University of Nevada, Reno

Photoionization and Photofragmentation of the Endohedral $Xe@C_{60}^{+}$ Molecular Ion

A dissertation submitted in partial fulfillment of the requirements for the degree of Doctor of Philosophy in Physics

by

Nagendra Bahadur Aryal

Dr. Ronald A. Phaneuf, Dissertation Advisor

May, 2013

University of Nevada, Reno
Statewide • Worldwide

THE GRADUATE SCHOOL

We recommend that the dissertation
prepared under our supervision by

NAGENDRA BAHADUR ARYAL

entitled

Photoionization and Photofragmentation of the Endohedral Xe@C60+ Molecular Ion

be accepted in partial fulfillment of the
requirements for the degree of

DOCTOR OF PHILOSOPHY

Ronald A. Phaneuf, Ph. D., Advisor

Peter Winkler, Ph. D., Committee Member

Jonathan Weinstein, Ph. D., Committee Member

W. Patrick Arnott, Ph. D., Committee Member

Sean M. Casey, Ph. D., Graduate School Representative

Marsha H. Read, Ph. D., Dean, Graduate School

May, 2013

Abstract

An experimental study of photoionization and fragmentation of the $Xe@C_{60}^{+}$ endohedral molecular ion is presented in the photon energy range of the well-known Xe 4d giant resonance, and evidence of redistribution of the Xe 4d oscillator strength in photon energy due to multipath interference is reported. Experiments were conducted at undulator beamline 10.0.1 of the Advanced Light Source (ALS) using the merged-beams technique. Prior to these measurements, macroscopic samples containing endohedral $Xe@C_{60}$ were prepared using a setup developed at the ALS. Endohedral $Xe@C_{60}$ yields as high as $2.5x10^{-4}$ were synthesized and a pure $Xe@C_{60}^{+}$ ion beam current of up to 5.5 pA was obtained for the merged-beams experiments. Cross sections were measured in the photon energy range 60 - 150 eV in 0.5 eV steps for single, double, and triple photoionization of endohedral $Xe@C_{60}^{+}$ accompanied by the loss of n pairs of carbon atoms yielding $Xe@C_{60-2n}^{2+}$ (n = 0, 1), $Xe@C_{60-2n}^{3+}$ (n = 0, 1, 2, 3), and $Xe@C_{58}^{4+}$ photo-ion products. Reference absolute cross-section measurements were made for empty C_{60}^{+} for the corresponding reaction channels. The spectroscopic measurements with $Xe@C_{60}^{+}$ were placed onto an absolute scale by normalization to the reference cross sections for C_{60}^{+} in ranges of photon energies where the Xe 4d contributions were negligible. Results for single photoionization and fragmentation of $Xe@C_{60}^{+}$ show no evidence of the presence of the caged Xe atom. The measurements of double and triple photoionization with fragmentation of $Xe@C_{60}^{+}$ exhibit prominent signatures of the Xe 4d resonance and together account for 6.6 ± 1.5 of the total Xe 4d oscillator strength of 10. Compared to that for a free Xe atom, the Xe oscillator strength in $Xe@C_{60}^{+}$ is redistributed in photon

energy due to multipath interference of outgoing Xe 4d photoelectron waves that may be transmitted or reflected by the spherical C_{60}^{+} molecular cage, yielding so-called confinement resonances. The experimental data are compared with numerous theoretical predictions for this novel single-molecule photoelectron interferometer system. The comparison indicates that the interference structure is sensitive to the geometry of the molecular cage.

Acknowledgements

I would like to express my sincere gratitude to a number of people, whose help and support made the completion of this dissertation possible. First and foremost, I would like to thank my academic advisor, Prof. Ronald A. Phaneuf, for your valuable practical guidance, scholarly inputs, advice, and encouragement over the course of this investigation. Without your support, the completion of this project could not have been possible. It has been a great opportunity to work under your supervision and to learn from your research expertise.

I would like to thank Dr. David A. Kilcoyne at the ALS. I really appreciate your valuable advice, help, and encouragement. I wish to thank Dr. Alejandro Aguilar at the ALS for your help and support. I would like to thank the collaborators: Dr. Alfred Müller, Dr. Stefan Schippers and Jonas Hellhund from University of Giessen, Germany. I would like to express my deep appreciation to the Division of Chemical Sciences, Geosciences and Biosciences of the U. S. Department of Energy for funding this project.

I would like to thank Dr. Peter Winkler, Dr. Jonathan Weinstein, Dr. W. Patrick Arnott, and Dr. Sean M. Casey for your helpful comments and for serving on my graduate committee.

My sincere gratitude goes to all the professors in the department of physics at University of Nevada, Reno. I thank Mercy Balderrama and Marvin Wakefield in the physics office, and our technical staff, Wade Cline in the physics machine shop for your support. I would like to thank my present and past student colleagues at UNR who participated in the collection of the data presented in the dissertation: Kiran Baral, Christopher Thomas, David Esteves and Ghassan Alna'Washi. In addition, I would like

to acknowledge all of my friends especially Netra Regmi for your help that drives me to give my best.

I would like to acknowledge all the teachers of Arjai Secondary School, Gulmi, Nepal, especially Gyan B. Karki, Sher K. C., Devi R. Aryal, and Champha B. Aryal for your guidance, blessing and support. I thank late Chandra K. Aryal, Khadga B. Aryal and Tulsi R. Aryal for inspiring me throughout my life.

Finally, I would like to thank my beloved wife Bindu, our children Raman and Rakshya for your love and unconditional support and patience along this journey. I owe a lot to my mom and dad who encouraged and helped me at every stage of my personal and academic life, and longed to see this achievement come true. Also thanks to my brothers Rajendra, Ramesh, Nabin and sister Usha for your continuous encouragement and support.

Nagendra B Aryal

May, 2013

Table of Contents

List of Tables

List of Figures

Abbreviations

ALS	Advanced Light Source
DFT	Density-functional theory
ECR	Electron-cyclotron-resonance
EUV	Extreme ultra-violet
EXAFS	Extended x-ray absorption fine-structure
GE	General Electric
HF	Hartree-Fock
IPB	Ion-photon-beam
KCN	Potassium cyanide
LBNL	Lawrence Berkeley National Laboratory
LTB	Linac-to-booster
MRI	Magnetic resonance imaging
NIST	National Institute of Standard and Technology
NMR	Nuclear magnetic resonance
OPV	Organic photovoltaic
RF	Radio-frequency
RPAE	Random phase approximation with exchange
TDDFT	Time-dependent density-functional theory
TDLDA	Time-dependent local density approximation
SR	Synchrotron radiation

Chapter 1
Introduction

This chapter presents some of the general motivations that have stimulated theoretical and experimental studies of photoionization of atoms, molecules and their ions, and present measurements for photoionization of the $Xe@C_{60}^{+}$ molecular ion. Experimental and theoretical efforts on photoionization of endohedral fullerenes are highlighted. The specific objectives of the present research are presented and finally, the content of the remaining chapters is outlined.

1.1 Motivations

Photoionization is a fundamental process of significant interest in atomic and molecular physics. The process provides a wealth of information about the electronic structure and dynamics of atoms, molecules, and their ions. Interactions of photons with ionic species dominate the plasma environments that constitute most of the observable universe as well as high-temperature research and engineering devices. In addition to the applications in space research, astrophysics, controlled thermonuclear research, and a number of areas of science and technology, photoionization cross sections for ions are essential data for the modeling of different types of plasmas [1]. Therefore, quantitative measurements of photoionization of atomic and molecular ions are important to benchmark the theoretical methods and models used in plasma studies.

The development of merged ion-photon beams and third-generation synchrotron radiation facilities provides a sufficiently high density of target ions and photon beams of

high brightness and narrow bandwidth to enable such measurements [2, 3]. The ion-photon-beam (IPB) endstation at the Advanced Light Source (ALS) facilitates quantitative experimental studies of photoionization and photofragmentation of singly and multiply charged atomic and molecular ions. When coupled with the high extreme ultra-violet (EUV) photon beam intensity, energy resolution and tuneability available at the ALS, photo-ion spectroscopy has been demonstrated to be a powerful probe of the structure and dynamics of atomic and molecular ions. Investigations of photo-ion spectra permit the identification of collective electron effects such as giant resonances and plasmon oscillations, and test sophisticated atomic structure and dynamics codes at unprecedented levels of precision.

Shortly after the discovery of the C_{60} fullerene molecule by Kroto and collaborators [4], so-called endohedral fullerene molecules were identified that contain an atom inside their spherical carbon cage [5]. Numerous studies have been aimed at characterizing the unusual physical properties of endohedral fullerenes and exploring multifold possibilities for their practical use in quantum computing [6], hydrogen storage [7] and medicine [8]. Evidence for the existence of C_{60} and C_{70} molecules containing noble gas atoms was discovered in samples from meteor, comet and asteroid impact craters by Becker et al. [9]. The isotopic ratios in these samples differ by an order of magnitude from those of noble gases found elsewhere on earth, indicating that the endohedral fullerenes are of extra-terrestrial origin and hence signifies their importance in astrophysical research.

The properties of an atom caged within an electrically charged spherical surface of nanometer scale present an intriguing fundamental quantum physics problem. Novel quantum effects associated with the photoionization of a noble gas atom located within a spherical shell of C_{60} were predicted [10] and subsequently termed confinement resonances [11]. Because noble-gas endohedral fullerenes were unavailable in sufficient quantity, theoretical activity on the subject of confinement resonances has been continued for more than a decade [11–18] in the absence of an experimental test. A Xe atom inside a fullerene molecule forms Van der Waals bonds, remaining neutral and centered within the cage [19]. Xe has a strong, broad 4d resonance signature in double photoionization near 100 eV [20]. The Xe atom inside a C_{60} molecule has been the subject of many theoretical studies as it best approximates an atom in a cage. Therefore $Xe@C_{60}$ was considered the most promising candidate for observation of quantum confinement resonances.

1.2 Preceding Experimental Efforts

Experimental data on photoionization of endohedral fullerenes are sparse because of the difficulty in producing sufficient amounts of purified endohedrals for the gas phase experiments [21]. Photoabsorption experiments involving endohedral fullerenes using the synchrotron radiation reported to date have been conducted however only for $Ce@C_{82}$ [22], $Dy@C_{82}$ [23], $Pr@C_{82}$ [24], $Sc_3N@C_{80}^+$ [25], and $Ce@C_{82}^+$ [21, 25].

Mitsuke and collaborators performed the time-of-flight measurements analyzing the charged products of photoabsorption in neutral metallofullerene vapors of $Ce@C_{82}$ [22], and $Pr@C_{82}$ [24] in the region of giant resonances. Evidences for the giant

resonance feature due to the 4d excitation of the encaged Ce and Pr atom were presented and found to be reduced by encapsulation. The data obtained have large absolute uncertainties due to difficulties in measuring and controlling the vapor density. In addition, the measured relative photo-ion yields have large statistical uncertainties resulting from the low target densities. The splitting of the 4d giant resonance in these measurements remained inconclusive because of the lack of sufficient statistical precision of the data.

The first photoionization experiments with endohedral fullerene ions were conducted at the ALS by Muller et al. [21] for $Ce@C_{82}^{+}$ and a clear signature of the Ce 4d resonance centered at 122 eV was observed. The valency of the caged Ce atom (+3) and a significant redistribution of the large Ce^{3+} 4d resonance oscillator strength within the endohedral molecule were confirmed. Although the statistical precision of the measurements was sufficient, no evidence of oscillatory structures was observed. This was attributed to the Ce^{3+} ion not being centered within the fullerene cage and ionic bonding with cage atom, resulting in hybridization of the atomic orbitals and a broadening of resonance features.

The first ever observation of the confinement resonances was reported by Kilcoyne et al. [26] in the total cross section for double photoionization of $Xe@C_{60}^{+}$ accompanied by loss of two carbon atoms. The experiment was conducted at the ALS by merging a mass-selected ion beam with a beam of monochromatized synchrotron radiation. Taken with a maximum ion beam current of only 0.3 pA, the measurements were suggestive of the predicted interference phenomenon but because of extremely low

product-ion count rates, their statistical precision was insufficient to adequately distinguish among the different theoretical predictions.

1.3 Preceding Theoretical Efforts

There have been a number of theoretical studies over the past decade on the photoionization of various atoms inside fullerenes [10, 13–18, 27–37]. Particularly, a number of theoretical calculations of the Xe 4d giant resonance in photoionization of $Xe@C_{60}$ using different approximations predict a redistribution of the Xe 4d oscillator strength as a function of photon energy compared to that for a free Xe atom (Figure 1.1). Puska and Nieminen [12] modeled for the first time the C_{60} molecule using a spherical shell with an attractive potential and used a jellium shell to calculate the 4d photoabsorption cross section of a Xe atom inside the C_{60} molecule. Their results demonstrated some oscillations in the dependence of the cross section on photon energy and noted that the cage-induced oscillations have the same nature as extended x-ray absorption fine-structure (EXAFS) measurements for solid-state systems. This feature of the photoionization spectrum of $Xe@C_{60}$ was termed 'confinement resonances' [11] which appear as a result of multi-path interference between the photoelectron waves from the caged atom and the electron waves reflected from the fullerene cage.

Amusia and co-workers [13] used a delta-like potential for the C_{60} shell of zero thickness and the random-phase approximation with exchange (RPAE) method to calculate cross sections for photoionization of $Xe@C_{60}$. Their results indicate that the Xe 4d giant resonance is distorted substantially, exhibiting four prominent peaks. The predictions for $Xe@C_{60}$ were subsequently reproduced by Dolmatov and Manson [14],

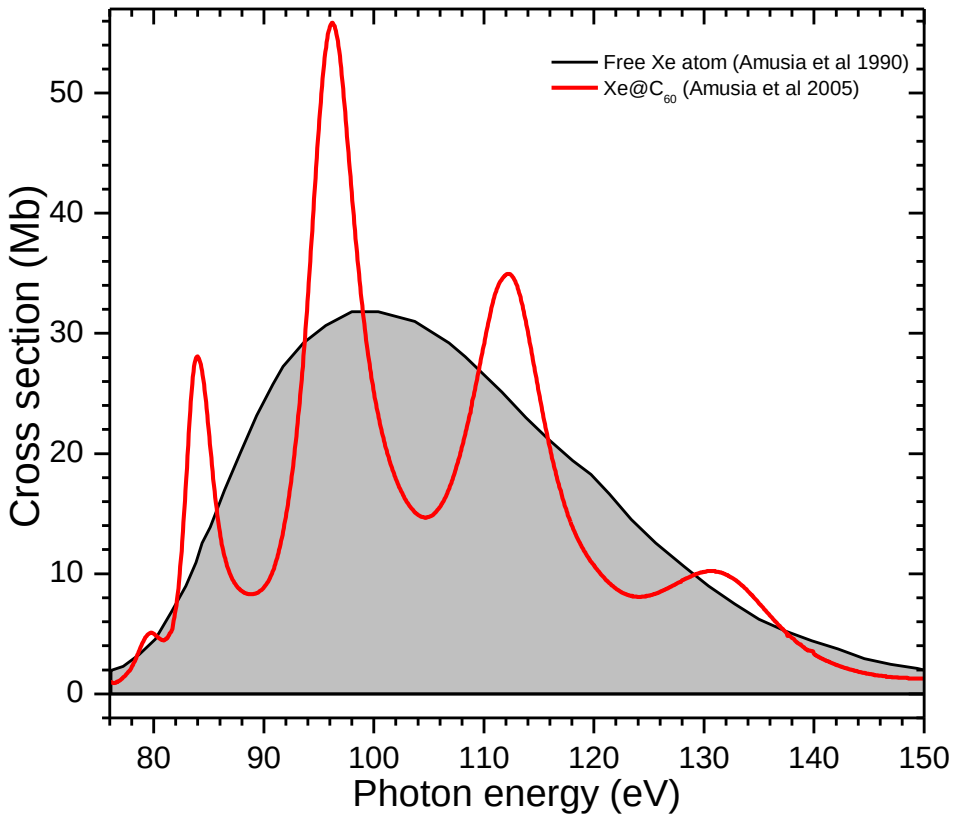

Figure 1.1 Theoretical calculations of cross sections for free Xe atom and endohedral Xe@C_{60} [13, 20].

who applied the RPAE methodology but argued that the amplitude of the oscillations depends on the thickness of the fullerene shell. They adopted a semiempirical value of 0.105 nm for the thickness of the C_{60} cage, resulting in damping of the predicted oscillations. Prominent oscillatory structures were predicted by Madjet et al. [15] who used the time-dependent density-functional theory (TDDFT) to study the 4d photoabsorption of a Xe atom inside a C_{60} molecule, which considers all the valence electrons to form a delocalized charged cloud and treats the residual ion-core as a classical jellium shell.

After the experimental results for photoionization of $Xe@C_{60}^{+}$ were reported for the first time by Kilcoyne et al. [26], a number of theoretical calculations have been reported. By using a technique based on Fourier-transforming cross sections to the reciprocal configuration space, time-dependent density-functional approximation (TDLDA) calculations for the single photoionization cross section of $Xe@C_{60}$ have been reported by Patel and Chakraborty [38]. A number of similarities between their prediction and the experimental data were claimed. Chen et al. [16] used the TDDFT method for the study of photoabsorption spectra of $Xe@C_{60}$ and compared their results with the experimental results for photoionization of $Xe@C_{60}^{+}$. Their calculations qualitatively confirmed the three main peaks observed in the experiment. Similarly, new numerical values for C_{60} cage potential were obtained by Dolmatov et al. [39] by fitting theoretical results to the experimental data for $Xe@C_{60}^{+}$, leading to a better agreement between experimental and theoretical data for $Xe@C_{60}$ spectra. Using these values for square-well potential parameters, Gorczyca et al. [18] applied R-matrix method to calculate cross sections for photoionization of $Xe@C_{60}$ in the vicinity of the Xe 4d giant resonance and compared with experimental results. Despite the discrepancy for peak cross section and width, agreement between the theory and experiment for the oscillatory structures was suggestive.

1.4 Objectives

The main goal of this dissertation was a definitive experimental study of photoionization and photofragmentation of $Xe@C_{60}^{+}$ molecular ions in the photon energy range of the well-known 4d giant resonance to explore the effect of the fullerene cage on

the caged Xe atom and to assess the validity of the theoretical predictions of confinement resonances associated with photoionization of $Xe@C_{60}$. The objectives needed to achieve this goal include: to prepare sample materials containing endohedral $Xe@C_{60}$ in order to produce $Xe@C_{60}^{+}$ ion beams sufficient for merged-beams experiments; to perform cross section measurements for photoionization and photofragmentation of $Xe@C_{60}^{+}$ yielding multiply-charged photo-ion products in the photon energy range 60 – 150 eV; and to provide a more definitive test of the theoretically predicted 'confinement resonances' associated with the photoabsorption of the Xe 4d in the photoionization of $Xe@C_{60}$ and a characterization of this phenomenon in terms of experimental variables. Such ambitious objectives were accomplished by developing an experimental set up at the ALS based on an ion beam implantation technique for sample production and optimization of production parameters; and performing cross section measurements for photoionization and fragmentation of $Xe@C_{60}^{+}$ at the IPB endstation of the ALS. Such experimental measurements were expected to be helpful in refining the computational techniques in an ongoing effort to improve theoretical models of interference phenomenon in such a complex multi-electron systems.

1.5 Organization of Dissertation

The organization of this dissertation is as follows. Chapter 2 presents a brief introduction to endohedral fullerenes with their potential applications, and the methods used for their production. Chapter 3 presents brief descriptions of the photoionization process, resonance phenomena and the theoretical methods. Chapter 4 describes the technique of merging counter-propagating beams of ions and monochromatized

synchrotron radiation to determine photoionization cross sections. The production and synthesis of sample materials containing endohedral $Xe@C_{60}$ at the ALS for merged-beams experiments are described in chapter 5. Cross section measurements for single and double photoionization with fragmentation of $Xe@C_{60}^{+}$ are presented in Chapter 6. In chapter 7, the triple photoionization with fragmentation of $Xe@C_{60}^{+}$ measurements are presented, and results for the Xe 4d contributions from all measured product channels are combined to compare with a number of theoretical results. A summary of this work, conclusions and an outlook for future related research are presented in chapter 8. Finally presented are the references used in this dissertation, and a list of publications of results of experiments in which the author of this dissertation has participated.

Chapter 2
Overview of Endohedral Fullerenes

2.1 Introduction

Fullerene, the third allotrope of carbon, was discovered by Kroto and collaborators in 1985 [4] during experiments aimed to understand the mechanisms behind the formation of long-chain carbon molecules in interstellar space. For this serendipitous discovery, a laser-vaporization supersonic cluster beam technique [40] was used. Their cluster beam studies showed that discrete mass peak corresponding to molecules with the exact mass of sixty carbon atoms, attributed to C_{60}, exhibit pronounced intensity in the spectrum under specific conditions along with other even numbered carbon mass peaks. They suggested that extra stability of C_{60} molecule is due to its spherical structure similar to that of a soccer ball. The C_{60} molecule consists of 60 carbon atoms bound in a nearly spherical configuration with a diameter of about 7.1 Å. This shape is called a truncated icosahedron, with 20 hexagons and 12 pentagons. In the truncated icosahedral structure of the C_{60} molecule all carbon atoms are equivalent, sharing a double bond and two single bonds with their nearest neighbors. The thirty double bonds, 1.40 Å in length, are located at the shared edges of adjacent hexagons and are shorter than the 1.45 Å single bonds surrounding each pentagon. Because of the resemblance of these molecules to the geodesic domes designed and built by famous architect R. Buckminster Fuller, the name "buckminsterfullerene" was given specifically to the C_{60} molecule. The word "fullerene" is now commonly used to represent the whole class of closed cage carbon molecules. This work was awarded the Nobel Prize for Chemistry in 1996. Later, pure samples of

these molecules were prepared and their structures characterized by their mass and ^{13}C NMR spectra, indicating the existence of a family of stable fullerenes, thus confirming a third form of carbon [41].

Because of their unique structures, the discovery of the fullerenes has attracted intense interests among scientists in a large variety of disciplines. However, nearly all fullerene research in the early stages was limited to theoretical studies due to lack of efficient productions of fullerenes. In 1990, Krätschmer and Huffman [42] at the Max Planck Institute for Nuclear Physics in Heidelberg, Germany used a carbon-arc plasma to produce the first macroscopic quantities of fullerenes. Since then fullerenes are among the most investigated molecules and are constantly attracting great attention within the scientific community.

One of the most fascinating and unique feature of fullerenes is the nanometer-scale nearly spherical empty space inside the carbon cage. The volume of the space depends on the size of the fullerene. Such a characteristic of fullerenes implies intuitively an idea of stuffing atoms into its empty space, resulting in the formation of endohedral fullerenes (Figure 2.1). As the novel form of fullerene-based materials, endohedral fullerenes represent a special class of nanostructures, which are characterized by a robust fullerene cage with atoms, ions, or small clusters trapped in its hollow volume. The possibility of producing endohedral fullerenes by inserting atoms into the cage had already been suggested by Kroto et al. [4]. Soon after, the first evidence for endohedral fullerenes, $La@C_{60}$ was reported in the mass spectra of clusters produced by laser vaporization of a La-impregnated graphite disk in a pulsed supersonic nozzle [5].

However, macroscopic quantities of the first endohedral fullerene La@C_{82} were produced in 1991 by Chai et al. [43] using the contact arc technique. Because the simple formula of MC_n cannot distinguish the fullerene with atom (M) inside the carbon cage composed of n carbon atoms from the other fullerenes with M outside the cages, a more explicit symbolism for the endohedral fullerene — M@C_n was constructed, where the symbol @ is used to state that atoms listed to the left of the @ symbol are situated inside the C_n cage. Since then, a large variety of endohedral fullerenes has been synthesized by encapsulating metal atoms or metal-containing clusters, noble gas atoms, group V elements or simple molecules inside the fullerenes.

2.2 Noble-Gas Endohedral Fullerenes

Noble-gas atoms inside a fullerene ideally do not interact or interact only weakly with the fullerene electrons. The first experiment in which noble gas atom was made to penetrate an intact fullerene cage was carried out by the Schwarz group in 1991 [44]. In this experiment, an energetic C_{60}^+ beam was made to collide with He atoms in the gas phase. Evidence for formation of an endohedral compound rather than the He being weakly bound to the outside of the cage was obtained by the same group in a series of neutralization/re-ionization experiments [45]. Many research groups have investigated the noble-gas endohedral compounds using different methods, such as collision methods, high pressure and high temperature methods, nuclear recoil implosion methods and beam implantation methods. These methods are described separately in the next section.

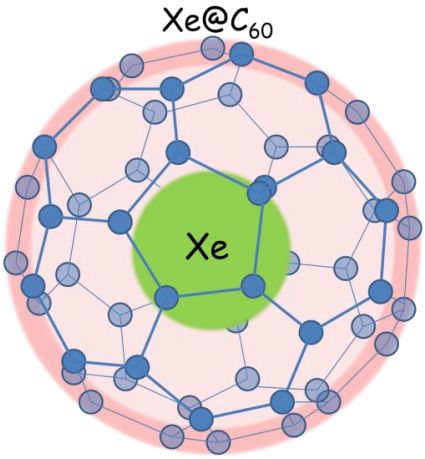

Figure 2.1 A schematic diagram of Xe atom inside C_{60}.

2.3 Methods for Noble-Gas Endohedral Production

2.3.1 Collision Methods

The noble-gas endohedral fullerenes have been synthesized in minute amounts in gas phase experiments carried out under single-collision conditions. For the first time, evidence for the formation of $He@C_{n-2x}^{+}$ ions (x= 1, 2, 3, ….) was observed by the Schwarz group using a four-sector mass spectrometer in which energetic fullerene ions with kinetic energies of several thousand electron volts collided with helium atoms [44]. Ross and Callahan reproduced the experimental results and reported the identification of the $He@C_{60}^{+}$ product, indicating that the helium adduct formation does not require fragmentation [46]. Caldwell et al. showed that, besides He, Ne and Ar may also be captured by C_{60}^{+} at similar collision energies [47]. Further strong evidence for endohedral formation was provided by Campbell et al. who demonstrated that the He capture by C_{60}^{+} is associated with sizeable energy barrier [48]. Collisions of Ne^{+} with C_{60} at high energies in tandem mass spectrometers were shown to form capture complexes by Christian et al.

[49]. All these experiments produced minute amounts of the endohedral species which were observed only in mass spectrometers and could not be isolated in sufficient quantity to subject them for further experiments.

2.3.2 High Pressure and High Temperature Method

Saunders and collaborators developed a high pressure and high temperature method for preparing endohedral complexes of C_{60} and C_{70} with the noble gases, He, Ne, Ar, Kr, and Xe and they verified the syntheses by mass spectroscopy [50, 51]. They proposed the "window" mechanism involving reversibly breaking one or more bonds to temporarily open a window in the cage which is large enough for entry of atoms. Fullerenes were heated at 600^0C under high pressure of a noble gas up to 2700 atm and synthesized the noble gas (He, Ne, Ar and Kr) endohedral with 0.1- 0.3% yield in the products. The Xe@C_{60} concentration in the product prepared by this method was only 0.008%, but the yield reached 0.3% with the use of cyanide (KCN) as a catalyst [52].

2.3.3 Nuclear Recoil Implosion Method

In this method, radioactive atoms are implanted into the fullerenes by recoil implantation processes following nuclear reactions. Braun and Rausch [53] in 1995 showed evidence for radionuclide endohedral formation from neutron irradiation of polycrystalline C_{60}, as a result of an Ar impurity trapped in the solid. They proposed that endohedral radionuclide formation was the result of penetration of radioactive ^{41}Ar atoms into the C_{60} cages by taking into account of the high nuclear recoil energy produced from prompt gamma emission following the nuclear reaction, $^{40}Ar(n,\gamma)^{41}Ar$. By using the same method, Gadd et al. [54] observed noble-gas radionuclide endohedrals, RN@C_{60} (RN =

^{125g}Xe, ^{133g}Xe, ^{135g}Xe, ^{41}Ar, and ^{85m}Kr) from interstitial fullerenes. Ohtsuki et al [55] expanded this method and produced radioactive endohedral fullerenes $^{127}Xe@C_{60}$ and $^{79}Kr@C_{60}$ by mixing the fullerene material with potassium-iodide ($K^{127}I$) or potassium-bromide ($K^{79}Br$), respectively, and irradiating the mixed material with deuterons. Based on their *ab initio* molecular dynamics simulations, it was confirmed that the insertion of the Xe atom into C_{60} through six-membered rings is possible in the range 130-200 eV of kinetic energy.

2.3.4 Ion Implantation Method

Shimshi et al. [56] developed an experimental set up for endohedral production using an ion implantation method. The fullerenes emerging from an oven heated to 470^0C were continually deposited on a rotating aluminum cylinder and were exposed to the ions accelerated up to 230 eV to synthesize $He@C_{60}$ and $Ne@C_{60}$. Wantanbe et al [57] also applied an ion implantation method to the production of $^{133}Xe@C_{60}$. Fullerene targets were made by vacuum evaporation of fullerenes on Ni foils, and by using an isotope separator, ^{133}Xe ions were implanted into the targets. For implantation of these radioactive atoms, their ions were accelerated to 40 keV to be mass-separated from stable isotopes.

2.4 Applications

Endohedral fullerene molecules have opened many possibilities for research and have been attracting wide interest, not only in physics and chemistry but also in such interdisciplinary areas as materials and biological sciences. Their physical and chemical

properties are very important for their potential applications in the biomedical field, information technology, and energy sources.

Biomedical applications of endohedral fullerenes have been reviewed extensively [58]. Some of them are as encapsulating hosts for the chemical isolation of highly reactive or toxic atoms in medical diagnostics [59], and as delivery media for pharmaceuticals [60]. Endohedral fullerenes can shield radiotoxic materials from the environment and with their high kinetic stability they can be used as a radiotracer in nuclear medicine. It is known that endohedral fullerenes ($Gd@C_{82}$) could be used as contrast agents in magnetic resonance imaging (MRI) for diagnostic purposes. Also, endohedral $^{133}Xe@C_{60}$ has been proposed as a radiopharmaceutical for cancer therapy [57].

Recently, concepts for quantum computation using endohedral fullerenes as spin–qubits have been presented [6]. Qubits or quantum bits are the fundamental unit of information in quantum computers and endohedral fullerenes in particular $N@C_{60}$ and $P@C_{60}$ are considered to be possible candidates for qubits, since these encapsulated elements retain their atomic nature.

Hydrogen is a clean, sustainable and renewable energy carrier, and a hydrogen energy system is expected to progressively replace the existing fossil fuels in the future. It has been predicted that endohedral fullerenes can be promising candidates for hydrogen storage [7] , which can accelerate the development of hydrogen fuel cell-driven vehicles. The organic photovoltaic cell (OPV) has potential use as a solar energy conversion device that has not only lower production costs but also represents a promising

alternative for low-cost renewable energy sources. However, the low voltage output is one of its fundamental limitations. Recent theoretical and experimental data suggest that trimetallic nitride endohedral fullerenes as acceptor materials for use in photovoltaic devices offer high power conversion efficiencies [61].

Chapter 3
Theoretical Background

Photoionization is a fundamental phenomenon which has attracted considerable interest as it provides a means to reveal the electronic structure and dynamics of atoms, molecules and their ions. The theoretical description of photoionization is based on quantum mechanics. In principle, understanding of the photo-interaction requires the correct and exact solution of the Schrodinger equation which is only possible in a few cases like hydrogen and hydrogen-like ions. In many-electron systems, electron-electron interactions make it impossible to obtain the exact solution. Therefore, different approximation methods are developed to explain the photo-interaction results. In this chapter, some of these theoretical methods commonly used to calculate photoionization cross section and that are relevant to our measurements are introduced. The mechanisms of photoionization and their contributions to the ionization cross section, as well as some fundamental equations for the cross section and oscillator strength are given. Finally, the last sections in this chapter are concerned with giant resonances and confinement resonances.

3.1 Introduction

The quantitative description of the energy levels of the electrons is given by the solution of Schrödinger's equation for non-relativistic system with N electrons,

$$H\,\Psi_k = E_k\,\Psi_k \tag{3.1}$$

where k is the set of good quantum numbers, Ψ_k and E_k are the eigenfunctions and eigenvalues of the system and H is the Hamiltonian operator. The Hamiltonian operator

includes separate kinetic and potential energy terms, such that for an *N*-electron atom of atomic number *Z*, the Hamiltonian in the non-relativistic picture is given by:

$$H = \sum_{i=1}^{N} \frac{p_i^2}{2m_e} - \sum_{i=1}^{N} \frac{Ze^2}{r_i} + \sum_{i \neq j} \frac{e^2}{|r_i - r_j|} \tag{3.2}$$

where p is the momentum of the electron, e is the electron charge, m_e is the electron mass and $r_{i,j}$ are the coordinates of the electron. The first term of the Hamiltonian represents the kinetic energy of the i^{th} electron. The second term defines a potential energy arising from the attraction of each electron to the nuclear charge Ze, i.e. the Coulomb interaction between the nucleus and i^{th} electron, and the last term represents electron-electron Coulomb interactions. Analytical solutions of this equation are only possible for hydrogenic systems, i.e. for one-electron systems. For multi-electron systems, the electron-electron interactions, represented by the last term of this equation, make analytical solutions of Schrödinger's equation impossible. Therefore more sophisticated approximation methods are needed to include such so-called electron-correlation effects and to calculate the various aspects of the complex spectra obtained in photoionization studies of atoms and ions. To address this issue, different approximation methods have been developed and are briefly introduced in the following section.

3.2 Theoretical Methods

As mentioned earlier, the presence of the electron-electron interaction term for a many-electron system makes the Schrödinger equation insoluble in general and poses a major challenge in all areas of atomic and molecular physics. Therefore, approximation methods are required to obtain a wavefunction for the many-electron system. A number

of methods have been developed that differ mainly in the way in which the electron-electron interaction is included. Among them, only the Hartree-Fock method, the random phase approximation with exchange (RPAE), the time-dependent density-functional approximation (TDDFT), and the R-matrix method relate to the present work and are described here. Details of these methods can be found in [62-64].

3.2.1 Hartree-Fock Method

Hartree-Fock (HF) or self-consistent field method [62] is the independent-particle model according to which each electron in the atom moves independently in the Coulomb field of the nucleus and the average field due to the other electrons. Then each electron in the system is described by its own separate wavefunction. To approximate an exact solution of the *N*-electron problem within this framework, the total wavefunction of the system is described by an antisymmetric product of individual orthonormalized single-particle spin-orbitals or the Slater determinant,

$$\Psi = \frac{1}{\sqrt{N!}} \det\left[\Psi_i(x_j)\right] \tag{3.3}$$

where the coordinates of the space and spin are included in the variable $\boldsymbol{x_j}$. The Slater determinant is then obtained using the variational method by requiring that the energy expectation value, $\langle H \rangle$, to remain stationary under small variations, $\Psi + \delta\Psi$, such that the change in Ψ to be zero:

$$\frac{\delta}{\delta\Psi_i}\left[\langle H\rangle \; - \sum_j \varepsilon_j \int \left|\Psi_j\right|^2 d^3r \right] = 0 \tag{3.4}$$

where ε_j is a Lagrange multiplier resulting from the orthogonality requirement, representing the binding energy of the *i*th electron. This procedure leads to a set of one-electron equations, called the Hartree-Fock equations.

$$\left(-\frac{\hbar^2}{2m_e}\nabla_i^2 - \frac{Ze^2}{r_i} + e^2\sum_j \int d^3r' \frac{|\Psi_j(r')|^2}{|r_i - r_j|}\right)\Psi_i(r)$$

$$- e^2\sum_j \delta_{\sigma_i\sigma_j}\int d^3r' \frac{\Psi_j^*(r')\Psi_i(r')}{|r_i - r_j|}\Psi_j(r) = \varepsilon_i\Psi_i(r) \qquad (3.5)$$

where $\boldsymbol{r}$ and $\boldsymbol{r'}$ are the position vectors of the electrons, and σ_i labels the spin of particle *i*. The first and second terms in the left hand side of this equation represent the electron kinetic energy and the electron-nucleus Coulomb interaction, respectively. The third term, which is known as the Hartree term, represents the electron-electron Coulomb potential. The unphysical self-interaction of electrons when $i = j$ in this term is cancelled by the fourth term, which is known as the exchange term resulting from the inclusion of the Pauli exclusion principle and the assumed determinant form of the wavefunction. It takes into account the exchange effects between the states $\Psi_i\ (r_i)$ and the $N - 1$ other states occupied by the electrons. It is only non-zero when considering electrons of the same spin. The exchange term makes the Hartree-Fock equations difficult to solve in most cases. The central field approximation allows a separation of the orbital component of the wavefunction into radial and angular parts. The one-electron equations are then solved by a self-consistent method.

When applied to the photoionization process, this method has one basic limitation that it assumes all atomic electrons move independently in a static field which is the same before and after the photoionization event. Thus although the HF approximation is used

to calculate the initial wavefunctions, the theoretical methods used in the calculation of ionization processes seek to provide a realistic description of the effect of a time-dependent field interacting with the electrons of the atom or ion.

3.2.2 Random Phase Approximation with Exchange (RPAE) Method

RPAE is a prominent theoretical method which accounts for the effect of the time varying electromagnetic field by considering the polarization of the electron cloud due to the absorption of photon. This method was initially developed in the field of condensed matter physics to analyze the behavior of an electron gas [65]. The term "random phase" was used to describe certain matrix elements which were neglected because of cancellation due to their random phases in the limit of a very large number of electrons. The first attempt to apply RPAE was made by Altick and Glassgold [66] for atomic photoionization. However, good agreement with experiment was achieved only after substantial improvements were made by Amusia and co-workers [67] to account for inter-channel interactions.

The electron and hole wavefunctions are calculated using the HF approximation, and the RPAE corrections are applied to the dipole operator, which is modified to account for the inter-electron Coulomb interaction; electron correlations are separated into the two classes: inter- and intra-shell. This method does not take into account the higher order effects, such as the interaction between two electron–hole states, but such interactions are not usually important above second order. The RPAE accounts for both static and dynamic rearrangement of the atomic electrons. Static rearrangement is the compression of the orbitals of outer shell electrons due to the vacancy created by the photo-ejected electron or as a result of Auger decay where the outgoing photoelectron

moves in the strong attractive field caused by at least two vacancies. By taking into account the response of the atomic system to the polarizing effect of the incident photon, dynamic rearrangement is included, but a separate dynamic effect, polarization of the atomic core through its interaction with the outgoing electron, is not included. Hence the technique includes both direct removal of an electron by the absorption a photon and indirect removal or excitation of another electron via correlation. Furthermore, by including an infinite class of diagrams, the RPAE avoids the sum rule problems that plague HF calculations. The principal drawback of this approach is its computational complexity, which renders similar calculations for larger systems intractable.

3.2.3 Time-Dependent Density-Functional Theory (TDDFT)

Density functional theory (DFT) was developed by Hohenberg and Kohn [68] and its practical formulation was provided by the Kohn and Sham [69] as a ground state theory which is not strictly applicable to the calculation of excitation energies or other excited-state properties. The extension of DFT to deal with the time-dependent Schrödinger equation and excited-state properties has been achieved with the formulation of time-dependent density-functional Theory (TDDFT), a theory mathematically established by the theorem of Runge and Gross [70]. Individual excitation energies can be computed using TDDFT together with linear response theory which is a straightforward consequence of the time-dependent Schrödinger equation in a perturbative treatment. The idea of calculating excitation energies within the linear response regime of time-dependent density-functional theory is based on the fact that the frequency-dependent linear density response of an interacting system has poles at the exact excitation energies of the system.

Different practical implementations of the TDDFT concerning the calculation of optical absorption spectra in the linear regime using the dipole approximation are available in its most general form by expressing the TDDFT linear response problem in terms of a Dyson-like equation [71], Casida's equations. The Dyson-like equation allows computation of a generalized susceptibility whose poles are excitation energies, and the polarizibility which gives the optical absorption spectra of the system under investigation. The Dyson-like equation for susceptibility has been reformulated by Casida [72] into an eigenvalue problem, whose eigenvalues and eigenvectors are used to build the optical absorption spectra. The construction of Casida's equations requires the prior diagonalization of the full ground-state problem. The eigenvalue problem is then efficiently solved by iterative techniques.

3.2.4 R-Matrix Method

This method was first developed to describe resonances in nuclear reactions by Wigner and Eisenbud [73] and was adapted originally by Burke and co-workers [74] for the calculation of photoionization cross sections. This method was the basis of the calculations done in the OPACITY and IRON projects [75] to produce an atomic database for astrophysical applications, and is used for calculations of cross sections and spectral structure of free and confined atoms [18].

The R-matrix method separates the calculation into two regions, an inner one in which electron correlation is expected to be strong, and an outer one in which the electron correlation can be neglected. The choice of radius of the inner region is important because it varies with the atom or ion being studied. The problem is solved by ensuring continuity of the outer and inner wavefunctions and their first derivatives across the

boundary region. In the internal region the problem cannot be solved exactly due to strong electron correlation, but in the outer region the solution to the problem is simple due to weak electron-electron interactions.

3.3 Photoionization Cross Section and Oscillator Strength

The binding energy of an electron in an atom or molecule is the minimum energy required to free that electron from the Coulomb potential well due to the nucleus and neighboring electrons, i.e. to ionize it. The ionization potential of an atom, molecule, or ion is the binding energy of an electron in the ground or lowest occupied energy level. Photoionization can result from absorption of a photon by an atomic or molecular system, if the photon energy exceeds the ionization potential. Two processes could be involved in this interaction are: direct or non-resonant photoionization and indirect or resonant photoionization. These two mechanisms contribute differently to the photoionization cross section. Here, the single photoionization process will be considered in which the interaction between a photon and an ion removes one electron from the ion.

Direct or non-resonant photoionization is the consequence of the absorption of a photon whose energy matches or exceeds the binding energy of the electron being ejected from the atom or the ion. For positive ions, this process is manifested as a step-function rise of the photoionization cross section at the threshold or minimum photon energy, falling off monotonically with increasing photon energy. Direct photoionization may be represented by the following pathway:

$$h\nu + A^{q+} \rightarrow A^{(q+1)+} + e^{-} \tag{3.6}$$

where h is Planck's constant and ν is the photon frequency.

Indirect or resonant photoionization may result from excitation of a core electron to a discrete unoccupied state whose energy is greater than the ionization potential. In this case, the photon energy must match the energy difference between the initial and final states, so it is a resonant process. There is a high probability that such a multiply-excited system will minimize the excess energy by a so-called Auger or autoionization process in which one or more electrons may be ejected. This process is manifested in the cross section as a resonance and may be represented as follows:

$$h\nu + A^{q+} \rightarrow (A^{q+})^{**} \rightarrow A^{(q+1)+} + e^{-} \tag{3.7}$$

The photoionization cross section σ in megabarns (1Mb = 10^{-18}cm^2) is given in the dipole approximation by [113]:

$$\sigma(E) = 2\pi^2 \alpha a_0{}^2 R \frac{df}{dE} = 1.097618\, x\, 10^{-16} eVcm^2 \frac{df}{dE} \tag{3.8}$$

where α is the fine structure constant, a_o is the Bohr radius, R is the Rydberg constant, and df/dE is the differential oscillator strength per unit energy. Then, an electric dipole transition between the initial and final states can be characterized using the dimensionless oscillator strength,

$$f_{ij} = \frac{1}{3g_i R}(\Delta E)S \tag{3.9}$$

where g_i is the statistical weight ($2J_i+1$) of the initial state i, J_i is the total angular momentum, f_{ij} is the dimensionless (absorption) oscillator strength, and ΔE is the transition energy ($E_f - E_i$). S is the electric dipole line strength, which is the square of the reduced matrix element of the electric dipole operator D of the atomic system,

$$D = -e\sum_{k=1}^{N} r_k \tag{3.10}$$

between the initial bound state Ψ_i and the final continuum state Ψ_f,

$$D_{if} = \langle \Psi_f | D | \Psi_i \rangle$$

In the *LS*-coupling scheme, the non-zero matrix elements are characterized by the angular momentum selection rules for electric-dipole transitions,

$$\Delta S = 0,$$

$$\Delta L = 0 \text{ or } \pm 1, \text{ and } L_i + L_f > 0,$$

$$\Delta J = 0 \text{ or } \pm 1, \text{ and } J_i + J_f > 0,$$

$$\Delta \pi = \pm 1.$$

where *L*, *S*, and *J* are the orbital, spin, and angular quantum numbers, and π represents the parity operator. The last rule is a consequence of the odd parity of the electric dipole operator.

Integrating the cross section σ (Mb) in equation (3.8) between two energies E_1 and E_2 (eV) yields a practical expression for the average oscillator strength:

$$f_{12} = 9.1106\, x\, 10^{-3} \int_{E_1}^{E_2} \sigma(E) dE \tag{3.11}$$

where the energy *E* is in eV and the cross section σ is in Mb. This formula was used to calculate the total photoionization oscillator strengths for the xenon atom reported in this dissertation. According to the Thomas-Reiche-Kuhn sum-rule, the total oscillator strength of the transitions originating from the 4d subshell of a xenon atom is equal to the number of electrons populating it, i.e. ten.

3.4 Giant Resonance

The study of giant resonances is of great interest, because of their collective nature. It is interesting that they persist over ranges of sizes, from nuclei, through atoms and molecules and even to clusters of large size. The energy of giant resonance peaks varies from ~ 2 eV in alkali-metal clusters to ~ 20 MeV in nuclei (a range of 7 orders of magnitude) [76].

The term "giant resonance" originates from nuclear physics and was observed for the first time by Baldwin and Klaiber in 1947 in measurements of x-ray photon-induced fission [77-79]. The word 'giant' refers merely to the fact that the resonance dominates the observed cross section within a broad energy range and exhausts the oscillator strength available under the dipole sum rules for a complete shell of particles. They were attributed to the collective motion of a shell of nucleons. In atomic physics, the origin of giant resonances is the collective excitation of an entire electron subshell. These autoionizing excitations are characterized by a strong oscillator strength that depends on the occupancy of the subshell being excited. Excitation of a filled 4d subshell, for example, exhibits a broad asymmetric 4d - ϵf resonance for neutral atoms and low-charge-state ions, as observed in photoionization of Xe [80]. In molecular physics, giant resonances have been observed in the photoionization of fullerenes, hollow closed-shell molecules composed solely of carbon atoms. Two distinct resonances attributed to electric-dipole-excited collective electron oscillation modes were observed in these molecules. A strong surface plasmon resonance occurs at photon energy near 22 eV for the C_{60}^{+} molecular ion. A second resonance attributed to a volume plasmon excitation occurs near 38 eV [81].

3.5 Confinement Resonances

In the photoionization spectra of atoms endohedrally confined within a fullerene cage, resonances arise due to the presence and properties of the confining cage, and which do not exist in the spectrum of the free atom, have been termed ‘confinement resonances’. The phenomenon results from multi-path interference of photoelectron waves emitted by the encaged atom that may be transmitted or reflected by the carbon cage. It may be considered as a single-molecule analog of EXAFS (extended x-ray absorption fine structure) [82] that is widely used for structural analysis in surface science. Confinement resonances were first reported by Puska and Nieminen for the phoionization of caged Xe and Ba atoms in C_{60} cage [10]. After that, a large number of theoretical calculations of the Xe 4d giant dipole resonance in photoionization of $Xe@C_{60}$ using different approximations predicted a significant redistribution of the Xe 4d oscillator strength as a function of photon energy relative to that for a free Xe atom. These calculations indicate that the interference structure is sensitive to the thickness and confinement potential of the carbon cage and the position of the atom within.

Chapter 4
Experimental Technique

4.1 Introduction

The photoionization cross section measurements reported in this dissertation were performed at the ion-photon-beam (IPB) endstation on beamline 10.0.1 at the Advanced Light Source (ALS), a third generation synchrotron radiation source located at Lawrence Berkeley National Laboratory in Berkeley, California. Based on the principle of merged-beams technique [83], the apparatus was designed and constructed at the University of Nevada, Reno and permanently installed as a multi-user facility at ALS in 1999. It has since been used for the experimental studies of the interaction between multiply charged atomic or molecular ion beams and a photon beam by overlapping them along a common path. The details of the IPB endstation have been described in the Ph. D. dissertations of Alex Aguilar [114] and David Esteves [115] and reported by Covington et al. [84]. Therefore, only a brief description of the principal components of the merged-beams experiment and the procedures involved in the measurements are presented in this chapter.

4.2 Synchrotron Radiation

Synchrotron radiation (SR) is a very bright, broadband, polarized source of electromagnetic radiation that covers the entire electromagnetic spectrum from the infrared region through the visible, ultraviolet, and into the X-ray region. It is well known from the classical theory of electricity and magnetism that accelerating charges passing

through a transverse magnetic field emit electromagnetic radiation in a direction perpendicular to both the directions of acceleration and magnetic field. In the case of synchrotron radiation, relativistic electrons are accelerated in a circular orbit and emit electromagnetic radiation that takes the form of a narrow cone tangent to the trajectory of the accelerated electrons [85, 86].

Natural synchrotron radiation from charged particles spiraling around magnetic field lines in space is as old as the stars, for example, the light we see from Crab Nebula [87]. Although the first theoretical predictions were made by Lienard 1898, the most complete theory of synchrotron radiation was established by Schwinger [88] in a convenient form for practical computation after its first experimental observation by a team of scientists working at the General Electric (GE) Laboratory in 1946 [89, 90]. Only after 20 years was synchrotron radiation used for ultraviolet/soft-x-ray absorption spectroscopy by Tomboulian and Hartman [91], and recognized as a powerful research tool.

In synchrotron radiation sources, radiation is caused by transverse acceleration due to magnetic forces in bending magnets (forming the circular path) or periodic acceleration in special insertion devices called wigglers and undulators [86] (see Figure 4.1). Figure 4.2 compares the radiation from a bending magnet and an undulator.

4.2.1 Bending Magnet Radiation

When relativistic electrons travel in a uniform magnetic field of a bending magnet, they are subjected to a Lorentz force that accelerates the electron centripetally and bends the electrons into a circular orbit. The bending results in the emission of synchrotron radiation having comparatively low brightness, directed tangentially outward

in a narrow radiation cone. The radiation spectrum is very broad and the emission angle is typically $1/\gamma$, where γ is the Lorentz contraction factor ($\sqrt{1-\gamma^2/c^2}$).

4.2.2 Wiggler / Undulator Radiation

Wigglers and undulators are the two principle types of insertion devices added to the synchrotron radiation sources in straight section between bending magnets to extend the spectral range and increase the brightness. They produce oscillatory motion of the electron beam resulting in the emission of radiation with special properties. Wigglers create a broad but intense beam of incoherent light. Undulators create a narrower and significantly more intense beam of coherent light, with selected wavelengths which can

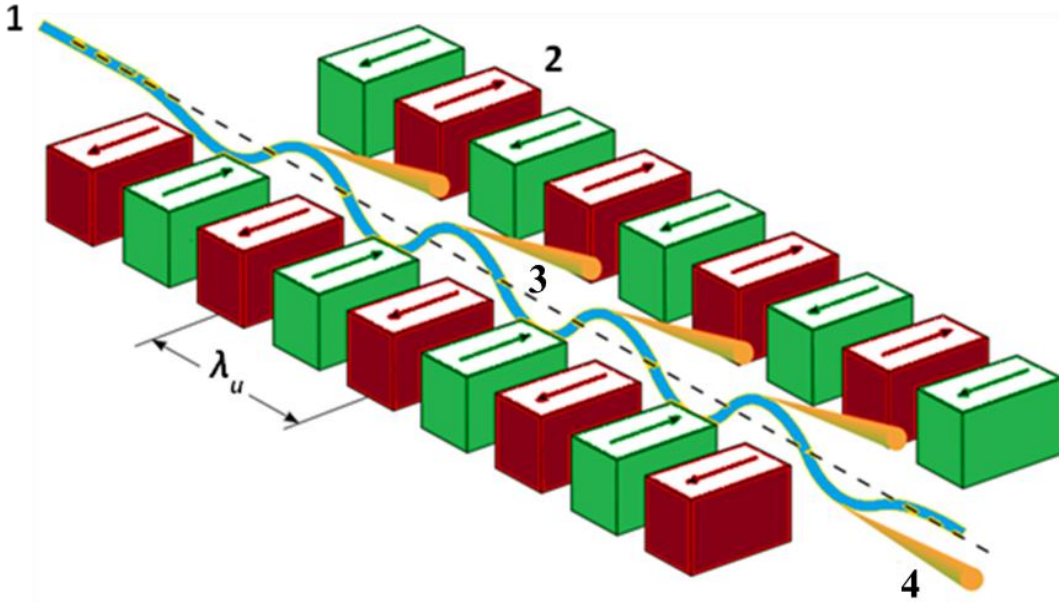

Figure 4.1 Conceptual diagram of an undulator/ wiggler. Alternating magnetic field induced by opposing dipole magnets (2) force the electrons (1) to accelerate relativistically as they pass through the gap (3), resulting coherent synchrotron radiation (4) [116].

be tuned by manipulating the magnetic field in the device. Insertion device can be characterized by the deflection parameter, K_{id}, related to the peak magnetic field B_0 in Tesla by

$$K_{id} = \frac{\text{max. orbit deflection angle}}{\text{radiation spread angle}} = \frac{1}{2\pi}\frac{eB_0\lambda_{id}}{mc} \approx 0.934\,\lambda_{id} \qquad (4.1)$$

where λ_{id} is the magnetic period of the insertion device in cm. Wigglers and undulators differ fundamentally in their values of K_{id}, which controls the properties of the radiation emitted. Since the deflection parameter K_{id} is related to the maximum deflection angle of the oscillating electrons, the resulting synchrotron emissions are contained within a central radiation cone of half-angle θ such that

$$\theta = \frac{1}{\gamma\sqrt{N}} \qquad (4.2)$$

where N is the number of magnetic periods within the insertion device. When $K_{id} \gg 1$, the electron oscillations extend beyond the central radiation cone thus minimizing interference caused by the magnets. This is the physical characteristic of a wiggler. When$K_{id} \leq 1$, then the electron oscillations are entirely within the central radiation cone thus increasing the interference effects of the magnets and degree of coherence. This is the physical characteristic of an undulator. The radiation from an undulator has a narrower spectrum. The wavelengths of the lines can be derived by first Lorentz transforming the undulator field to the rest-frame of the beam. The radiation by the beam in its own rest-frame induced by the undulator field is then Doppler shifted back into the laboratory-frame. This gives:

$$\lambda_n = \frac{\lambda_u}{2n\gamma^2}\left(1 + \frac{K^2}{2} + \gamma^2\theta^2\right) \tag{4.3}$$

where n is the harmonic order and θ is the deviation angle of the direction of observation from the forward direction. Equation 4.3 indicates that the wavelength of the undulator radiation can be tuned through the deflection parameter of undulator, K, by varying the magnet gap and hence the peak of magnetic field B_0 (Figure 4.1).

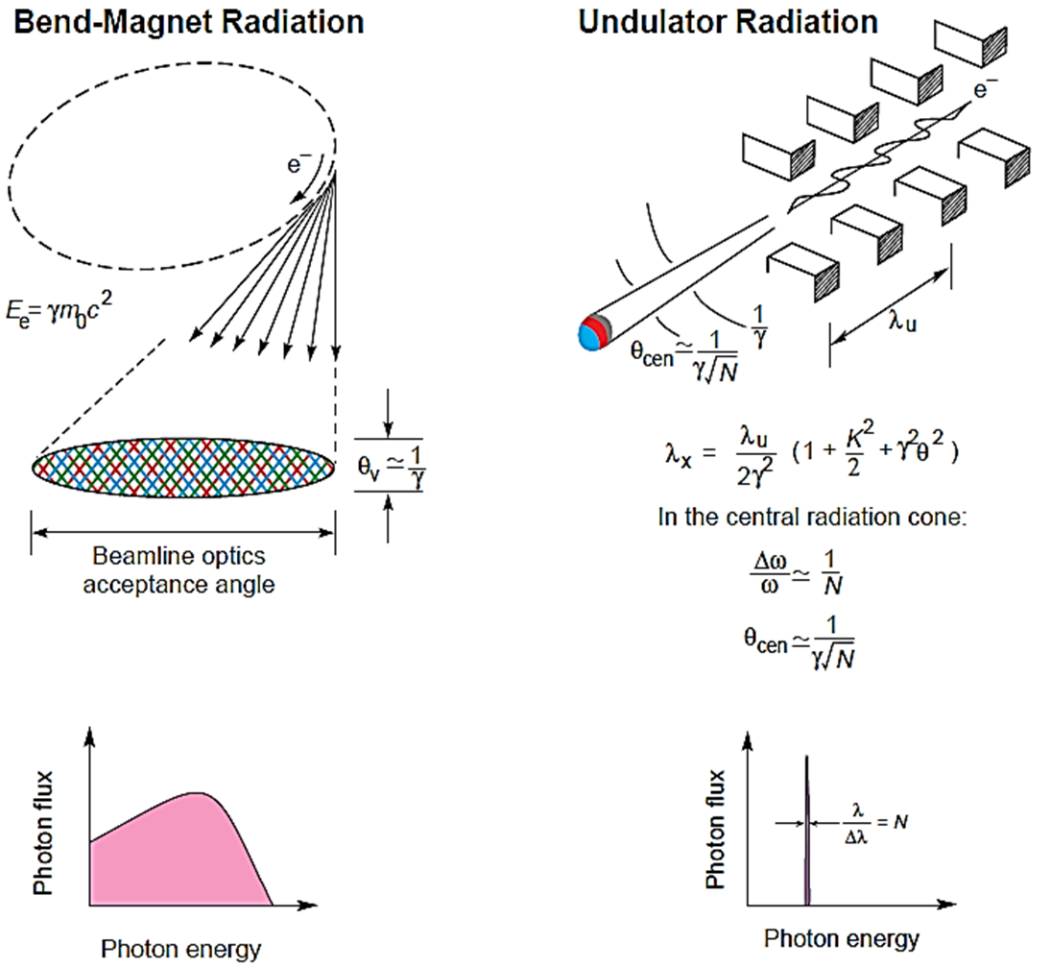

Figure 4.2 Comparison of the radiation from a bending magnet and an undulator [117].

Facilities dedicated to the production and use of synchrotron radiation are known as synchrotron light sources and their evolution is usually described in terms of three generations [92]. Until about 1975, synchrotron radiation was produced as a by-product of accelerators that were designed and built for high energy physics experiments. Their SR was intense but change in intensity, source position within a cycle and cycle-to-cycle fluctuations pose limitations. With the development of high energy physics storage rings, SR became available with constant spectrum and source position, and long stored-beam lifetime. The pioneering uses of the first generation synchrotron radiation facilities in many different research fields were made in a parasitic mode [85]. In the mid-1970's, totally dedicated SR facilities were designed and constructed for use of synchrotron emissions for scientific purposes. These early dedicated facilities, in which synchrotron light is mostly produced at bending magnets, are called second generation sources. Later, an important method of enhancing brightness of synchrotron light was made with the use of insertion devices such as wigglers and undulators on these facilities, though they are not well optimized. Third generation light sources are the dedicated synchrotron radiation storage rings designed specifically to take advantage of insertion devices, primarily undulators. These facilities provide synchrotron light with special features of high brightness, lower beam emittance and long beam life by incorporating long straight sections into the storage ring for insertion devices.

4.3 The Advanced Light Source

The Advanced Light Source, located at Lawrence Berkeley National Laboratory in Berkeley, California, is a third-generation synchrotron radiation source dedicated to produce vacuum ultraviolet light with very high brightness. Figure 4.3 shows a schematic

layout of the ALS storage ring of 200-m circumference which is in fact a series of straight sections connected at bend magnet locations and insertion devices located exclusively along the straight sections between bend magnets.

Electrons bunches produced by a thermoionic gun are accelerated by a 4-meter-long linear accelerator into a linac-to-booster (LTB) transfer line at an energy of 50 MeV. The transfer line injects the electron bunches into the booster ring in which the electron energy increases to 1.5 GeV for further injection into the storage ring in which the

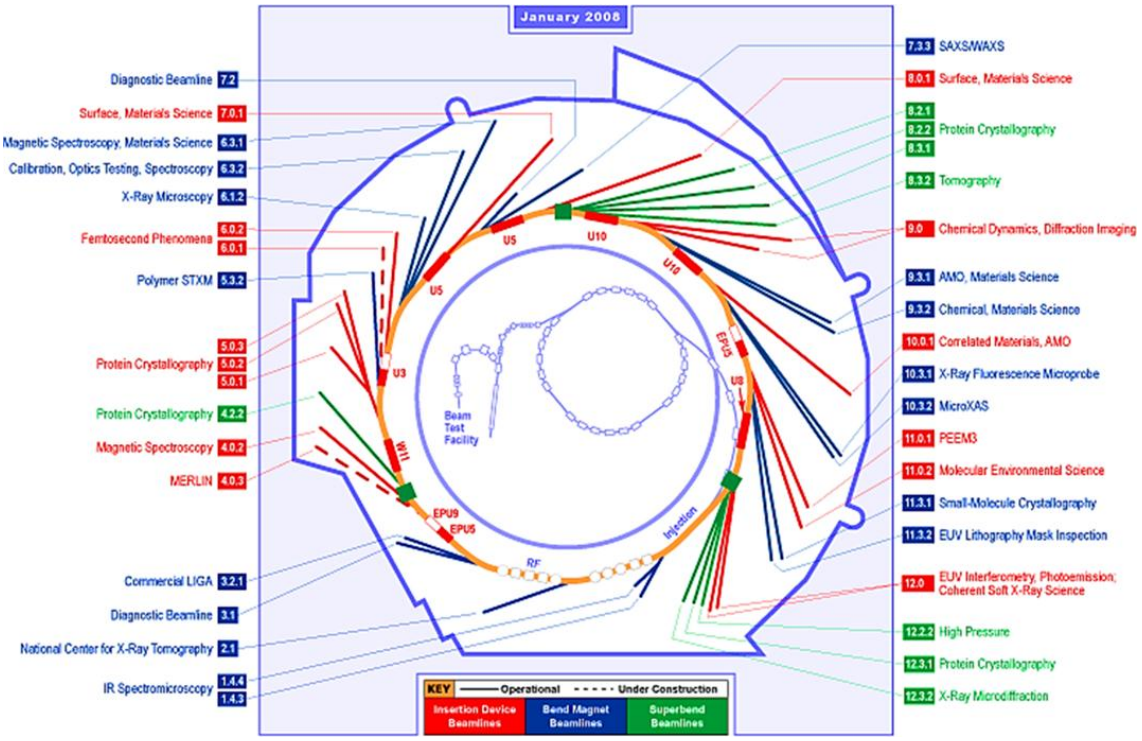

Figure 4.3 Schematic layout of the 200-meter circumference ALS storage ring [118].

electron energy is finally increased to the nominal 1.9 GeV operating energy. The path of the electrons is kept along the desired trajectory by means of various magnetic devices installed around the perimeter of the circular storage ring. Synchrotron radiation is produced as the electrons pass through the bending magnets, undulators and wigglers, and the beamlines are distributed around the circumference of the storage ring at which different experiments may be simultaneously conducted.

4.4 Beamline 10.0.1

A schematic layout of the ALS beamline 10.0.1 is shown in Figure 4.4. It utilizes a 4.55-m-long, 10-cm-period undulator with 43 full periods located in sector 10 of the ALS storage ring. The beamline can provide an intense, well-collimated photon beam (~ 10^{14} photons/s) at very high spectral resolving power ($E/\Delta E \sim 10{,}000$) over the photon energy range from 17 eV to 340 eV [119]. The photon beam from the undulator is horizontally and vertically focused by two spherical mirrors and directed to a spherical-grating monochromator consisting of three parts; a fixed entrance slit, a translating exit slit, and three interchangeable diffraction gratings. The rulings and energy ranges of the three gratings installed in the monochromator at Beamline 10.0.1 are listed in Table 4.1. The fundamental relation governing the diffraction gratings [93] is given by

$$n\lambda = d\,(\sin\alpha - \sin\beta), \qquad (4.4)$$

where n is the diffraction order (n = 0, 1, 2,…), λ is the photon wavelength, d is the groove spacing of the grating, α and β are the incident and diffracted beam angles measured from the grating normal. Only the first order diffraction (n = 1) was used in the present experiment. The photon energy is changed by simultaneously rotating the grating

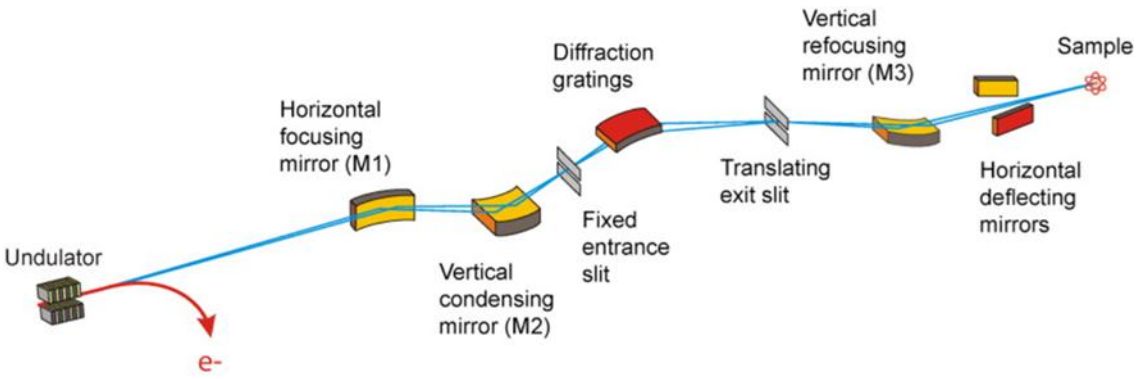

Figure 4.4 Principal optical components of the ALS Beamline 10.0.1 [119].

and adjusting the undulator gap. The photon energy resolution is determined by adjusting the widths of the entrance and exit slits of the mochromator. A third spherical mirror vertically refocuses and directs the beam to the experiment.

Table 4.1 Rulings and photon energy ranges for the three interchangeable spherical gratings installed in the monochromator at beamline 10.0.1.

Grating	Ruling (lines/mm)	Energy range (eV)
Low	380	17 - 75
Medium	925	40 - 160
High	2100	100 - 340

4.4 Electron-Cyclotron-Resonance Ion Source

A 10 GHz all-permanent-magnet electron-cyclotron-resonance (ECR) ion source was developed [94] in order to enable studies of multiply charged positive ions. The production of multiply charged ions by sources of this type is described in detail by Geller [95]. The ECR ion source is a magnetically-confined plasma device in which the cyclotron motion of electrons in a magnetic field is resonantly excited by the injection of microwave radiation. The configuration of the ECR ion source is shown in Figure 4.5. Inside the plasma chamber, the super-heated electrons are confined by a "magnetic bottle" created by an array of permanent magnets. The ECR ion source used at the IPB endstation consists of four permanent ring magnets arranged to create an axial magnetic mirror. The distribution of this field in the mid-plane of the ECR ion source is shown in Figure 4.6. Radial confinement is created by 24 magnets arranged in a hexapole configuration and located between the two inner ring magnets. The frequency for heating electrons is determined by the cyclotron resonance equation:

$$f = \frac{eB}{2\pi m_e} \qquad (4.5)$$

where e and m_e are the charge and the mass of the electrons, respectively. B is the axial magnetic field strength. The value of the strength of this field at the mid-point is 3.6 kG which corresponds to a cyclotron resonance frequency of 10 GHz. A low-pressure gas or vapor injected into the ECR ion source plasma chamber is multiply ionized by successive collisions with the energetic confined electrons in the magnetic bottle.

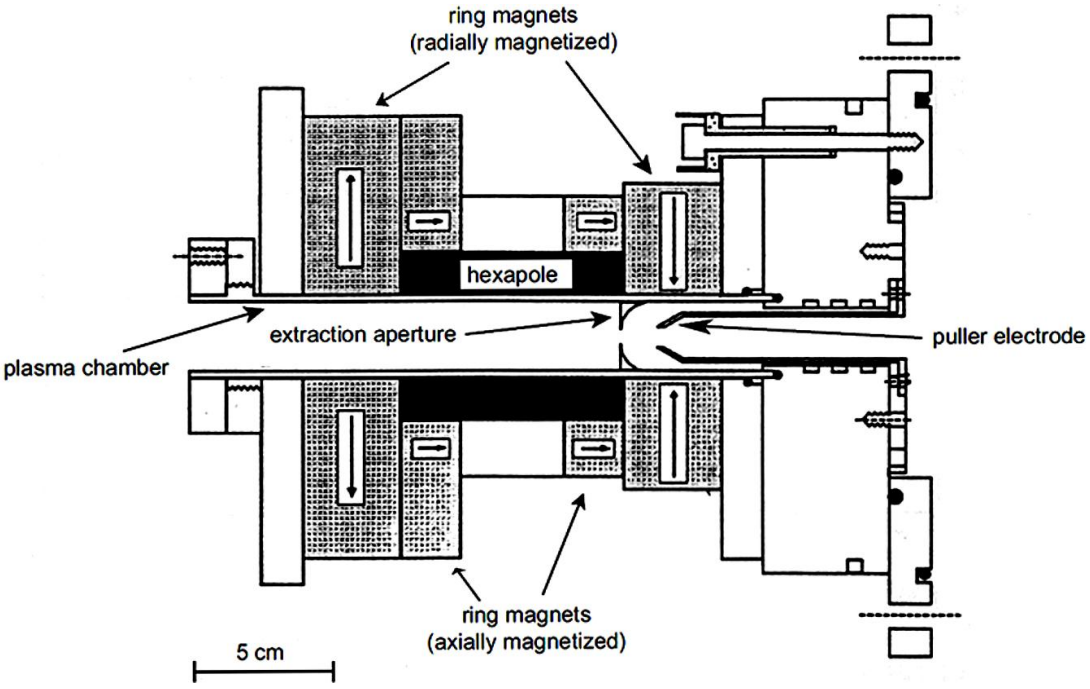

Figure 4.5 Cross section of the ECR ion source installed at Beamline 10.0.1[114].

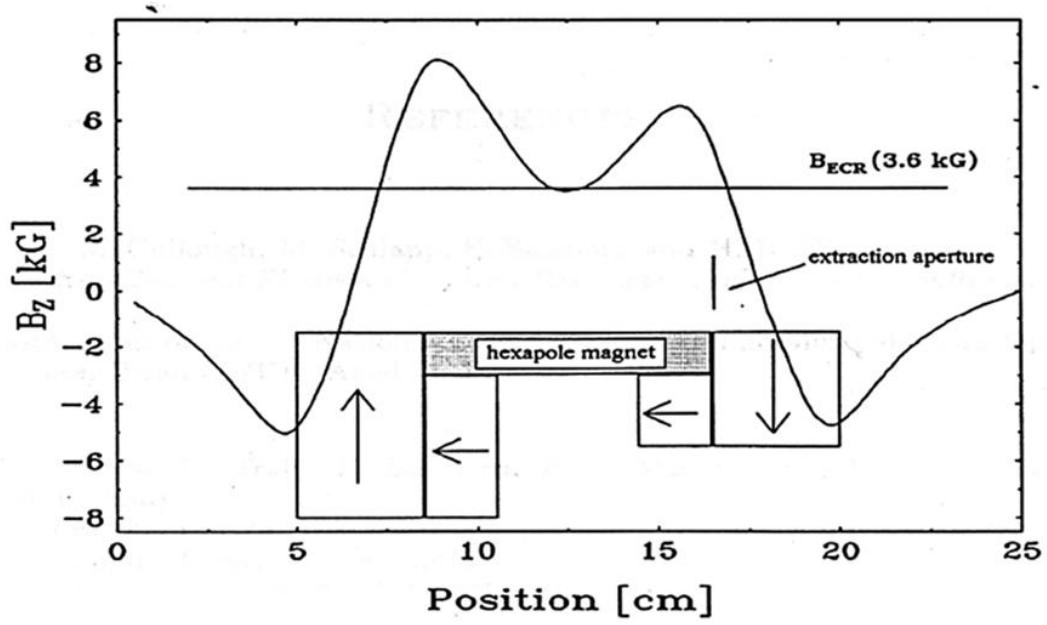

Figure 4.6 Axial magnetic field distribution along the central axis of the 10 GHz ECR ion source [114].

The microwave system consists of a microwave frequency signal generator and an 8-18 GHz traveling-wave-tube amplifier with a maximum continuous-wave output power of 250 Watts. This microwave system is protected from reflected power by a magnetic circulator situated in the waveguide path. The transmitted and reflected powers are monitored by directional couplers connected to RF power meters. The cylindrical plasma chamber into which the microwaves are to be delivered is under vacuum and at high voltage for ion acceleration. It is therefore necessary to make transition from rectangular to cylindrical waveguide, from atmospheric pressure to a typical vacuum pressure of 10^{-7} Torr and from ground potential to typically +6 kV. The pressure and voltage break are accomplished by the use of a commercial Kapton window and a thin (0.2 mm) Mylar sheet respectively which are transparent at 10 GHz. The transition from rectangular to circular waveguide is accomplished by a coupler called a `magic cube' which produces the TM01 mode inside the cylindrical waveguide connected to the plasma chamber. A translatable tuning plunger is installed on one side of the magic cube, which acts as an RF multimode cavity to optimize the coupling of the microwaves into the plasma. The ion source plasma chamber is cooled by a flow of deionized water through a double-walled stainless-steel plasma chamber. A water flowswitch is interlocked to the microwave amplifier to protect the NdFeB permanent magnets that would be irreversibly damaged by thermal demagnetization if a temperature above 40^{0}C were reached. A small resistively heated oven located outside the injection end of the plasma chamber is used to evaporate non-gaseous materials into the ion source plasma discharge.

4.5 IPB Endstation and Merged-Beams Technique

Figure 4.7 shows a schematic diagram of the Ion-Photon-Beam (IPB) endstation installed on ALS beamline 10.0.1. The ECR ion source produces a mixture of ions with different charge states. The mixed ions are extracted and accelerated as a beam through a small aperture by applying 6 kV potential difference between the plasma chamber and the puller electrode. After being extracted from the ion source, ion beam is focused and steered by an einzel lens and two pairs of parallel electrostatic steering plates aligned in the horizontal and vertical directions. A removable Faraday cup located at the center of the chamber that contains the steering plates is available for monitoring the ion beam. In this region, the ion beam contains different charge states of different species, all having the same energy-to-charge ratio (E/q) but different momentum-to-charge ratio. According to their mass-to-charge ratio (m/q), the specific initial charge state of the desired element is selected by a 60^0 dipole analyzing magnet with a pole gap of 10 cm and a bending radius of 59 cm. Mass per charge resolution of this magnet, in combination with the adjustable horizontal and vertical beam slits located before and after it, is adjustable and sufficient to separate ions of different elements, isotopes and charge states.

After selection by the analyzing magnet, the ion beam enters the premerger section equipped with a second einzel lens and set of steering plates. In this section, the ion beam is further focused, steered, positioned, and collimated by these optical elements in order to place the ion beam onto the axis of the photon beam. A pair of spherical electrostatic bending-plates, called the merger, deflects the ion beam horizontally by 90^0 onto the axis of counter-propagating photon beam. A hole in the back plate of the merger allows the photon beam to pass through to a calibrated silicon photodiode that monitors

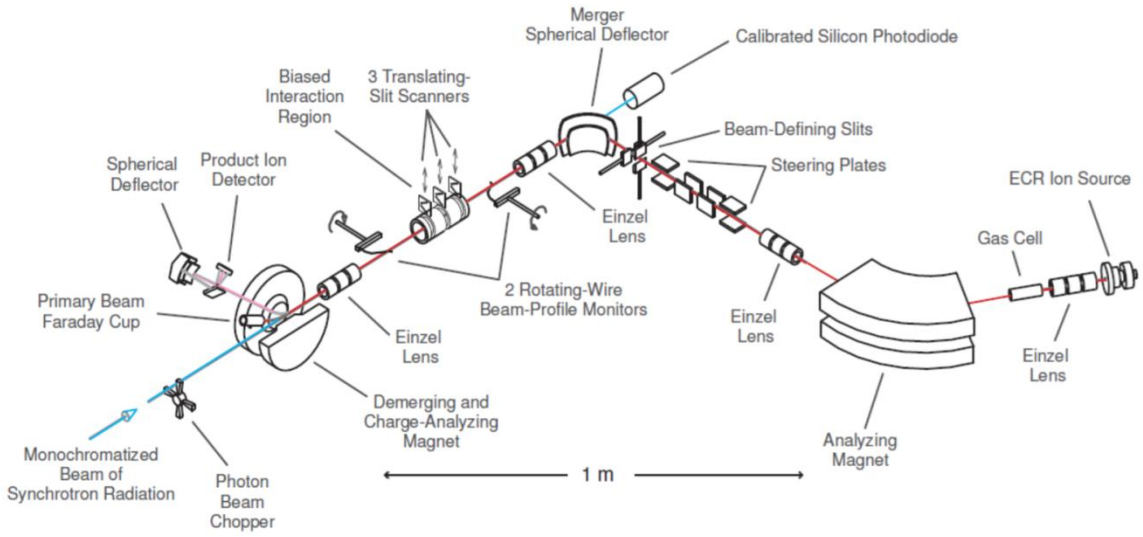

Figure 4.7 Schematic of the IPB endstation located at Beamline 10.0.1 of the Advanced Light Source, LBNL [84].

the photon flux. After the ion beam is deflected onto the photon-beam axis, a third einzel lens refocuses it along the merged path to optimize the spatial overlap of the photon and ion beams. Once the photon and ion beam are merged, photoionization of the primary ion beam produces photo-ions of increased charge. The product photo-ion beam is collinear and co-propagating with the primary ion beam. An additional einzel lens located immediately downstream of the interaction region is used to refocus the product photo-ions to insure that they all reach the signal detector.

For absolute measurements, the ion and photon beams are carefully tuned for overlap within a 29.4 cm-long interaction region, which consists of an electrically-isolated stainless steel mesh cylinder placed at well-defined electrical potential (typically +2 kV). This applied potential produces energy-labeled photo-ions in this region which can be separated downstream from photo-ions produced outside the region. Within the interaction region, three translating slit scanners are located to measure the two-dimensional spatial intensity distributions of interacting beams at three locations along its axis. Two commercial rotating-wire scanners located just upstream and downstream of the interaction region are used to monitor the spatial overlap of the photon and ion beams in real time while aligning the beams. For spectroscopic measurements the interaction region is grounded so the effective interaction region becomes the entire 140 cm merged path length between the merger and demerger.

Downstream of the interaction region, the ion beam is deflected by a 45^0 dipole analyzing magnet, called the demerger, vertically out of the photon path and simultaneously separates the photo-ion product beam from the primary ion beam. As the primary and product ion beams have different charge states, they are deflected through different angles and therefore separated within the demerger magnet. The primary ions are collected by a large Faraday cup and their current is measured by an electrometer. The product ions, having increased charge, are deflected by a larger angle than the primary ions, pass through an aperture in the center of the Faraday cup and are directed to a pair of 90^0 spherical plates. These deflectors deflect and steer the product ions onto a negatively-biased stainless steel plate from which secondary electrons are accelerated into a channeltron detector operated in single-particle mode. Since many secondary

electrons are produced by the impact of each incoming ion on the plate, the efficiency of the channeltron detector is nearly unity. The pulses from the detector are amplified and passed to a constant-fraction discriminator. This produces TTL logic pulses which are registered by a computer-controlled counter. The photo-ion counts from the detector are normalized to the primary-ion-beam and photodiode currents. The photon flux was monitored by a silicon photodiode calibrated by the National Institute of Standards and Technology (NIST). The photodiode current is proportional to the photon flux and was measured by a calibrated picoammeter.

The primary source of background in these experiments is ionization of the primary ion beam due to stripping collisions with residual gas. These ions will make it to the detector and be counted together with the photo-ion signal. In order to reduce this stripping background, ultrahigh vacuum of order of 10^{-10} Torr is maintained in the interaction region. However, this background is still not negligible, and must be subtracted. This was accomplished using a 6 Hz mechanical chopper in the photon beamline which mechanically chops the photon beam on and off. This process allows for the measurement of signal-plus-background when the chopper is on and just background when the chopper is off. By subtracting these two measurements, the photo-ion signal count rate is determined.

4.6 Absolute Photoionization Cross Section Measurement

The IPB endstation has two modes of operation: spectroscopic mode and absolute mode. In spectroscopic mode, the interaction region is grounded so that the full 1.4 m merged-path of the ion and photon beams becomes the effective interaction region, thus maximizing photo-ion yield. During these measurements, photon energies are stepped

across a desired energy range and a photo-ion yield spectrum is recorded as a function of photon energy. In absolute mode, a bias voltage is applied to the interaction region that permits energy-labeling of the product ions and an accurate definition of the volume in which the photon-ion interaction takes place. Depending upon the primary and product ion charges, a positive or negative potential of 1-2 kV was applied to the interaction chamber. The two-dimensional spatial intensity profiles of the photon and ion beam are measured using three translating slit scanners located at the two ends and at the center of the interaction region. These are used to calculate the form factor that quantifies the spatial overlap of the beams, which is needed to determine absolute cross sections.

An advantage of the IPB endstation is that all the parameters needed to calculate absolute photoionization cross sections can be measured experimentally. Cross-section measurements are typically performed at a number of discrete photon energies. These absolute cross sections at selected photon energies may be used to normalize the photo-ion yield spectrum measured in spectroscopic mode. The absolute photoionization cross section, σ (cm^2), can be determined from measurable parameters using the formula:

$$\sigma = \frac{Rqe^2 v_i \epsilon}{I^+ I^\gamma \, \Omega \, \delta \, \Delta \int F(z) dz} \tag{4.6}$$

where R is the photo-ion signal count rate (counts/s), q is the charge state of the parent ion, e is the fundamental charge (1.6 x 10^{-19} C), v_i is the velocity of the primary ion beam within the interaction region (cm/s), ϵ is the quantum efficiency of the photodiode (electron/photon), I^+ is the primary ion beam current measured in the primary beam Faraday cup (A), I^γ is the photodiode current (A), δ is the pulse transmission fraction as

determined by the discriminator setting, Ω is the photo-ion collection efficiency (close to 100%), Δ is the fraction of photo-ions striking the negatively-biased stainless steel plate within the detector apparatus that produce a pulse in the channeltron detector (also typically close to 100%). Similarly, $\int F(z)dz$ is the form factor defining the spatial overlap of the photon and ion beams within the interaction region based on the form factors, $F(z_i)$, as measured by each of the three slit scanners (i = 1, 2, 3). Each slit scanner contains two orthogonal slits that measure the beam intensities along x and y axes. Form factors $F(z_i)$ are determined at three positions z_i along the interaction region axis (4.39 am, 15.38 cm and 26.4 cm from the entrance aperture of the interaction chamber);

$$F(z_i) = \frac{\iint I^{+}(x,y)\, I^{\gamma}(x,y)dxdy}{\iint I^{+}(x,y)dxdy \iint I^{\gamma}(x,y)dxdy} \qquad (4.7)$$

where $I^{+}(x, y)$ and $I^{\gamma}(x, y)$ are the ion and photon beam currents at the position z_i, respectively. To a good approximation, it is assumed that the current densities are separable [96] in the form, $I^{+}(x,y) = I^{+}(x)I^{+}(y)$ and $I^{\gamma}(x,y) = I^{\gamma}(x)I^{\gamma}(y)$. The three individual factors, $F(z_i)$ are then used to obtain the total form factor, $F(z)$, to use in equation 4.6 by interpolation/extrapolation over the full length of the interaction region. The form factors are plotted and fitted to a quadratic function along the path, z through the interaction region. This is typically done using OriginLab 7.5 analysis software which then extrapolates the total form factor as seen in the screenshot of Figure 4.8.

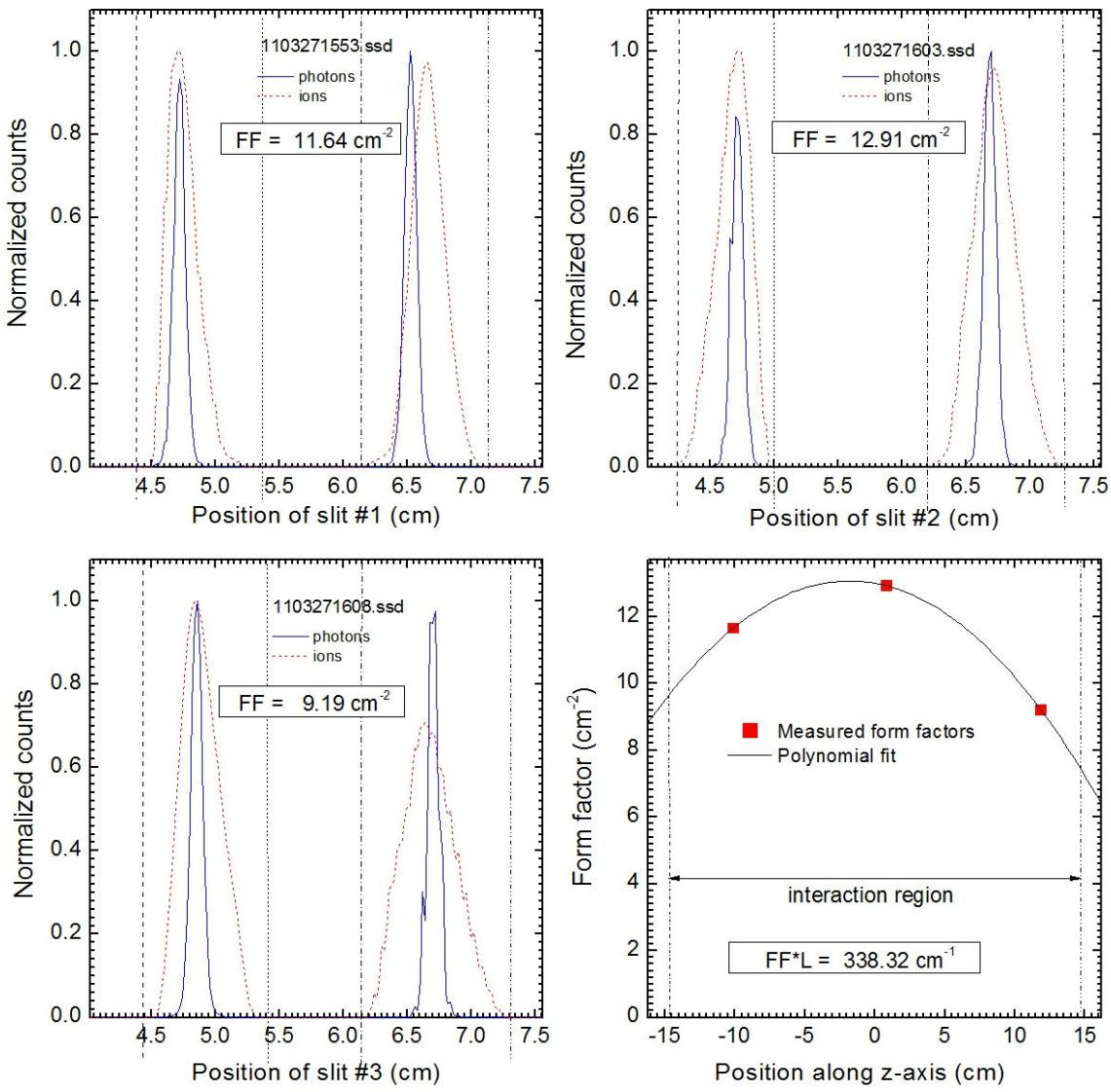

Figure 4.8 Typical beam-intensity profiles for absolute photoionization cross section measurements.

4.7 Experimental Uncertainties

The accuracy of the cross section data is determined by statistical fluctuations and a number of systematic contributions. The major sources of uncertainties in the present measurements include: characterization of photon beam, primary ion beam, and their

spatial overlap; collection of product photo-ions, and statistical uncertainty arising from their collection. The estimated relative and absolute uncertainties in the measurements based on these sources are presented in Table 4.2 [84, 97]. In each case, the total uncertainties are given by the quadrature sums of the individual sources estimated at the 90% confidence level. For the present study, the estimated uncertainty of the absolute measurements is $\pm$ 23%.

Table 4.2 Typical uncertainties in spectroscopy and absolute modes for photoionization cross section measurements estimated at the 90% confidence level.

Source	Spectroscopy	Absolute	Total
Counting statistics	2%	5%	5%
Photo-ion collection efficiency, Ω	-	10%	10%
Photo-ion detection efficiency, Δ	-	3%	3%
Parent ion collection efficiency	-	2%	2%
Ion current measurement, I^+	2%	2%	3%
Photodiode responsivity, ϵ	5%	15%	16%
Photodiode current measurement, I^γ	2%	2%	3%
Beam profile measurement	-	10%	10%
Beam overlap integral, F_L	-	5%	5%
Interaction length, L	-	2%	2%
Quadrature sum	**6%**	**22%**	**23%**

4.7 Photon Energy Calibrations

The three diffraction gratings on the beamline 10.0 are mechanically interchangeable, so the photon energy scale is only reproducible within approximately 0.1% whenever the grating is changed. Thus, in order to determine the photon energy scale with high accuracy, it is necessary to calibrate the photon energy for each experiment using well-known ionization thresholds or resonances. This can be accomplished by using either a gas cell installed on one branch of beamline 10.0 or the IPB endstation. The gas cell is isolated by a thin vacuum window that is installed on a different branch of the beamline that serves this purpose. It contains two parallel conducting plates placed along the photon beam axis over which a potential difference is applied to collect the photo-ions. Normally, the gas cell is filled with neutral gas at mTorr pressure. Photo-ions produced inside the cell are accelerated toward the cathode. A sensitive electrometer measures the photo-ion current collected by the cathode as the photon energy is scanned.

For IPB calibrations, well-known ionization thresholds for ions are typically measured. Since the photon and ion beams are counter-propagating in the IPB endstation, corrections for Doppler effect are necessary to account for the energy shift in the reference frame of the ion beam. This correction is made using the well-known Doppler formula:

$$E_{corr} = E_{nom}\sqrt{\frac{1+v_i/c}{1-v_i/c}} \approx E_{nom}\left(1+\frac{v_i}{c}\right) \tag{4.8}$$

where E_{nom} is the nominal photon energy, E_{corr} is the Doppler-corrected energy, v_i is the speed of the ion inside the interaction region and c is the speed of light. The middle-energy grating was used for photoionization experiments with $Xe@C_{60}^{+}$ ions described in this dissertation, which was calibrated using the Ar ($2p^{-1}_{3/2}$ 4s) resonance in second order (reference energy = 122.195 eV) [98].

Chapter 5

Production of Samples Containing $Xe@C_{60}$ at the ALS

By using an ion beam implantation technique, samples containing $Xe@C_{60}$ were prepared at the Advanced Light Source (ALS) and re-evaporated from a small oven into a low-power argon discharge in the ECR ion source. The endohedral $Xe@C_{60}$ were synthesized from the prepared samples with yields of ~ 10^{-5} and $Xe@C_{60}^{+}$ ion beam currents in the range 0.065 – 0.3 pA were obtained for the proof-of-principle merged-beams experiments with $Xe@C_{60}^{+}$. By optimizing the parameters for synthesis and using isotopically enriched ^{136}Xe for the sample production, endohedral yields as high as 2.5 x 10^{-4} were obtained, increasing the maximum ion beam current for the photoionization measurements to 5.6 pA. Following a brief description of ion beam implantation method used for the synthesis of endohedral fullerenes, the experimental set up developed at the ALS to prepare samples containing $Xe@C_{60}$ and the results are discussed in this chapter.

5.1 Introduction

Among various methods for the production of noble-gas endohedral fullerenes, only a high pressure and high temperature method [52, 99], a nuclear recoil implosion method [54, 55], and a beam implantation method [57] have been used to date for the synthesis of $Xe@C_{60}$ (Table 5.1). The first two methods have been discussed in Chapter 2. This chapter is focused on the beam implantation method which was used for sample production at the ALS.

In the ion implantation method for synthesis of endohedral fullerenes, the atoms to be encapsulated are ionized, accelerated and implanted into a solid fullerene target. Fullerene target molecules are continually exposed to the beam of ions at selected energies so that some of the ions penetrate the fullerene cage and finally produce endohedral fullerenes. Using this method, films of C_{60} containing 30% of endohedral fullerenes incorporating lithium ($Li@C_{60}$) have been routinely produced [100]. Similarly, metal [101], N^+ [102] and rare gas [56, 57] ions have been implanted into fullerenes to produce macroscopic quantities of endohedral fullerenes. Wantanbe et al [57] applied this method for the production of $^{133}Xe@C_{60}$. Fullerene targets were made by vacuum evaporation of fullerenes on Ni foils and by using an isotope separator, ^{133}Xe ions were implanted into the targets. For implantation of these radioactive atoms, the ions were accelerated to 40 keV to be mass-separated from stable isotopes. The yield of $^{133}Xe@C_{60}$ in the prepared sample was found to be 0.025%. Although ion implantation is similar to the nuclear reaction–recoil process, kinetic energy of atoms in this process is significantly lower than that in the nuclear reaction recoil process induced by charged

Table 5.1 Yields for the production of $Xe@C_{60}$ using different methods.

Method	Yield	Reference
High pressure and high temperature	3.0×10^{-4}	Saunders et al. 1994 [99]
High pressure and high temperature (improved with the use of KCN)	3.0×10^{-3}	Syamala et al. 2002 [52]
Beam implantation	2.4×10^{-4}	Wantanbe et al. 2003 [57]
Beam implantation	2.6×10^{-6}	J. Hellhund 2011 [120]
Nuclear recoil implosion	1.4×10^{-8}	Ohtsuki et al. 1998 [55]

particles. However, the ion beam accelerated to such a higher energy (40 keV) still damages fullerene molecules during collision.

Shimshi and collaborators [56] developed an experimental set up for noble gas endohedral production using the ion implantation method. In this technique the fullerenes emerging from an oven heated to 470^0C were continually deposited on a rotating aluminum cylinder and exposed to ions accelerated up to 230 eV to synthesize $He@C_{60}$ and $Ne@C_{60}$. Although this technique was not used to synthesize $Xe@C_{60,}$ a major advantage of the technique over the other methods is that bombarding freshly deposited fullerene surfaces with an accelerated noble-gas ion beam at lower energy

results in ion encapsulation with reduced decomposition of fullerene, and surviving empty or filled fullerenes can be easily separated from the decomposition products. The technique also enhances the yield of endohedral fullerenes during bombarding process by the repeated collision of the same fullerene molecule with ions and increasing the chance of ion penetration. Moreover, this method promises a higher incorporation ratio of the filled to empty fullerene molecules which is not limited by thermodynamic equilibrium constraints.

Samples containing endohedral $Xe@C_{60}$ were also synthesized in Giessen, Germany [120] by developing an ion implanter. Although their apparatus consists of an oven, a large rotating cylinder and a high-current ion thruster for the Xe^+ ion source, the yield of $Xe@C_{60}$ in the sample prepared from their method was only 2.6×10^{-6}.

The goal of all these above mentioned attempts was to produce endohedral $Xe@C_{60}$ with a high yield at an acceptable rate. However, the endohedral $Xe@C_{60}$ were not commercially available as solid samples in quantities sufficient for evaporation into an ECR ion source discharge. The main goal of this study was to prepare solid samples containing $Xe@C_{60}$ in a quantity sufficient for re-evaporation into the ECR ion source discharge, and from which sufficient ion beam current could be extracted for merged-beams experiments to perform photoionization cross section measurements. To achieve this goal, an apparatus was developed at the ALS, based on the ion implantation method reported by Shimshi et al. [56].

5.2 Production of $Xe@C_{60}$ at the ALS and Results

5.2.1 Experimental Set Up

Figure 5.1 shows the schematic diagram of the experimental setup devised by David Kilcoyne at the ALS to synthesize $Xe@C_{60}$ based on the technique developed by Shimshi and collaborators [56]. The major components of this implantation device are a resistively-heated oven, a rotating metal cylinder, and an ion source. The oven in vacuum is used to evaporate fullerene powder so that the emitted vapor is directed onto the

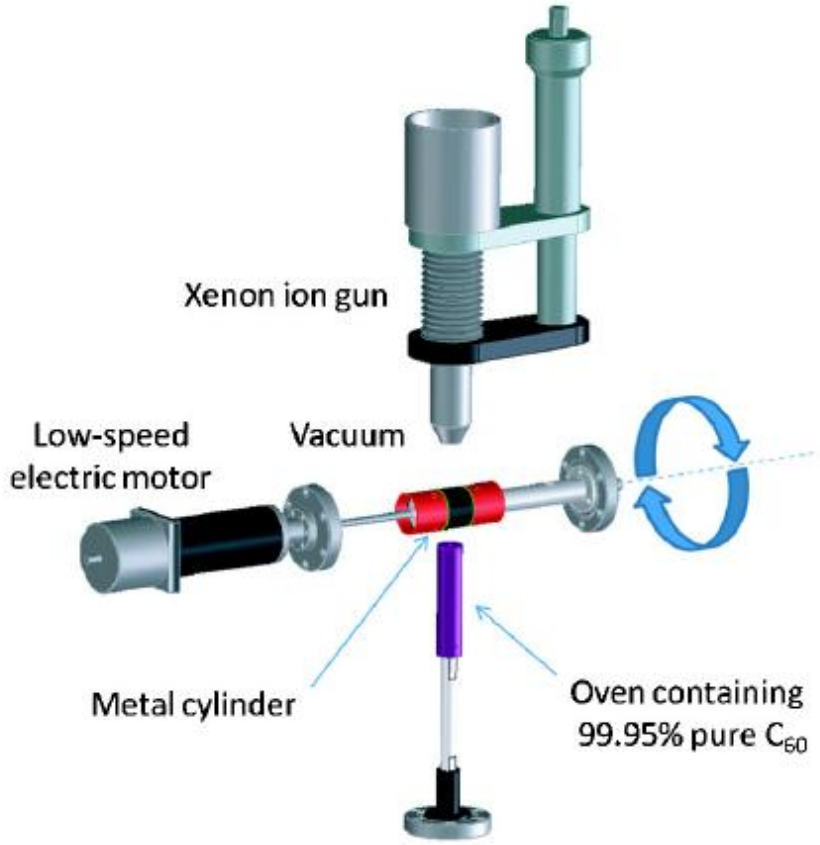

Figure 5.1 The set up developed at the ALS to synthesize $Xe@C_{60}$ based on the method reported by Shimshi et al. [56].

cylindrical target. The cylinder serves as a surface on which the fullerenes should deposit in layers which are exposed to irradiation by accelerated ions. A low speed electric-motor is used to rotate the target cylinder so that the rotating target can provide thin layers of fullerene material to be exposed to the ion beam one after another. An ion sputter gun, which is a combination of an ion source and an electrostatic lens to accelerate and focus ions, directs the ions into the surface of the rotating cylinder. The ion source consists of a filament and an electrostatic plate which serves as an anode. Applying a high voltage to the anode creates an electrostatic field inside the ion source. When xenon gas is injected into the ion source, the high electric field causes the gas to ionize. The ions are then accelerated and focused by an electrostatic lens onto the target cylinder.

5.2.2 Sample Production, Results, and Analysis

For the production of samples containing $Xe@C_{60}$, 99.95% pure C_{60} powder was continually evaporated in the oven and deposited onto the cylinder rotating with very low speed (~ 0.1 Hz). At the same time, a current is passed through the ion source filament, and the electrons emitted are accelerated towards the anode kept at positive high voltage. The pressure of the xenon gas in the source was optimized for maximum ion current. The ions formed are extracted, accelerated and focused onto the rotating cylinder. As the ion energy is a key parameter for the sample production, its value should be chosen within an appropriate range so that the ion could enter through the ring of C_{60} cage but not leave the cage again through the opposite ring or destroy the cage. According to the theoretical prediction of Ohtsuki et al. [55], the ion energy for optimal incorporation of xenon into C_{60} should be around 200 eV. According to their calculations, the energy of a xenon atom

has to be within 130eV and 200eV to penetrate through the middle of a six-membered ring of the C_{60} cage and not to escape through the opposite six-membered ring. So, Xe^+ ion energies in the range from 130 – 200 eV appear to be favorable for the production of $Xe@C_{60}$. Following this prediction, the freshly deposited fullerene layer on the cylinder was continuously irradiated by a typical 4 - 5μA Xe^+ ion beam current with an energy of 150 -200 eV from the ion sputter gun. This process continued for several weeks. After exposing a continuous fullerene vapor beam in vacuum to a continuous Xe^+ ion beam in such a manner for a period of several months, the powder deposited on the cylinder was then scraped from the surface to obtain several tens of mg of sample material.

For mass spectroscopic analysis, the sample powder was then placed into a small oven for subsequent re-evaporation into a low-power Ar discharge in the 10 GHz all permanent electron-cyclotron-resonance (ECR) ion source. In the ECR plasma, at first the sample was ionized, then ions were extracted from the ion source by a potential difference of 6 kV, and finally extracted ions were electrostatically steered and focused. The 60^0 magnetic-dipole mass spectrometer was used to select ions according to their mass-per-charge ratios. The selected ion beam was then registered either by a Faraday cup or by a single-particle detector. Several scans of the magnetic field were performed by closing the ion beam defining slits to resolve the $Xe@C_{60}^+$ peak which was expected just above the C_{70}^+ peak.

Figure 5.2 presents a mass spectrum of the ion beam from the ECR ion source operating at an Ar pressure of 3.5×10^{-6} Torr, microwave power of 1 W and oven power of 12 W. This spectrum was recorded during the photoionization cross section

measurements. In addition to mass peaks of C_{70}^{+} and $Xe@C_{60}^{+}$, the spectrum shows several peaks corresponding to the fragments of C_{70}^{+} and $Xe@C_{60}^{+}$ formed because of successive losses of C_2 dimers within the ion source discharge. Since the source material (99.95% pure C_{60}) for the production of the sample containing $Xe@C_{60}$ also remains as an end product of the process, the main contaminant in the sample is C_{70}. The mass of $Xe@C_{60}$ is slightly higher than that of C_{70} and both are distributed according to the natural isotopic distributions of carbon and xenon.

To identify the $Xe@C_{60}^{+}$, mass spectra of the isotopic pattern of $Xe@C_{60}^{+}$ were also simulated considering the probable combinations of ^{12}C and ^{13}C in C_{60}, and the relative abundances of the 9 stable isotopes of Xe. For the simulation, a script in OriginLab written by S. Schippers was used. The result shows that natural abundances of Xe and C isotopes result in 11 possible mass numbers for $Xe@C_{60}^{+}$ ranging from 848 amu to 858 amu whose fractional abundances exceed 1%. The inset shown in Figure 5.2 compares the measured mass peak to a simulation using these calculated relative abundances for each mass number and a Gaussian function to represent the ion mass spectrometer resolving power estimated to be 280 for the ion beam slit settings used for that measurement.

Theoretically, Xe is predicted to form both internal and external van der Waals bonds with C_{60} thus forming endohedral and exohedral complexes [103]. In the mass spectrum, the position of the mass peak corresponding to the endohedral complex is identical to that of an exohedral complex if it could survive. Evaporating 99.95% pure

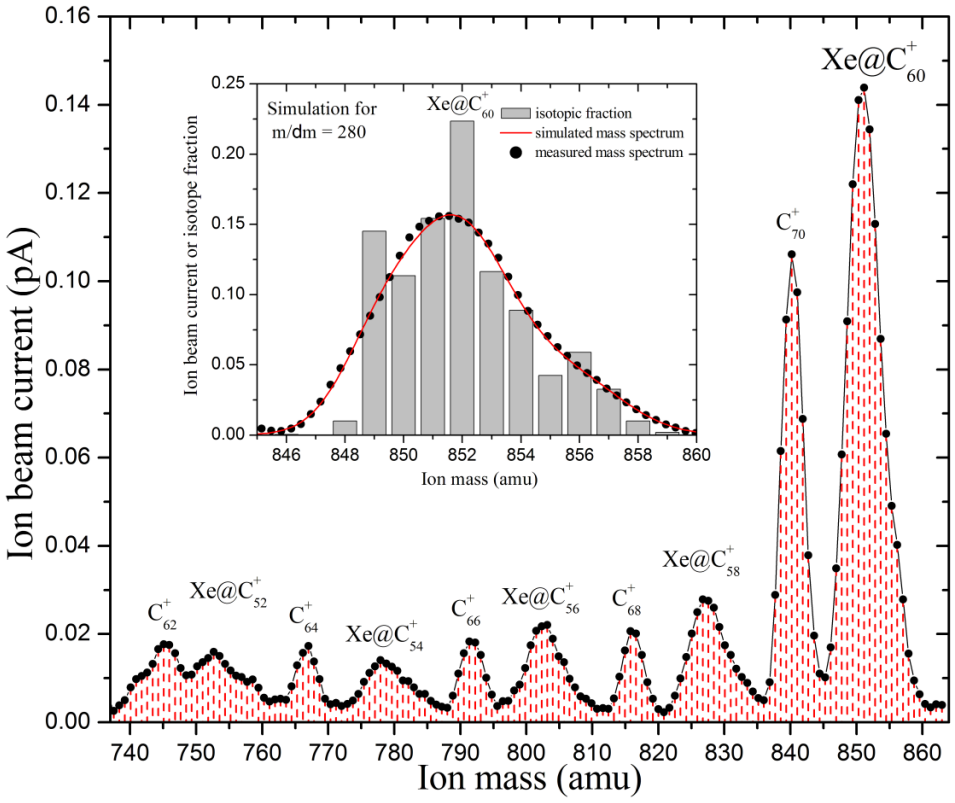

Figure 5.2 Mass spectrum of the ion beam from the ECR ion source operating at an Ar pressure of 3.5 x 10^{-6} Torr, microwave power of 1 W and oven power of 12 W. The inset compares the same $Xe@C_{60}^{+}$ peak measured with smaller steps to a simulated spectrum considering possible combinations of C and Xe isotopes weighted by their natural abundances (histogram) [26].

C_{60} into the ECR ion source discharge results in C_{58}^{+} and C_{56}^{+} ion beam currents that are typically 15% of the C_{60}^{+} ion beam current. It is also evident from the mass spectrum that the situation is similar for C_{70}^{+} with successive losses of C pairs, giving rise to C_{68}^{+}, C_{66}^{+}, etc., as shown in Figure 5.2. Survival of exohedral $Xe@C_{60}^{+}$ in such a plasma environment in which multiple pairs of C atoms are so readily removed from the C_{60}^{+} and C_{70}^{+} cages seems unlikely. Therefore, the $Xe@C_{60}^{+}$ ion beam was considered to consist

predominantly of endohedral molecular ions, although this could not be verified directly since the endohedral and exohedral fullerenes have identical masses.

The fraction of the C_{60} molecules in the sample containing a xenon atom gives the $Xe@C_{60}$ yield. By measuring the ion currents of C_{60}^{+} and $Xe@C_{60}^{+}$ beams on the Faraday cup, the yields of $Xe@C_{60}$ were estimated to be about ~ 10^{-5}. Such a very small fraction of the C_{60} molecules in the accumulated samples containing xenon atom was sufficient to produce pure mass per charge analyzed beams of $Xe@C_{60}^{+}$ ions with currents in the range 0.065 – 0.3 pA. Although the statistical precision of the photoionization results was limited by the extremely small ion currents that could be achieved, it was nevertheless possible to measure the photoionization cross section of $Xe@C_{60}^{+}$ for the first time [26], as will be described in next chapter.

Motivated by these encouraging results, a major effort was devoted to prepare samples with increased $Xe@C_{60}$ yield to produce more ion beam current for the photoionization cross section measurements. In this effort, isotopically enriched ^{136}Xe was used instead of natural Xe for the sample production and the parameters for the synthesis, such as Xe^{+} ion beam energy, rotation speed of the cylinder, and C_{60} evaporation rate were optimized systematically. The resulting ion beam mass spectra from both of these approaches are shown in Figure 5.3.

The Figure 5.3 compares the high resolution mass spectra of the $Xe@C_{60}^{+}$ ion beam produced from the samples using natural xenon with those using highly enriched ^{136}Xe by registering ions on a single-particle detector. The upper panel of Figure 4.3 shows eleven mass peaks of $Xe@C_{60}^{+}$ ranging from 848 amu to 858 amu. The

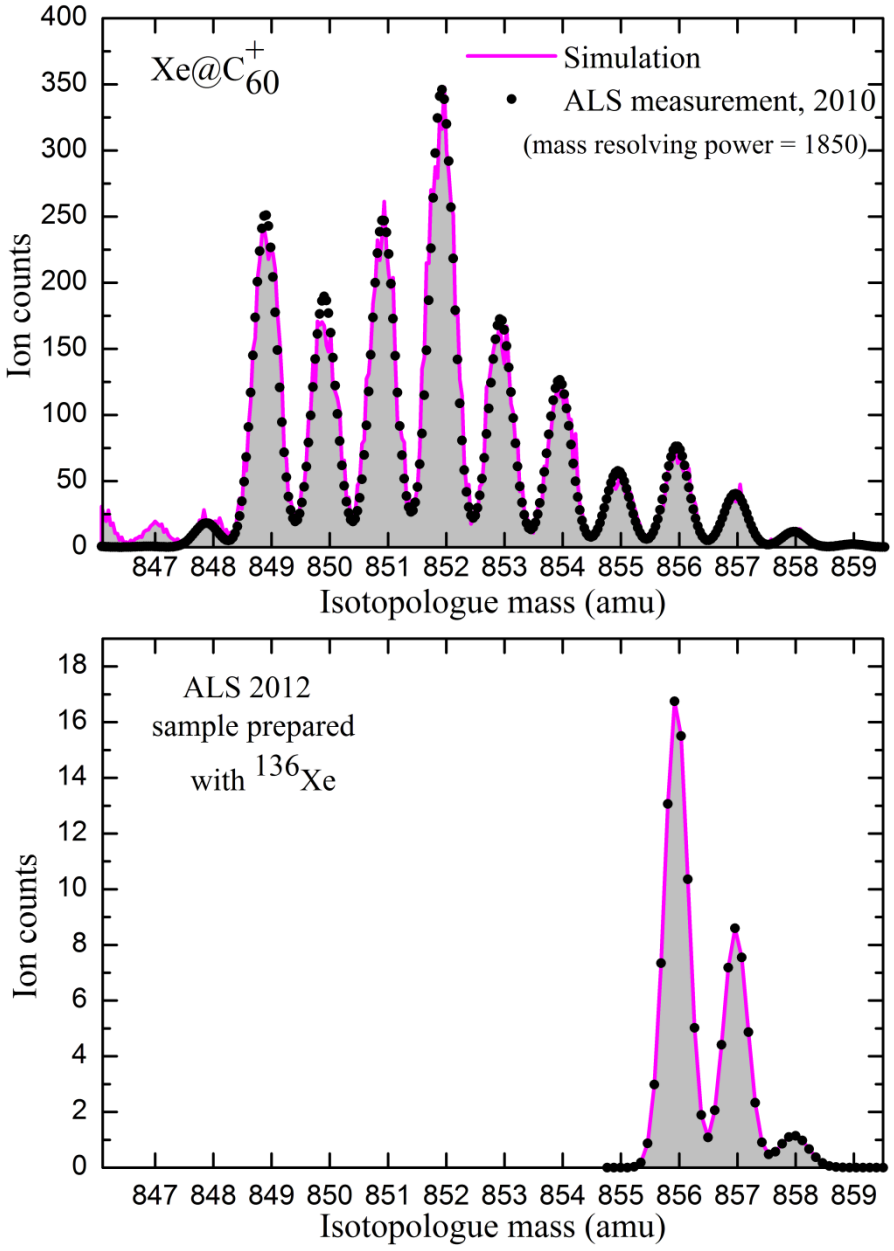

Figure 5.3 Ion mass spectra measured at high resolution using narrow ion-beam defining slits and a single-particle detector. Upper panel, results for samples prepared with a natural mixture of Xe isotopes, consists of 11 endohedral peaks as the result of combination of C and Xe isotopes. Bottom panel, results for samples prepared with highly enriched ^{136}Xe, consist of 3 peaks corresponds to $^{136}Xe@C_{60}$ containing zero, one and two ^{13}C atom.

endohedral peak thus formed was broad with lower maximum intensity and wider than the C_{70} peak (as in Figure 5.2) because of the different Xe isotopes present. At lower mass resolution, the endohedral peak could not be well separated from the C_{70}^{+} peak which was the major contaminant in the 99.95% pure C_{60} material used in the synthesis. To resolve the endohedral peak, ion beam defining slits were further closed, but the process resulted in lower ion beam current. The bottom panel of figure 5.3 shows the measured high resolution mass spectrum of the $^{136}Xe@C_{60}^{+}$ ion beam consisting of only three endohedral mass peaks corresponding to the combination of ^{136}Xe and C_{60} with the two isotopes of carbon. The overall endohedral peak $^{136}Xe@C_{60}^{+}$ thus formed in the ion mass spectrum was narrowed, resulting in a significant increase in the maximum ion beam current (as in bottom panel of Figure 5.3). Due to the absence of mass peaks corresponding to the other natural isotopes of Xe, the $^{136}Xe@C_{60}^{+}$ peak was well-separated from that of C_{70}^{+} even at much lower mass resolution. This allowed the ion beam defining slits to be opened wider, further increasing the ion beam current available for a photoionization cross section measurement.

The intensity of the ion beam current depends not only on the quality of the samples prepared but also on operating parameters for the ECR ion source discharge and various tuning parameters. Among them, the oven power is one that influences the intensity of the ion beam. Figure 5.4 presents the intensity of $Xe@C_{60}^{+}$ ion beam current as a function of increasing oven power (upper panel) and total operating time of the ion source with a typical sample material (lower panel). It was observed that $Xe@C_{60}^{+}$ beams

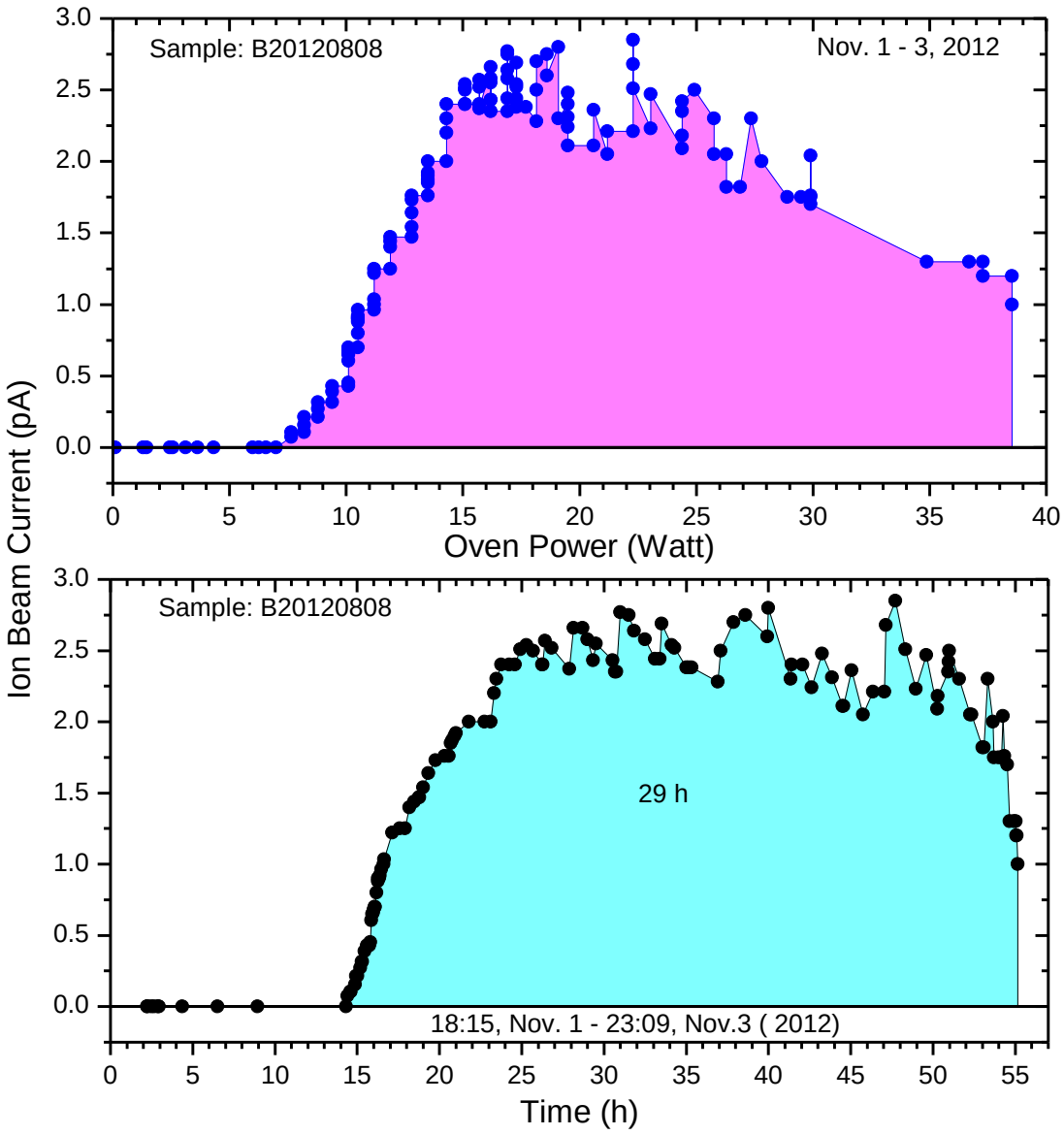

Figure 5.4 Intensity of $Xe@C_{60}^{+}$ ion beam current from a typical sample material, as a function of oven power and the total operating time of the ion source.

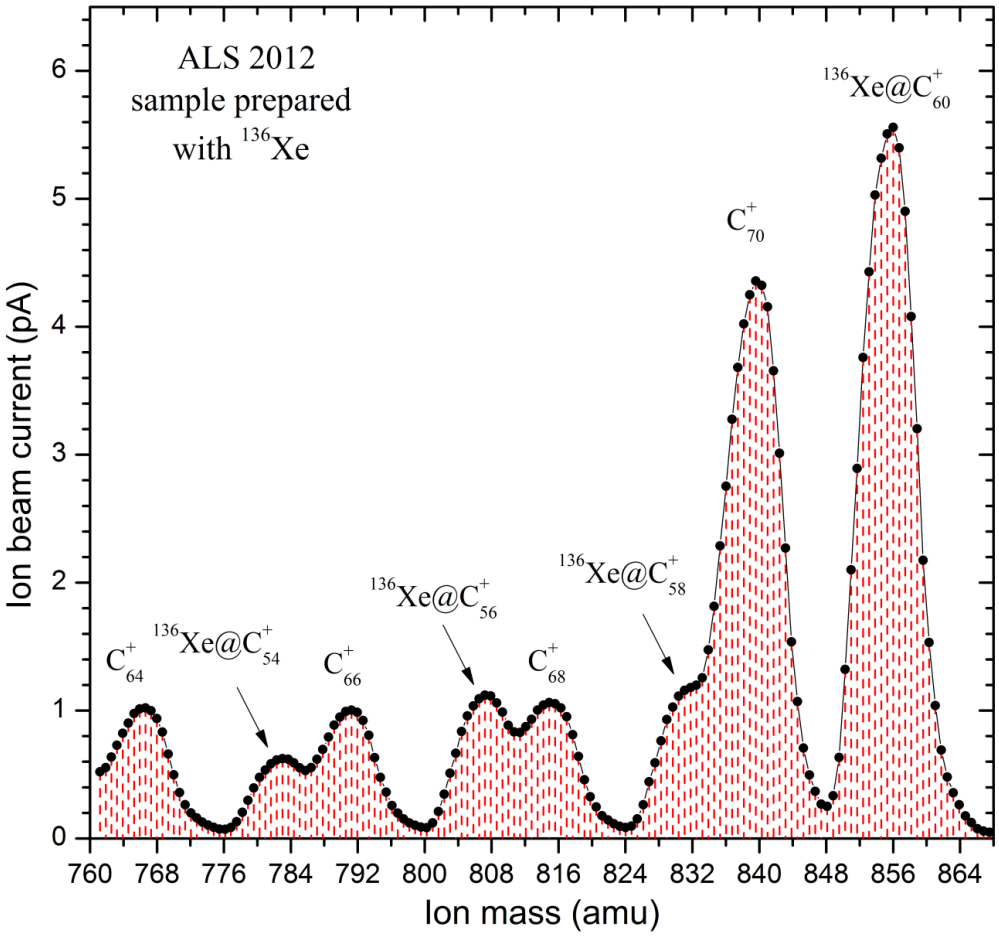

Figure 5.5 Ion beam mass spectrum at low mass resolution from the samples prepared with highly enriched ^{136} Xe. The $^{136}Xe@C_{60}^{+}$ ion beam current for merged-beams measurements was increased by a factor of 40 compared to natural $Xe@C_{60}^{+}$.

appear at an oven power of about 7 W. With increasing oven power the ion beam intensity was found to increase and a constant current of about 2.5 pA was maintained for 29 h. A RF power of 1 W was typically used to sustain a discharge which has little influence on the oven heating. The operating time of the ion source was limited by the

amount of the sample material in the oven and the oven power. At oven power in the range of 10 W – 25 W, the $Xe@C_{60}^{+}$ ion beam was found to be stable with sufficient beam intensity for the photoionization measurements.

Figure 5.5 shows the mass spectrum of the ion beam using samples containing $^{136}Xe@C_{60}$ with widely opened beam defining slits during the photoionization cross section measurements. The $^{136}Xe@C_{60}^{+}$ peak was well separated from the C_{70}^{+} peak even at much lower mass resolution. As expected, the width of $^{136}Xe@C_{60}^{+}$ peak is comparable to that of C_{70}^{+} peak. By comparing the C_{60}^{+} and $Xe@C_{60}^{+}$ ion beam currents, the endohedral $^{136}Xe@C_{60}$ yield in the prepared samples was estimated to be about 2.5×10^{-4}, and the peak ion beam current available for a merged-beams measurement was 5.6 pA, which is 40 times greater than the current used for the proof-of-principle measurements.

5.3 Summary

The endohedral $Xe@C_{60}$ was synthesized at the ALS using the ion beam implantation technique. The endohedral $Xe@C_{60}$ yield in the prepared samples was increased from 1×10^{-5} to 2.5×10^{-4} by optimizing the parameters for synthesis and by using isotopically enriched ^{136}Xe for sample production; thereby the ion beam current available for merged-beams experiments was increased from 0.14 pA to 5.6 pA. Subsequent photoionization cross section measurements for $Xe@C_{60}^{+}$ with these ion beam currents will be presented in the next chapters. Although the yields of $Xe@C_{60}$ in the samples prepared by the ALS method are still low, their values are comparable with those obtained from other techniques [57, 99]. The yield of $Xe@C_{60}$ obtained from an improved high pressure and high temperature method [52] with the use of a potassium

cyanide (KCN) and C_{60} mixture for sample production is higher than that obtained from the ALS samples by an order of magnitude but, the quantity of material produced is smaller. Although the Giessen apparatus [120] produces samples in quantities during short periods, their yield is 2.6×10^{-6}, which is an order of magnitude less than that of ALS samples.

The results demonstrate the feasibility of the ALS set up and technique in preparing solid samples with an acceptable yield of endohedral $Xe@C_{60}$ in quantities sufficient for photoionization cross section measurements. This technique has some advantages over other techniques which include: irradiating freshly deposited fullerene layers with an accelerated Xe^+ ion beam at lower energy results ion encapsulation with reduced decomposition of the empty C_{60} cage; the ratio of filled to the empty fullerene molecules is not limited by thermodynamic equilibrium constraints [56]; re-evaporating the sample in an oven into an ECR ion source discharge allows ions of unused or surviving empty C_{60} and endohedral $Xe@C_{60}$ to be easily separated by mass spectroscopy. Despite these advantages the technique is relatively time consuming as a period of several months is required to prepare samples of several tens of mg sufficient for merged-beams experiments.

Chapter 6

Single and Double Photoionization with Fragmentation of $Xe@C_{60}^{+}$ Molecular Ions

This chapter presents cross section measurements for single and double photoionization with fragmentation of the $Xe@C_{60}^{+}$ ion performed in 60-150 eV photon energy range. Confinement resonances associated with photoabsorption by a Xe atom in a C_{60}^{+} cage, were observed in double photoionization with fragmentation of $Xe@C_{60}^{+}$ and published [26]. These proof-of-principle experiments were performed for $Xe@C_{58}^{3+}$ photo-ion product. However, their statistical precision was limited by extremely small $Xe@C_{60}^{+}$ ion beam currents in the range 0.065 – 0.3 pA. Results with improved statistical precision were achieved in cross section measurements performed with increased $^{136}Xe@C_{60}^{+}$ ion beam current (described in Chapter 5). Since the $Xe@C_{58}^{3+}$ product channel accounted for only about 15% of the total Xe 4d oscillator strength, remaining oscillator strength was investigated with additional measurements for $Xe@C_{60-2n}^{2+}$ (n = 0, 1), and $Xe@C_{60-2n}^{3+}$ (n = 0, 1, 2, 3) photo-ion products. Absolute photoionization cross sections for empty-cage C_{60}^{+} yielding C_{60-2n}^{2+} and C_{60-2n}^{3+} were measured, to which relative cross sections for endohedral ions were normalized.

Confinement resonances associated with photoabsorption by a Xe atom in a C_{60}^{+} cage, were observed in the measured products from double photoionization with fragmentation of $Xe@C_{60}^{+}$. About 62% of total oscillator strength of Xe 4d was found to be distributed among the measured product channels. However, no signature of Xe 4d was observed in single photoionization with fragmentation of $Xe@C_{60}^{+}$.

6.1 Introduction

Xenon atoms have a filled 4d inner subshell and are well known to exhibit a 4d giant resonance in photoionization [20, 80,104]. A number of theoretical calculations of the Xe 4d giant resonance in photoionization of $Xe@C_{60}$ using different approximations predict a significant redistribution of the Xe 4d oscillator strength as a function of photon energy relative to that for a free Xe atom. The well-known single, giant 4d photoionization resonance in the Xe atom has been predicted to be significantly distorted by the spherical C_{60} cage in endohedral $Xe@C_{60}$, producing distinct maxima and minima that have been termed "confinement resonances" [10, 13-16, 18]. The phenomenon results from multipath interference of Xe 4d photoelectron waves that may be transmitted or reflected by the fullerene cage. Figure 6.1 compares a sampling of the predictions for photoionization of $Xe@C_{60}$ with the cross section for 4d photoionization of a free Xe atom.

To study the predicted confinement resonances, measurements of photoionization of $Xe@C_{60}^{+}$ were performed in the photon energy range 60 - 150 eV. For these measurements, a mass-analyzed 6 keV beam of $Xe@C_{60}^{+}$ ions was merged onto the axis of a counter-propagating beam of monochromatized synchrotron radiation. The beams interacted over a common path of 140 cm, after which a dipole magnet demerged the primary and product ions from the photon beam and separated them according to their charge/ mass ratio. The product ions yielded by photoionization of $Xe@C_{60}^{+}$ were counted by a single particle detector as the energy of the photon beam was stepped over the range 60–150 eV at 0.5 eV intervals.

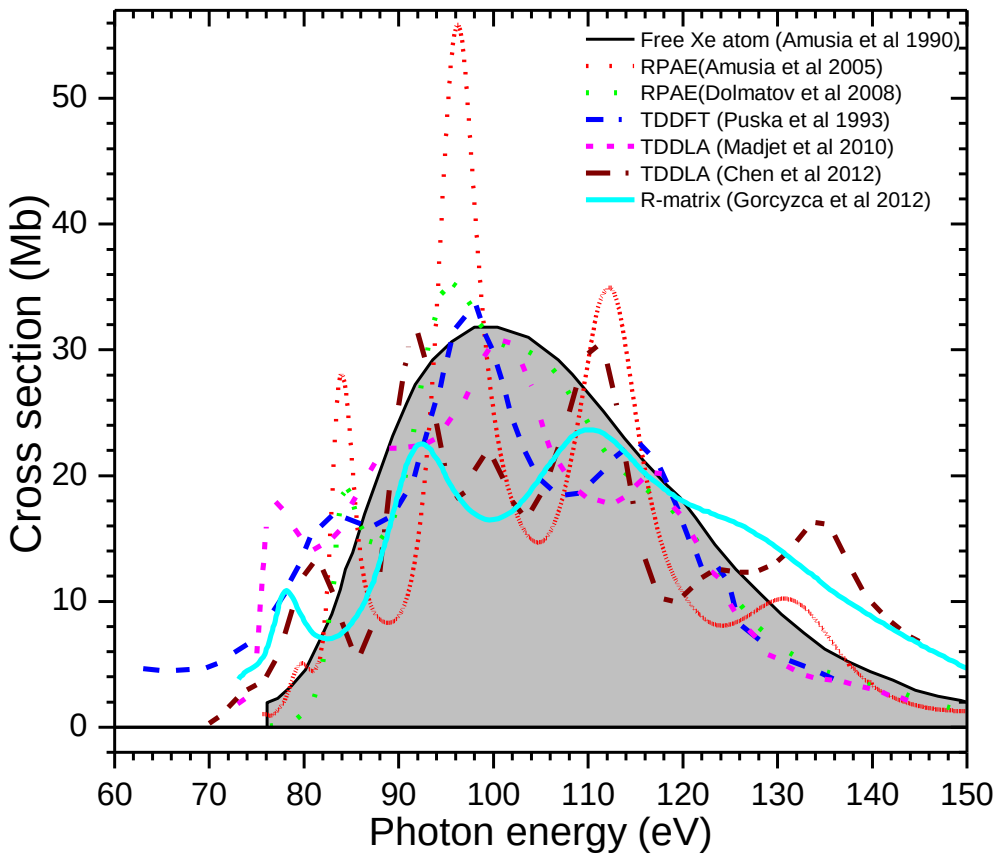

Figure 6.1 Theoretical calculations of the cross sections for photoionization of a free Xe atom by Amusia et al. [20], and endohedral Xe@C_{60} by Amusia et al. [13], Dolmatov et al. [14], Puska et al. [10], Madjet et al. [15], Chen et al. [16], and Gorcyzca et al. [18] showing the predictions in different approximations for redistribution of Xe 4d oscillator strength due to confinement resonances.

6.2 Absolute Cross Section Measurements for Photoionization with Fragmentation of C_{60}^{+}

The C_{60}^{2+} photo-ion yield was recorded as the photon energy was scanned over the ranges 18 – 70 eV and 60 – 150 eV with 0.5 energy steps. Individual scans were joined together to create single photoionization spectrum. Absolute cross section measurements were made independently for single photoionization of C_{60}^{+} [121] and

were used to normalize the present spectroscopic measurements. The resulting normalized spectrum is shown in figure 6.2. From this graph, values of absolute cross sections corresponding to 65 eV, 75 eV, 90 eV, 105 eV, 120 eV, and 140 eV were selected and used to calculate the cross sections for photoionization with fragmentation of C_{60}^{+} yielding various products.

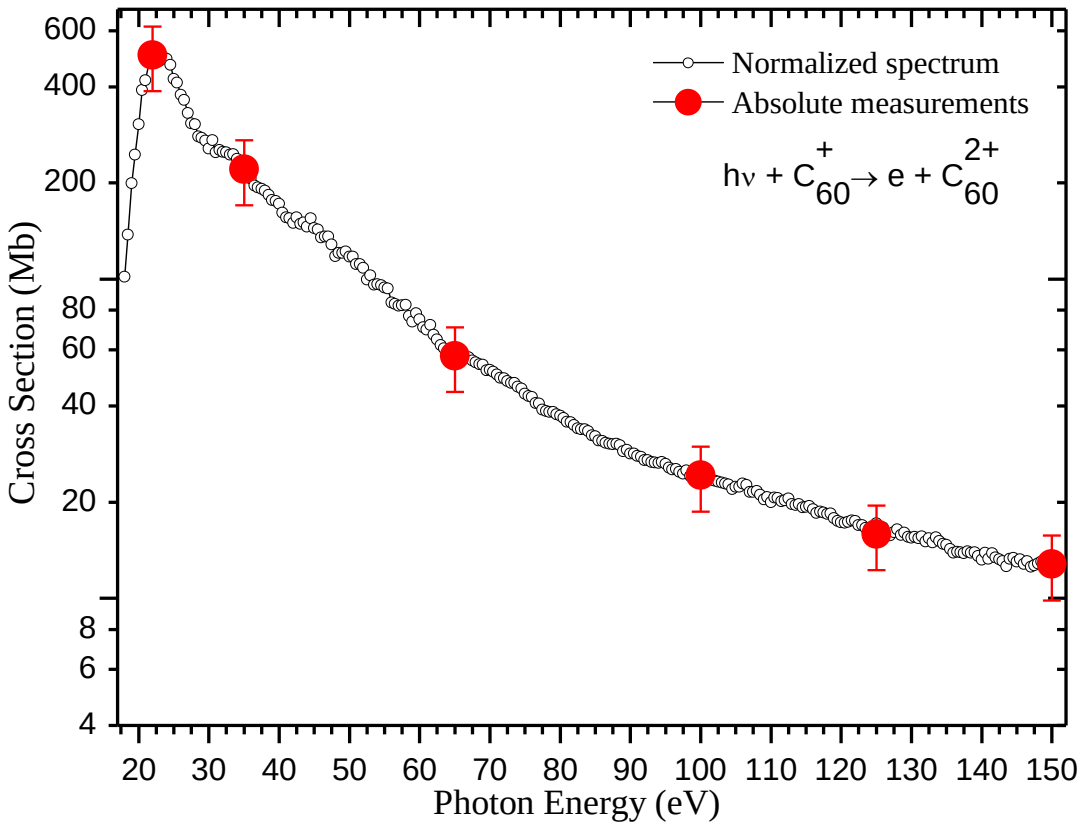

Figure 6.2 Single photoionization cross section measurements for C_{60}^{+}. Solid circles with error bars are absolute measurements with absolute uncertainties estimated to be ±23 %.

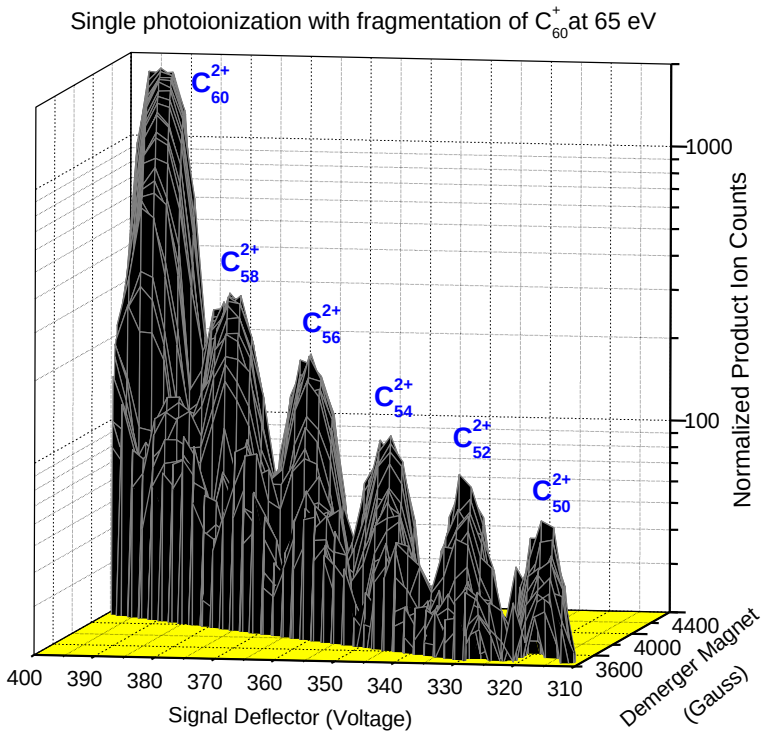

Figure 6.3 Two dimensional mass spectrum of photo-product yield from single photoionization and fragmentation of C_{60}^{+} at photon energy of 65 eV.

Fragmentation of fullerene molecules also occurs with successive ejection of pairs of carbon atoms as a result of its interaction with EUV photons. Figure 6.3 presents a two dimensional mass spectrum of product ions registered by single-particle detector, resulted from single photoionization and fragmentation of C_{60}^{+} at photon energy of 65 eV, by scanning the demerger magnet and spherical deflector plates simultaneously. Mass peaks of doubly-ionized photo-fragments resulting from single ionization of C_{60}^{+} accompanied by loss of several pairs of carbon atoms are well resolved. Adjustable slits at the entrance of the product ion detector in the IPB endstation permitted an increase in mass resolution which is sufficient to isolate these photo-fragmentation products in the experiments.

Table 6.1 Measured absolute cross sections for single photoionization of C_{60}^{+} and cross sections for C_{60}^{+} yielding different products determined from measured signal ratios under identical conditions. Absolute uncertainties in the tabulated values are estimated to be $\pm$ 23%.

Photon energy (eV)	Cross sections for products (Mb)					
	C_{60}^{2+}	C_{58}^{2+}	C_{60}^{3+}	C_{58}^{3+}	C_{56}^{3+}	C_{54}^{3+}
65	57.5	13.36	5.52	2.84	2.67	1.19
75	43.8	9.94	4.89	2.62	2.63	1.55
90	28.4	6.02	3.82	2.07	2.05	1.31
105	22.4	5.14	3.58	1.90	1.90	1.21
120	17.3	3.92	2.64	1.45	1.40	0.87
140	13.2	3.04	1.87	1.03	1.02	0.64

Results from the preliminary measurements with empty C_{60}^{+} ions shown in figure 6.3 indicated that photoionization accompanied by loss of one or more pairs of carbon atoms has significant probability in the photon energy range of interest. Therefore, product-ion signal count rates were measured under identical experimental conditions for the C_{60}^{2+} product and other various products resulted from photoionization and fragmentation of C_{60}^{+}. The signal count rates for each product ion were compared to those for C_{60}^{2+} products, and cross sections for C_{60}^{+} yielding various photo-ion products (Table 6.1) were computed to place them on an absolute scale based on following equation:

$$\sigma_R = \frac{S}{S_{12}} * \sigma_{12} \qquad (6.1)$$

where σ_R is the relative cross section, S is the photo-ion product signal count rate, and S_{12} and σ_{12} are the C_{60}^{2+} signal count rate and the absolute cross section for single photoionization of C_{60}^{+} (Figure 6.2).

6.3 Cross Section Measurements for Single Photoionization of $Xe@C_{60}^{+}$ Yielding $Xe@C_{60-2n}^{2+}$ (n = 0, 1) Products

Product ions $Xe@C_{60}^{2+}$ obtained from single photoionization of $Xe@C_{60}^{+}$were scanned as the energy of the photon beam was stepped over the range 60–150 eV at 0.5 eV intervals, with a primary ion beam current of about 1.6 pA. Since photon beam was not chopped, background counts (0.05 Hz) were measured and subtracted. Under similar conditions, energy scans for single photoionization of empty C_{60}^{+} cage were also recorded. Photo-ion spectra for $Xe@C_{60}^{+}$ and C_{60}^{+} were normalized to the absolute cross sections measured at 65 eV, 75 eV, 90 eV, 105 eV, 120 eV, and 140 eV (Table 6.1). Measured cross sections for the single ionization of $Xe@C_{60}^{+}$ and C_{60}^{+} placed on absolute scale are shown in upper panel of Figure 6.4. The result shows no Xe 4d signature in the single ionization of $Xe@C_{60}^{+}$ as it matches the empty cage measurements within experimental uncertainties. This result was expected, since 4d ionization of Xe leaves an inner subshell vacancy that decays predominantly by autoionization giving a net double ionization.

Since the cage of the endohedral fullerene is transparent to the incident EUV photons, most of the absorption oscillator strength of the 4d electrons in the encapsulated Xe is expected to be distributed into decay channels involving other than the net single ionization. The cross section measurements for the single photoionization with

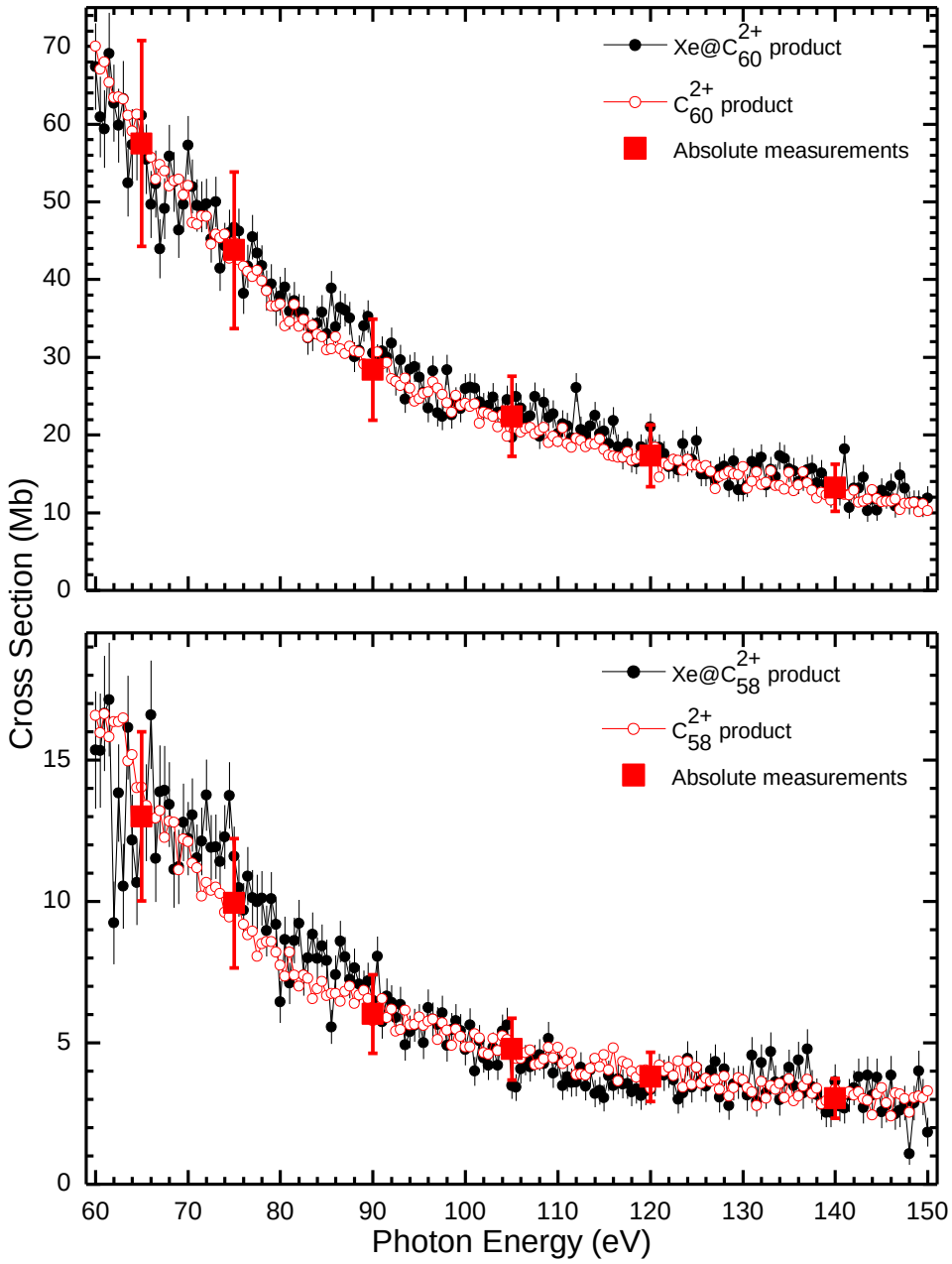

Figure 6.4 Single photoionization and fragmentation of endohedral $Xe@C_{60}^{+}$ (solid circles) and empty C_{60}^{+} (open circles) molecular ions: upper panel for $Xe@C_{60}^{2+}$ and lower panel for $Xe@C_{58}^{2+}$ products. Vertical error bars on solid circles represent statistical uncertainties and those on solid squares represent absolute uncertainties. No evidence of Xe 4d contribution in single photoionization of $Xe@C_{60}^{+}$ was observed.

fragmentation of $Xe@C_{60}^{+}$ and C_{60}^{+} were also performed under similar conditions. The well- resolved measurements with $Xe@C_{58}^{2+}$ and C_{58}^{2+}product signals were recorded over the range 60 – 150 eV with 0.5 eV step size. The recorded spectrum of $Xe@C_{58}^{2+}$ product was normalized to the spectrum of C_{58}^{2+}. Cross sections were placed on absolute scale and the results are shown in lower panel of Figure 6.4. Again, results from these preliminary measurements for single ionization with fragmentation of $Xe@C_{60}^{+}$ do not show evidence of significant excess Xe 4d contribution over the empty C_{60}^{+} cage measurements.

Results from measurements for single photoionization with fragmentation of $Xe@C_{60}^{+}$ yielding $Xe@C_{60-2n}^{2+}$ (n = 0, 1) showed no signature of a Xe 4d contribution. The absence of such signature could be the results of interaction of the ejected Xe electron with the cage. Electron capture, electron-impact ionization, and fragmentation subsequent to photoionization of the encapsulated Xe could occur as relaxation processes. The measurements of photoionization of a free Xe atom in this photon energy range showed that the direct ejection of one 4d electron creating a vacancy decays mainly by Auger electron emission resulting in net double photoionization as the dominant process [105]. Based on these results of the preliminary measurements for single ionization with fragmentation of $Xe@C_{60}^{+}$, it was inferred that the Xe 4d oscillator strength was associated with other product channels, most likely double photoionization, without and with fragmentation of the C_{60} cage releasing pairs of C atoms.

6.4 Cross Section Measurements for Double photoionization with Fragmentation of $Xe@C_{60}^{+}$ Yielding $Xe@C_{60-2n}^{3+}$ (n = 0, 1, 2, 3) Products

Measurements for double ionization with fragmentation of $Xe@C_{60}^{+}$ molecular ions were made for four different product channels and the reactions are represented by the following equation.

$$\gamma + Xe@C_{60}^{+} = 2e + 2nC + Xe@C_{60-2n}^{3+} \ (n = 0, 1, 2, 3) \qquad (6.2)$$

Results from the measurements for different product channels are described separately in the following sub-sections.

6.4.1 Double Photoionization and Fragmentation of $Xe@C_{60}^{+}$ Yielding $Xe@C_{58}^{3+}$

6.4.1.1 Proof-of Principle Experiment

Cross section measurements for double photoionization of $Xe@C_{60}^{+}$ with fragmentation yielding $Xe@C_{58}^{3+}$ were performed and Xe 4d contributions with oscillatory structures were observed for the first time [26]. These measurements are briefly described here as the proof-of-principle experiment. In this experiment, the $Xe@C_{58}^{3+}$ product ions were recorded as the energy of the photon beam was stepped over the range 60–150 eV at 2 eV intervals with a spectral resolution of approximately 0.2 eV. The measurements were taken with a $Xe@C_{60}^{+}$ primary ion beam current ranging from 0.06 to 0.3 pA and a $Xe@C_{58}^{3+}$ product count rate in the range 0.03–0.2 Hz. The photon beam energy was stepped 33 times over the range 60–150 eV. The product ions were counted for 20 s at each photon energy point during a sweep. Photon beam was mechanically chopped to subtract background counts yielded by the collisions of the ion

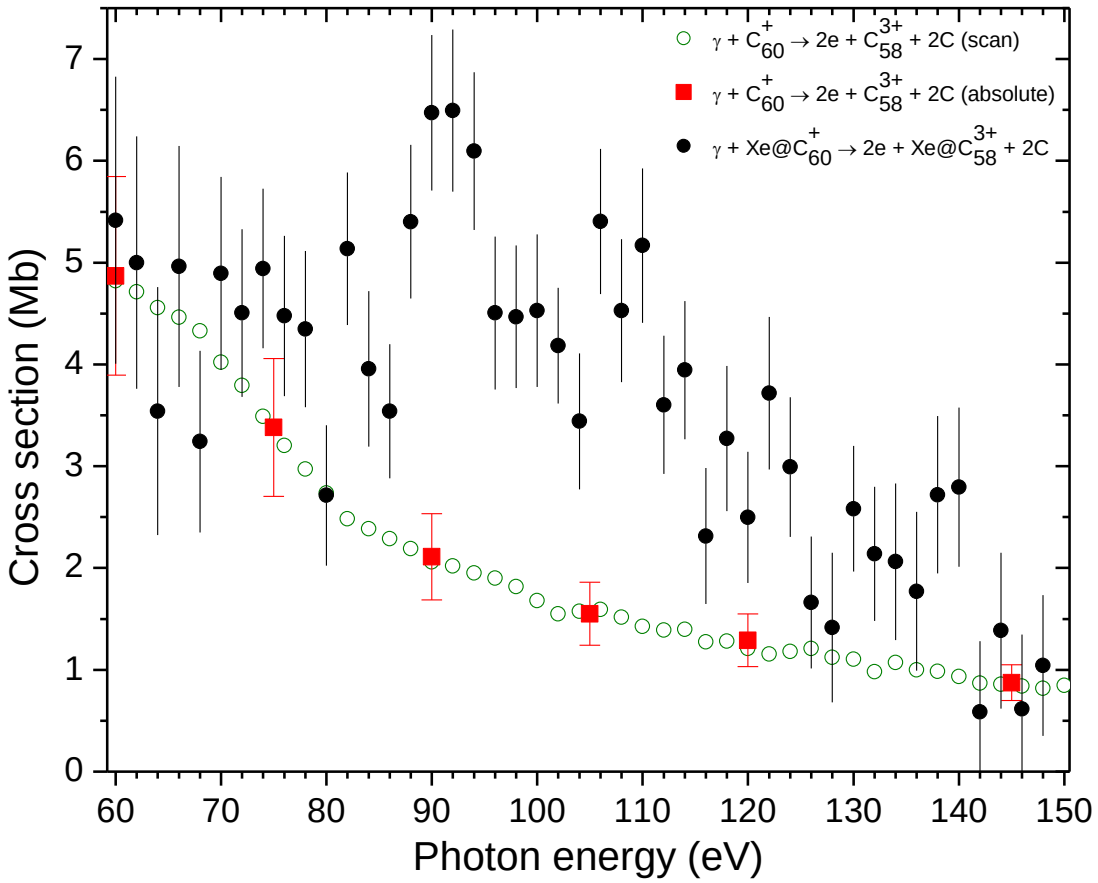

Figure 6.5 Cross section measurements for double photoionization with C_2 fragmentation for C_{60}^+ (open circles and squares) and $Xe@C_{60}^+$ (solid circles). The error bars on the solid circles are statistical (1 standard deviation from the mean), and those on the open squares are the absolute uncertainties [26].

beam with residual gas. Each data point corresponds to approximately 1400 s of total data accumulation at that energy. A photon energy scan was also made under the same conditions but with the ion beam flagged and the results verified the absence of background counts in the product ion detector produced by the photon beam. For

reference, measurements for double photoionization with fragmentation of the empty cage C_{60}^{+} yielding a C_{58}^{3+} product were also performed under similar conditions. At some discrete energies, the absolute cross sections for C_{60}^{+} yielding a C_{58}^{3+} product were measured to which empty C_{60}^{+} and $Xe@C_{60}^{+}$ data were normalized in the energy ranges 60–70 eV and 140–150 eV where no significant contributions from Xe 4d ionization are expected. Normalized cross sections for the endohedral $Xe@C_{60}^{+}$ and the empty C_{60}^{+} cage thus resulted are shown in Figure 6.5. Error bars are statistical, representing one standard deviation from the mean. Significant enhancement of the cross section for the endohedral relative to the empty fullerene in the 70–140 eV range is evident.

The difference between the endohedral $Xe@C_{60}^{+}$ and the empty C_{60}^{+} cage cross section measurements is taken to give the excess cross section due to the presence of Xe inside the C_{60}^{+} cage, which is attributed to the net Xe 4d contributions (Figure 6.6). The theoretical cross section for the photoionization of free Xe atom calculated by Amusia et al. [20] using random phase approximation (RPAE) method have been multiplied by 0.13 and plotted for comparison. The experimental data indicate a strong, statistically significant enhancement of the photoionization cross section in this energy range due to the presence of Xe inside the C_{60}^{+} cage, as well as a structure that is suggestive of confinement resonances. By integrating the area under the cross section curve in the range 70 – 150 eV, oscillator strength was found to be 1.31. Since the Xe 4d oscillator strength is 10, it indicates that the $Xe@C_{58}^{3+}$ product channel accounts for only about 13% of the total Xe 4d oscillator strength.

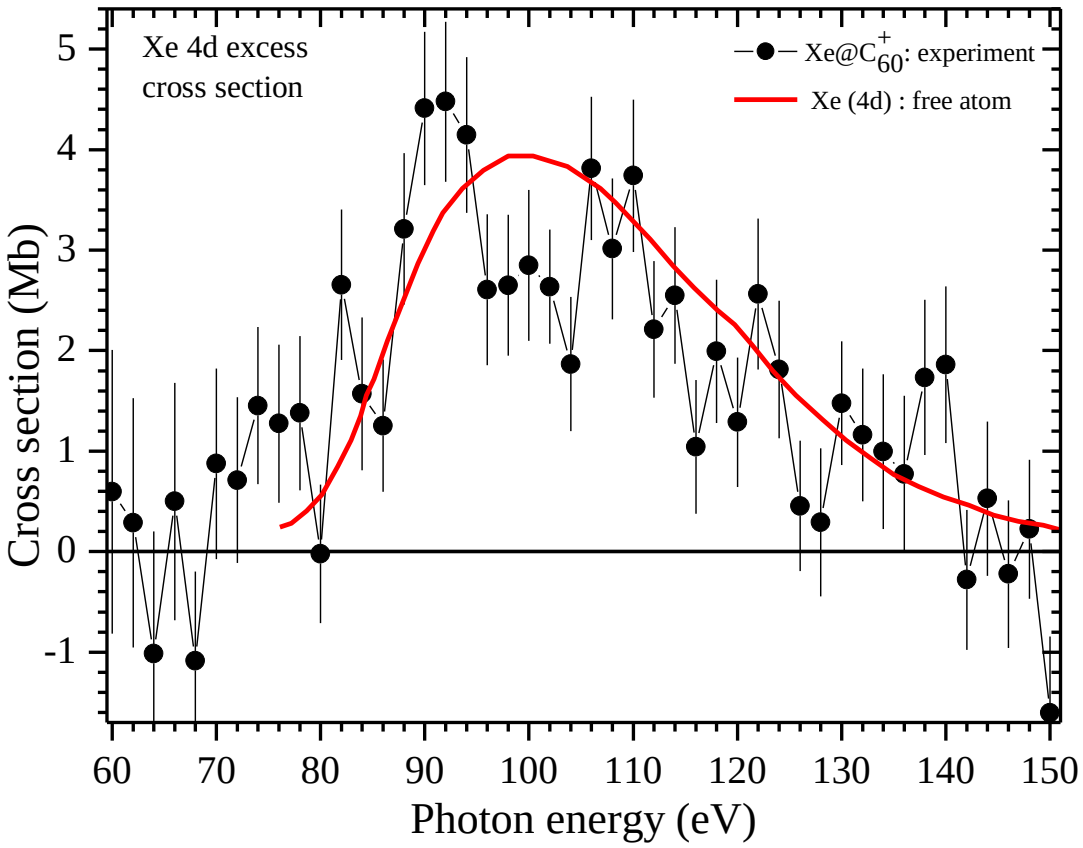

Figure 6.6 Excess cross section for double photoionization accompanied by release of C_2 for $Xe@C_{60}^+$ relative to the same process for empty C_{60}^+ [26]. Error bars are statistical, representing 1 standard deviation from the mean. The solid curve represents the theoretical cross section for 4d photoionization of free Xe [20], multiplied by 0.13 to match the experimental results.

6.4.1.2 Results from Improved Measurements

New measurements were performed for the photoionization of $^{136}Xe@C_{60}^+$ yielding $^{136}Xe@C_{58}^{3+}$ products with significantly increased $^{136}Xe@C_{60}^+$ ion beam current by using the samples containing higher yield of endohedral $^{136}Xe@C_{60}$. Primary ion beam currents in range 0.4 - 2.25 pA were used giving the net product count rates in the range 0.45 – 3.2 Hz. The photon energy was stepped over the range 60 – 150 eV with 0.5 eV

steps and 10 s dwell time. Since the photon beam was not chopped during these energy scans, background counts were measured for 100 s at 90 eV for each measurement and subtracted. To improve the statistics in the range 60 – 80 eV due to lower photon flux in second grating, data were taken using the lower energy grating. All the spectroscopic measurements were combined to create a single photo-spectrum in which each data point in the 60 - 90 eV range corresponds to approximately 1400 s and about 1100 s in the 90 – 150 eV range (Table 6.2) of total data accumulation at that energy. Reference measurements were made for the empty C_{60}^{+} cage yielding C_{58}^{3+} under similar conditions. Relative cross sections for $Xe@C_{60}^{+}$ and C_{60}^{+} were placed on absolute scale and shown in figure 6.7. The solid squares with error bar are the absolute cross sections for double photoionization with fragmentation of C_{60}^{+} yielding C_{58}^{3+} (Table 6.1) with uncertainty taken to be ±23% and open circles are normalized cross sections. Solid circles with error bars represent the normalized cross sections for $Xe@C_{60}^{+}$ with ± 3% statistical uncertainty in the spectroscopic measurements.

Table 6.2 Summary of data collection for double photoionization of $Xe@C_{60}^{+}$ yielding $Xe@C_{58}^{3+}$ products.

Measu-rement	Photon energy range (eV)	Average ion beam current (pA)	No. of sweeps	Dwell time (s)	Count rate (90 eV) (Hz)	Back-ground count rate (Hz)	Net count rate (Hz)
1	60 - 150	2.25	23	10	3.32	0.22	3.10
2	60 - 150	0.436	40	10	0.585	0.06	0.525
3	60 - 150	0.37	40	10	0.52	0.1	0.41
4	50 - 90	0.42	33	10	0.60	0.1	0.50

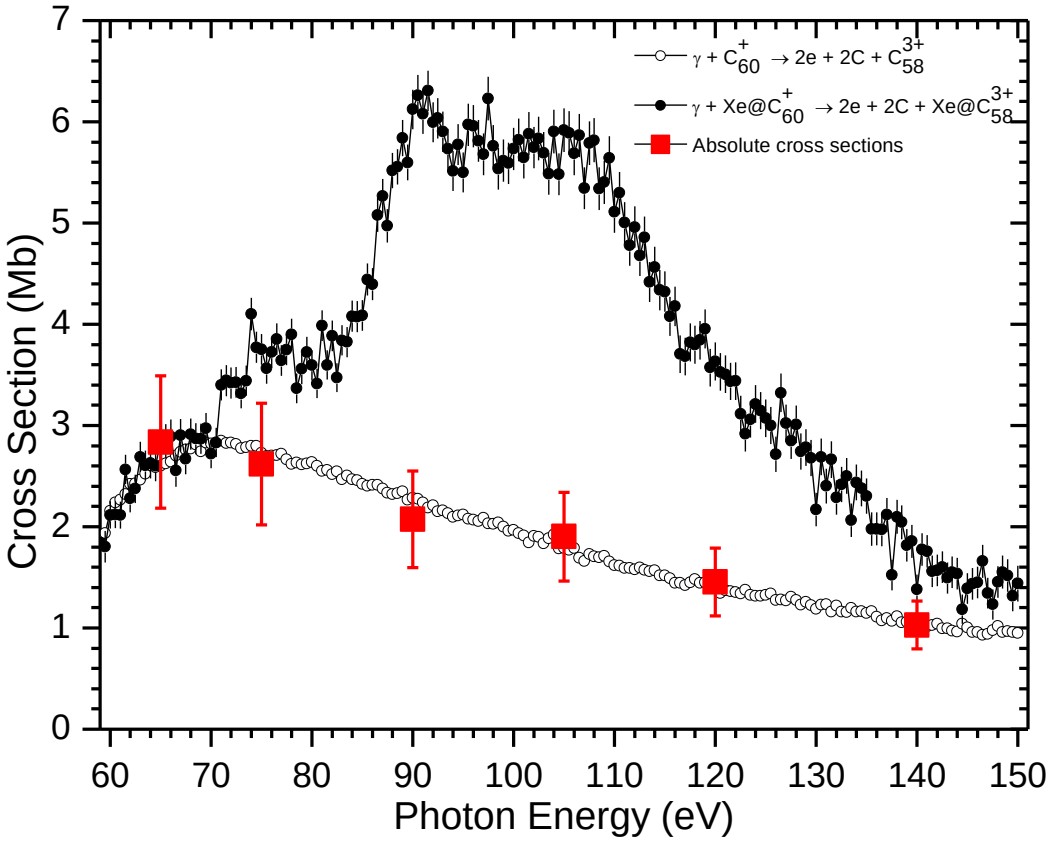

Figure 6.7 Cross section measurements for double photoionization and fragmentation of C_{60}^{+} (open circles and solid squares) and $Xe@C_{60}^{+}$ (solid circles) with a loss of 2 C atoms. The error bars on the solid circles are statistical and those on the solid squares are the absolute uncertainty estimated to be ±23%.

Figure 6.8 shows the excess cross section due to the presence of Xe inside C_{60}^{+} cage. The integral Xe 4d oscillator strength was found to be 1.51 in the 70 – 150 eV range, which indicates that the $Xe@C_{58}^{3+}$ product channel accounts for about 15% of the total Xe 4d oscillator strength. Plotted for comparison are the published experimental results [26] and the cross section for photoionization of free Xe atom calculated using the random phase approximation with exchange (RPAE) method [20] which are multiplied by 0.15 to match the experimental data.

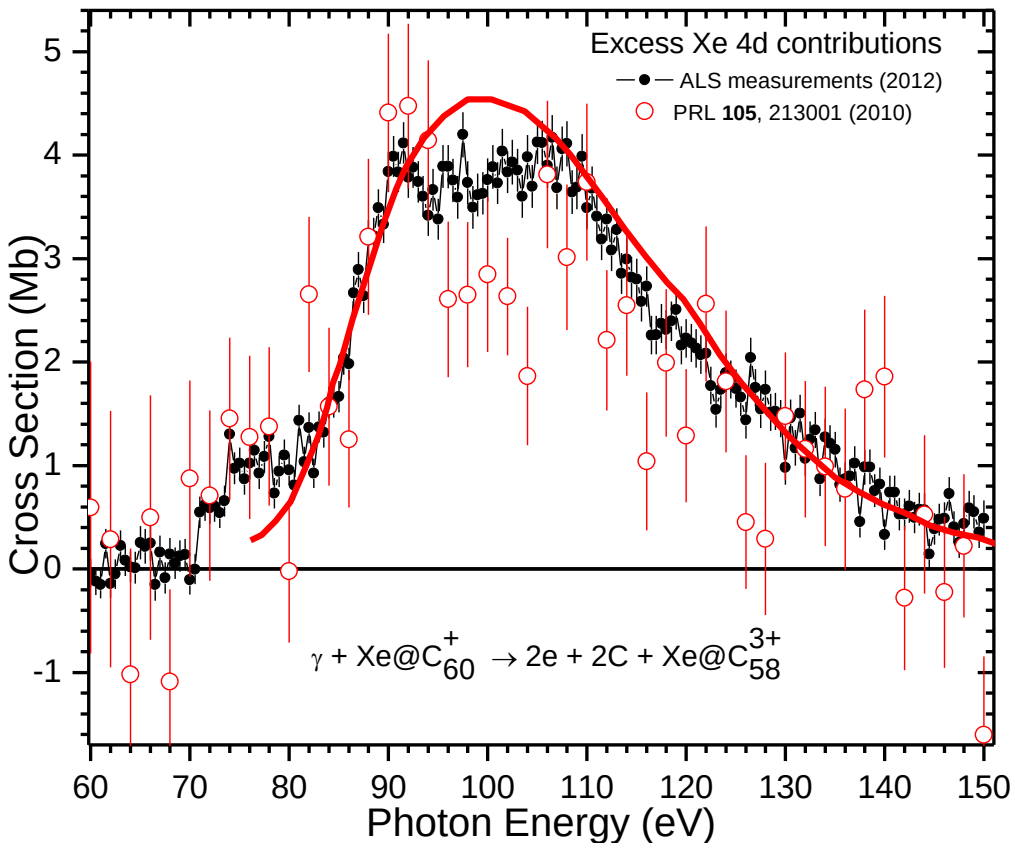

Figure 6.8 Excess cross section for double photoionization accompanied by release of C_2 for $Xe@C_{60}^+$ relative to the same process for empty C_{60}^+. Solid circles are the results from improved measurements and open circles are the published results [26]. Error bars are statistical. Solid curve represents the theoretical results for photoionization of a free Xe atom [20], multiplied by 0.15 to match the experimental results.

A significant improvement in counting statistics and smaller energy steps of 0.5 eV compared to 2 eV together resulted in a much clearer representation of the Xe 4d resonance contribution to the photoionization cross section. Broad peaks centered at about 75 eV, 90 eV, and 108 eV suggested in the published data, are prominent in the improved measurement. This provides much stronger evidence for the existence of confinement resonances in photoionization of $Xe@C_{60}^+$.

6.4.2 Double Photoionization of $Xe@C_{60}^{+}$

Measurements for double photoionization of $Xe@C_{60}^{+}$ yielding $Xe@C_{60}^{3+}$ products were performed with the $Xe@C_{60}^{+}$ ion beam current of range 0.7 – 5.6 pA. A summary of the data collected is given in Table 6.3. Background signals were measured and subtracted from unchopped data. All these data were combined to obtain a photoionization spectrum. For reference, measurements were made for the empty C_{60}^{+} cage yielding C_{60}^{3+} under similar conditions. Photoionization spectra for double ionization of the endohedral $Xe@C_{60}^{+}$ and the empty C_{60}^{+} cage were normalized to the absolute cross sections given in Table 6.1. Plots of these results are shown in Figure 6.9. The solid squares with error bars represent the absolute cross section for double photoionization of C_{60}^{+} (Table 6.1) with absolute uncertainties taken to be ±23%. The solid circles with error bars represent the normalized cross section for double photoionization of $Xe@C_{60}^{+}$ with a statistical uncertainty of ± 5% or less in the spectroscopic measurements, and open circles represent those for C_{60}^{+}.

Table 6.3 Summary of data collection for double photoionization of $Xe@C_{60}^{+}$ yielding $Xe@C_{60}^{3+}$ product.

Measu-rement	Photon energy range (eV)	Average ion beam current (pA)	No. of sweeps	Dwell time (s)	Count rate (90 eV) (Hz)	Back-ground count rate (Hz)	Net count rate (Hz)
1	60 - 150	1.9	21	10	2.51	0.32	2.19
2	60 - 150	2.52	15	5	2.15	chopped	2.15
3	60 - 150	0.73	11	10	1.95	0.15	1.8
4	60 - 150	5.2	9	10	4.88	0.5	4.38
5	60 - 90	1.52	8	10	2.11	0.2	1.91

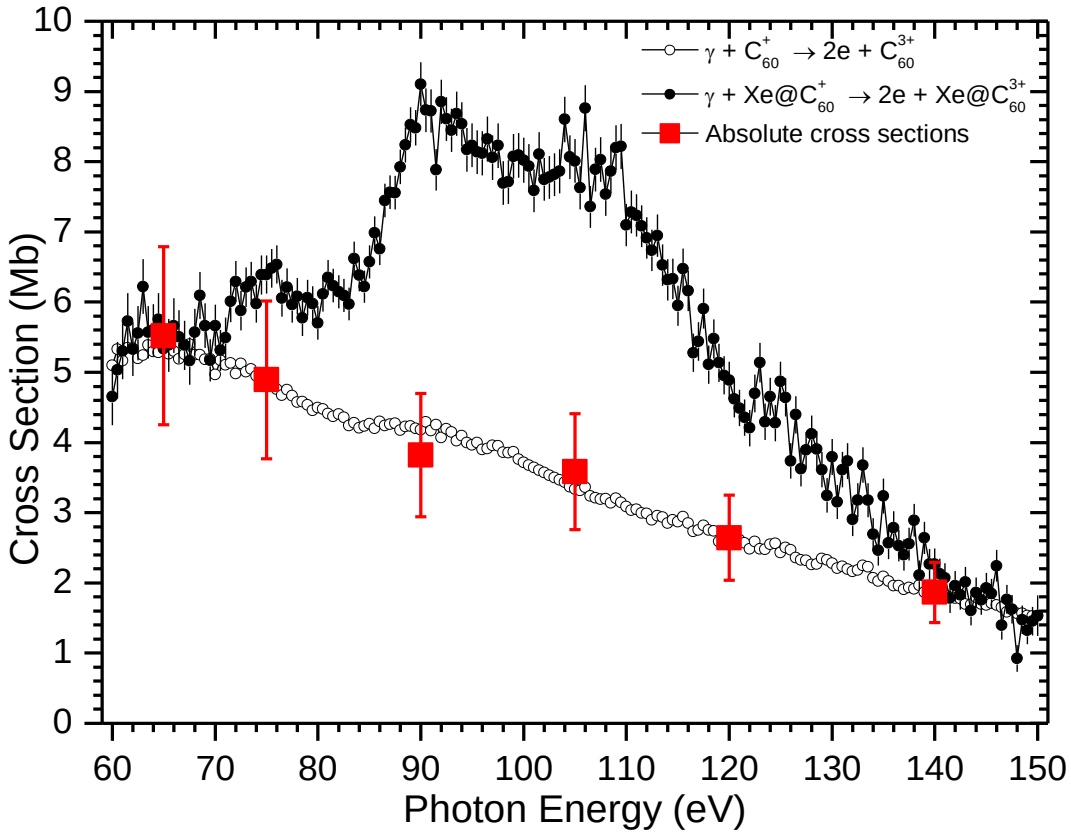

Figure 6.9 Cross section measurements for double photoionization of $Xe@C_{60}^{+}$ and C_{60}^{+}. The error bars on the solid circles are statistical and those on the solid squares are the absolute uncertainties estimated to be ±23%.

Figure 6.10 presents the difference between the cross section measurements for endohedral and the empty molecular ions, which gives the excess cross section due to the presence of Xe inside the C_{60}^{+} cage. Plotted for comparison are the theoretical cross sections for free Xe atom using the RPAE method [20], multiplied by 0.17 to match experimental results. Strong enhancement of the photoionization cross section is evident due to the presence of Xe inside the C_{60}^{+} cage, with photon energy dependent structures.

Since the integral oscillator strength was found to be 1.71 in the 70 – 150 eV energy range, the $Xe@C_{60}^{3+}$ product channel accounts for about 17% of the total Xe 4d oscillator strength.

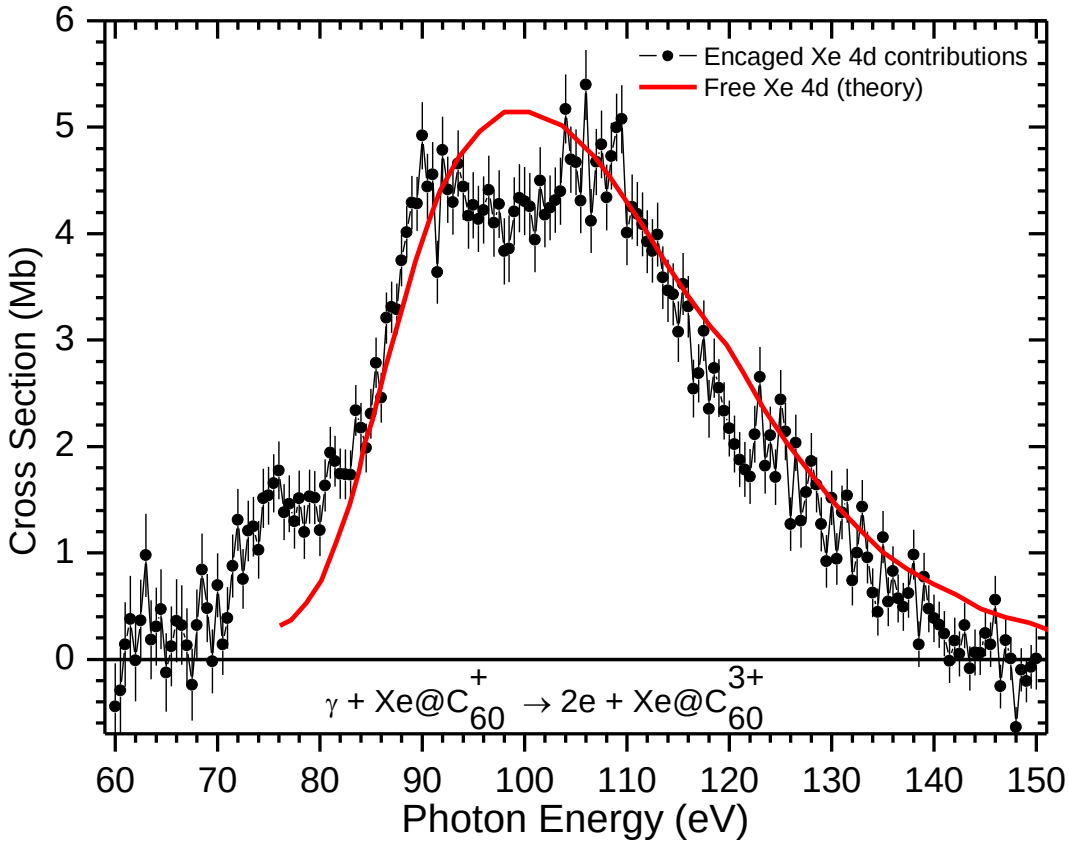

Figure 6.10 Excess cross section for double photoionization of $Xe@C_{60}^{+}$ relative to the same process for empty C_{60}^{+}. Plotted for comparison is theoretical cross sections for 4d photoionization of free Xe (solid curve) [20] . Error bars represent statistical uncertainties in spectroscopic measurements. The $Xe@C_{60}^{3+}$ product channel accounts for about 17% of the Xe 4d oscillator strength.

6.4.3 Double Photoionization and Fragmentation of $Xe@C_{60}^{+}$ with a Loss of Two Pairs of Carbon Atoms

Details of the measurements for double photoionization with fragmentation of $Xe@C_{60}^{+}$ yielding $Xe@C_{56}^{3+}$ products are given in Table 6.4. $Xe@C_{60}^{+}$ ion beam currents in the range 0.85 – 5.7 pA were used and the net product-ion count rate was in the range 1.3 – 7.6 Hz. Since data were taken without chopping the photon beam, measured background signals for each measurement were subtracted from the corresponding data. A single spectrum was obtained by combining all these data from different measurements. For normalization, reference measurements were made for the empty C_{60}^{+} cage yielding C_{56}^{3+} under similar conditions. The spectroscopic measurement of $Xe@C_{60}^{+}$ and the empty C_{60}^{+} cage were normalized to the measured absolute cross sections of C_{60}^{+} yielding a C_{56}^{3+} product (Table 6.1), in the energy ranges 60–70 eV and

Table 6.4 Summary of data collection for double photoionization with fragmentation of $Xe@C_{60}^{+}$ yielding $Xe@C_{56}^{3+}$ product.

Measu-rement	Photon energy range (eV)	Average ion beam current (pA)	No. of sweeps	Dwell time (s)	Count rate (90 eV) (Hz)	Back-ground count rate (Hz)	Net count rate (Hz)
1	60 - 150	1.23	32	10	1.90	0.28	1.62
2	60 - 115	3.7	15	10	5.70	0.82	4.88
3	110 - 150	5.5	3	10	7.2 (112 eV)	1.1	6.1
4	65 - 85	1.2	15	10	1.15 (85 eV)	0.2	0.95
5	85 - 112	2.07	15	10	3.61	0.46	3.15
6	60 - 150	0.85	9	10	1.03	0.1	0.93

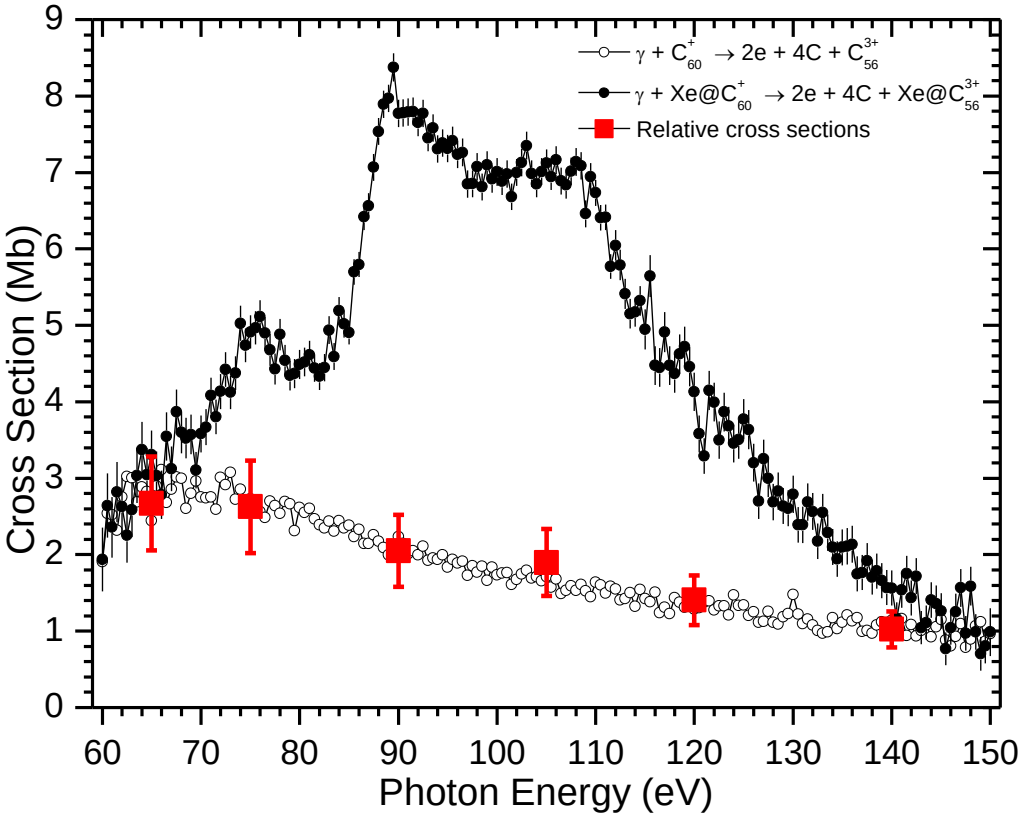

Figure 6.11 Cross section measurements for double photoionization and fragmentation of C_{60}^{+} and $Xe@C_{60}^{+}$ with a loss of two pairs of carbon atoms. Solid circles with error bars are the normalized cross section of $Xe@C_{60}^{+}$ with statistical uncertainties, open circles are normalized cross section of C_{60}^{+}, and solid squares with error bars are the absolute measurements for C_{60}^{+} with ±23% absolute uncertainties.

140–150 eV. The results are shown in Figure 6.11. The error bars on the solid squares represent the uncertainty for the absolute cross section measurements estimated to be ±23% and those in the solid circles are statistical uncertainty of ± 5% or less in the spectroscopic measurements.

The difference between the cross sections measured for $Xe@C_{56}^{3+}$ and C_{56}^{3+} products is plotted as a function of photon energy and shown in Figure 6.12. The RPAE

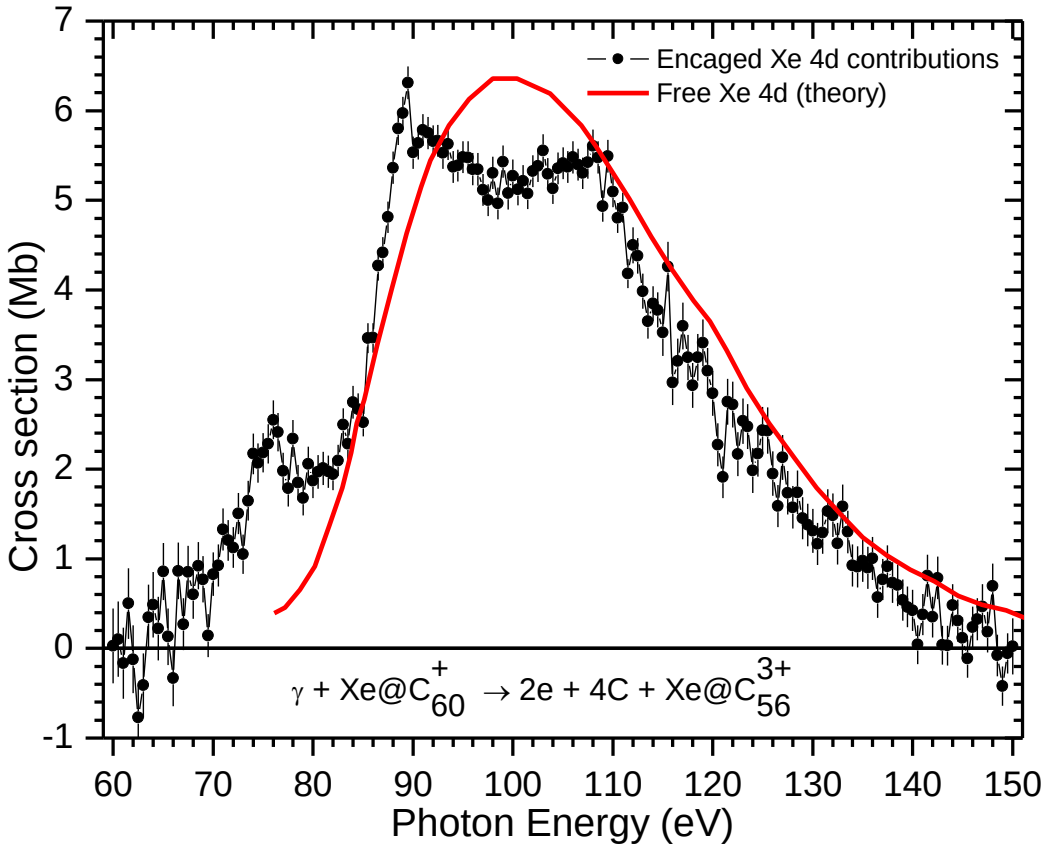

Figure 6.12 Excess cross section for double photoionization with fragmentation of $Xe@C_{60}^{+}$ with a loss of two pairs of carbon atoms relative to the same process for empty C_{60}^{+}. Plotted for comparison are theoretical cross sections for 4d photoionization of free Xe (solid curve) [20]. The $Xe@C_{56}^{3+}$ product channel accounts for about 21% of the Xe 4d oscillator strength.

calculation for the photoionization cross section of a free Xe atom [20] are scaled and plotted for comparison. The experimental data indicate a strong, statistically significant enhancement of the photoionization cross section in this energy range due to the presence of Xe inside the C_{60}^{+} cage, again showing structure that is suggestive of confinement resonances. By integrating the area under the cross section curve in the range 70 – 150 eV, the oscillator strength was 2.11, indicating that the $Xe@C_{56}^{3+}$ product channel accounts for about 21% of the Xe 4d oscillator strength.

6.4.4 Double Photoionization and Fragmentation of $Xe@C_{60}^{+}$ with a Loss of Three Pairs of Carbon Atoms

Similar measurements were performed for double photoionization with fragmentation of $Xe@C_{60}^{+}$ yielding $Xe@C_{54}^{3+}$ products. $Xe@C_{60}^{+}$ ion beam current of about 2.5 pA was used and the maximum net product count rate was observed about 0.8 Hz. Without chopping the photon beam, the product photo-ions were scanned 28 times over the range 60 – 150 eV with 0.5 eV steps and 10 s dwell time. So, the total counting time per point was 280 s. Background signals were measured during measurements and

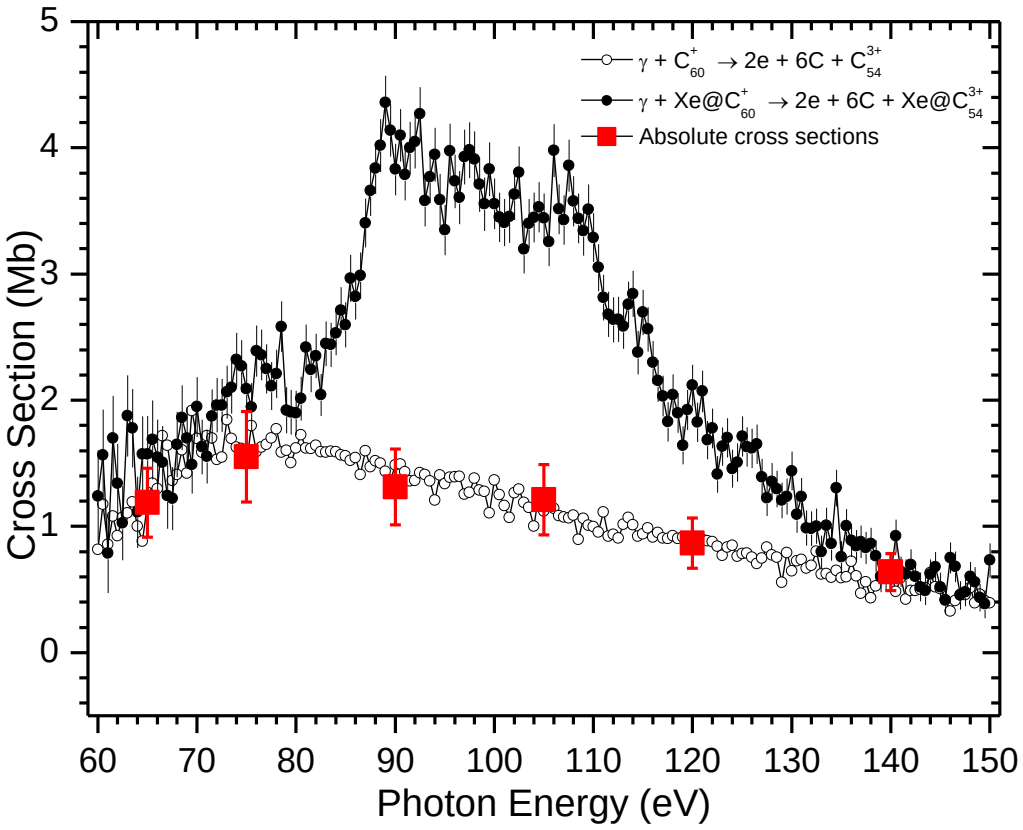

Figure 6.13 Cross section measurements for double photoionization and fragmentation of C_{60}^{+} and $Xe@C_{60}^{+}$ with a loss of three pairs of carbon atoms. The error bars on open circles are statistical and those on solid squares are absolute uncertainties.

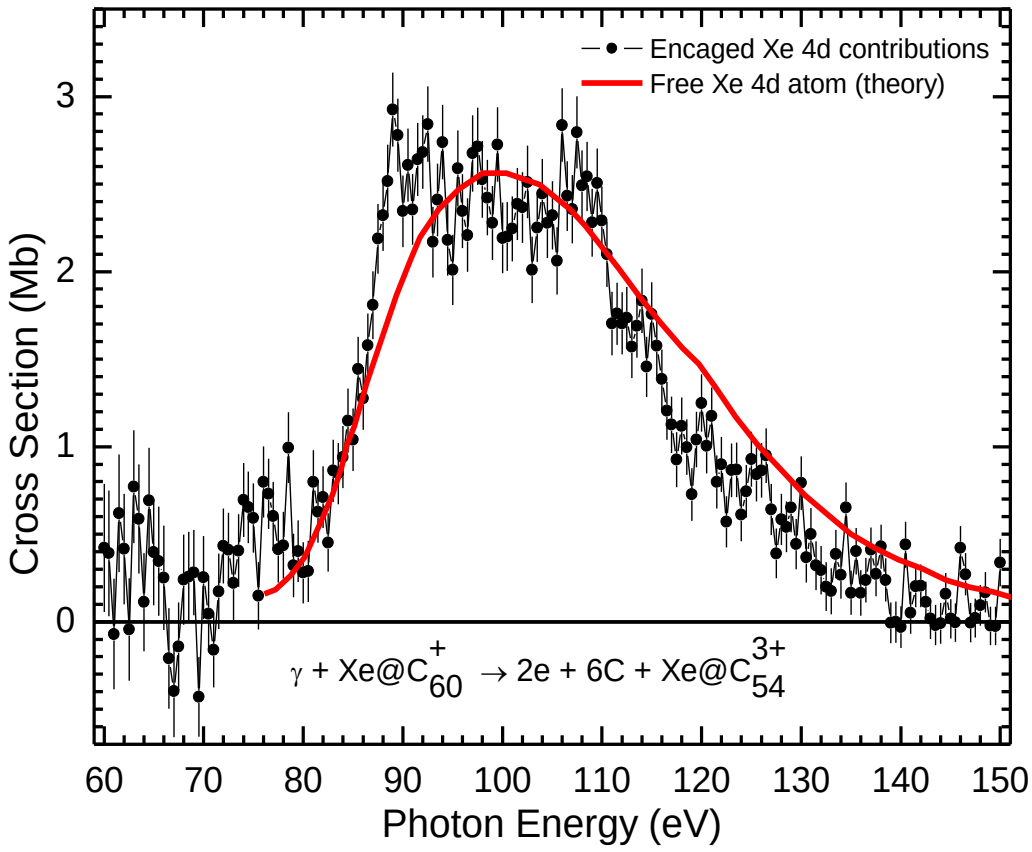

Figure 6.14 Excess cross section for double photoionization with fragmentation of $Xe@C_{60}^{+}$ relative to the same process for empty C_{60}^{+}. Error bars are statistical. Plotted for comparison are theoretical cross sections for 4d photoionization of free Xe (solid curve) [20]. The $Xe@C_{54}^{3+}$ product channel accounts for about 8.5% of the Xe 4d oscillator strength.

subtracted from the corresponding data. For reference, measurements were made for the empty C_{60}^{+} cage yielding C_{54}^{3+} under identical conditions. The endohedral $Xe@C_{60}^{+}$ data was normalized to the empty C_{60}^{+} data using absolute cross sections of C_{60}^{+} yielding a C_{54}^{3+} product given in Table 6.1 and the results are shown in Figure 6.13. In the graph, the vertical error bars on the solid squares represent the absolute uncertainties for the

cross section measurements estimated to be ±23% and those in the solid circles are the statistical uncertainty in the spectroscopic measurements.

Figure 6.14 presents the excess cross section of the endohedral $Xe@C_{60}^{+}$ relative to the empty C_{60}^{+} cage, giving net Xe 4d contributions. Results show a statistically significant enhancement of the photoionization cross section in this energy range due to the presence of Xe inside the C_{60}^{+} cage. For this product channel, confinement resonances associated with Xe 4d photoabsorption are evident. The integral oscillator strength in the energy range 70 -150 eV was found to be 0.85. Since the Xe 4d oscillator strength is 10, the $Xe@C_{54}^{3+}$ product channel accounts for about 8.5% of the Xe 4d oscillator strength.

6.5 Result and Discussion

Results from the measurements with empty C_{60}^{+} ions in 60 – 150 eV photon energy range showed that double photoionization of C_{60}^{+} accompanied by loss of one or more pairs of carbon atoms is significant. Cross section measurements for single and double photoionization with fragmentation of $Xe@C_{60}^{+}$ were performed in 60 – 150 eV photon energy range. Although double photoionization of a free Xe atom is the dominant product channel, a small Xe 4d contribution could be expected due to single photoionization of the Xe atom inside the C_{60}^{+} cage. However, the results from single photoionization of $Xe@C_{60}^{+}$ showed almost no signature of Xe 4d contribution, which might be due to additional processes such as electron capture and electron-impact ionization that took place as a result of interaction of photoelectron from Xe 4d shell with the C_{60}^{+} cage.

Results from double photoionization with fragmentation of $Xe@C_{60}^{+}$ yielding $Xe@C_{60-2n}^{3+}$ (n = 0, 1, 2, and 3) products showed strong Xe 4d contributions, as expected. The individual Xe 4d contributions for the different products are plotted on the same cross section scale and are compared in Figure 6.15. The Xe 4d contributions in each product channel have almost the same photon energy dependence. At least three broad peaks centered at about 76 eV, 90 eV and 108 eV are evident on the net Xe 4d cross section spectra for each product channel, providing stronger evidence for the existence of confinement resonances in the photoionization of $Xe@C_{60}^{+}$. The strongest Xe 4d photoionization signature among these four product channels appears in the $Xe@C_{56}^{3+}$ product channel. It suggests that the geometrical structure of a C_{56} cage is more favorable for caged Xe after double photoionization than for C_{60}, C_{58} and C_{54} cages. The Xe 4d oscillator strengths for each product channel obtained by integrating the cross section curves in the range 70 – 150 eV are presented on Table 6.5. These products account for 6.18 of the total Xe 4d oscillator strength of 10.

Table 6.5 Integral oscillator strengths for the four product channels

Product channels	**Area under the curve (Mb.eV)** (70-150 eV)	**Oscillator strength** (Area x 9.11 x 10^{-3})
$Xe@C_{60}^{3+}$	187.38	1.71
$Xe@C_{58}^{3+}$	165.98	1.51
$Xe@C_{56}^{3+}$	231.14	2.11
$Xe@C_{54}^{3+}$	93.04	0.85
Sum	**677.54**	**6.18**

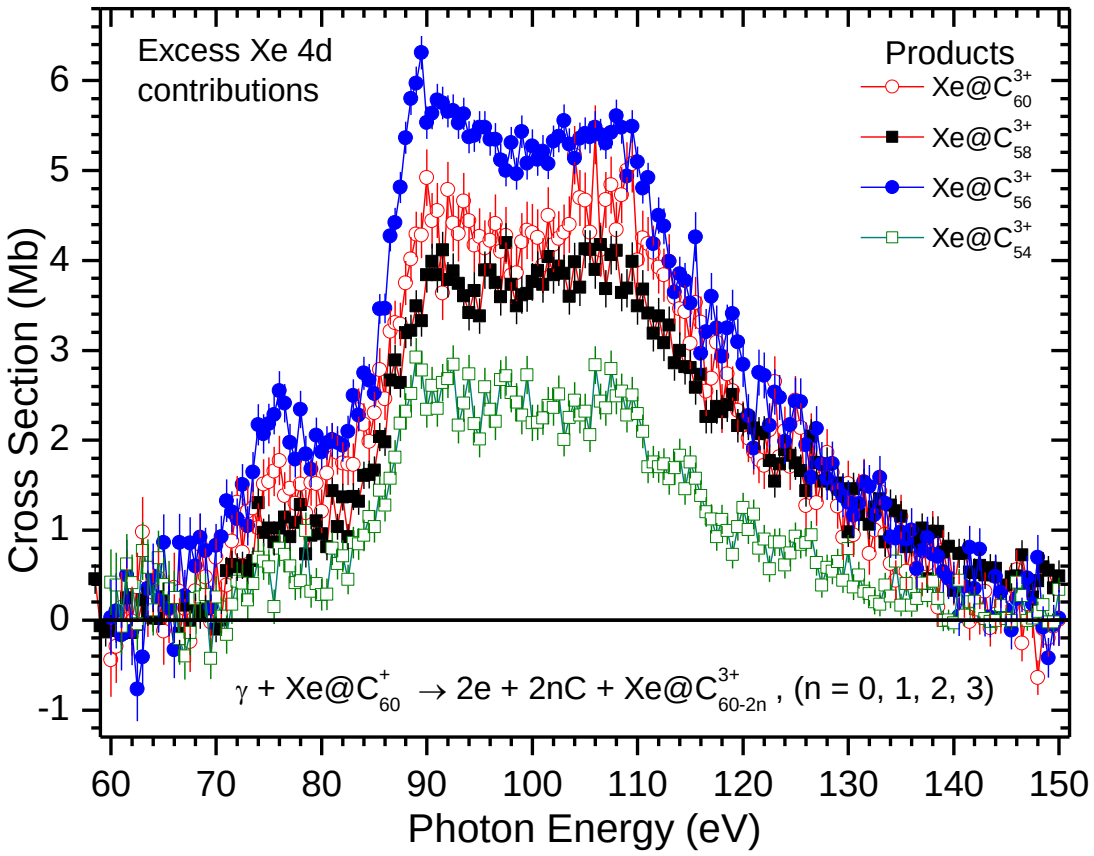

Figure 6.15 Net Xe 4d contributions to the double photoionization of $^{136}Xe@C_{60}^{+}$ accompanied by the loss of 0, 2, 4 and 6 C atoms on the same cross section scale.

Figure 6.16 compares the sum of the net Xe 4d contributions for measured product channels with the theoretical calculation of single photoionization cross section of free xenon atom. Theoretical values of the cross section are multiplied by 0.62 to match the experimental results. Confinement resonances are evident, resulting from multi-path interference of photoelectron waves emitted by the encaged Xe atom that may be transmitted or reflected by the C_{60}^{+} cage. Above 115 eV, the spectrum follows the Xe atom 4d curves almost perfectly. This indicates that C_{60}^{+} cage becomes transparent to the photoelectron in the higher photon energy range and thus the interference is absent.

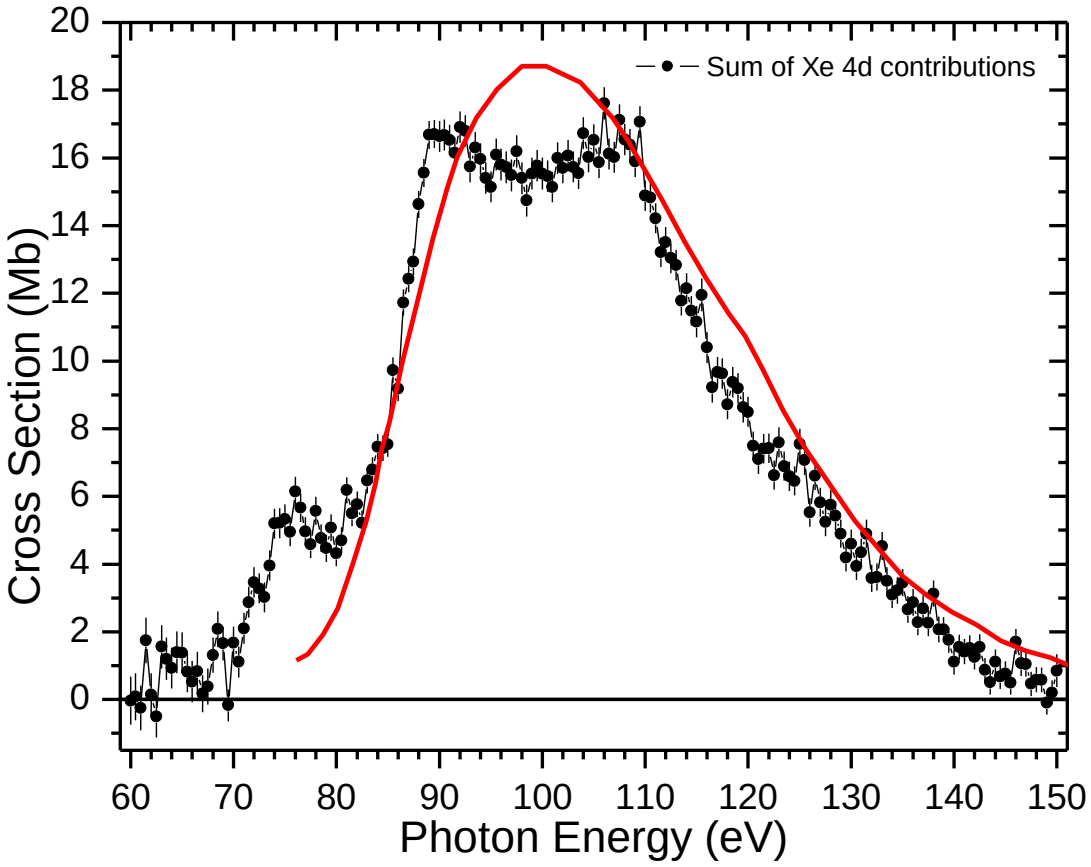

Figure 6.16 Sum of the net Xe 4d contributions for the $Xe@C_{60-2n}^{3+}$ (n = 0, 1, 2, and 3) product channels. Theoretical cross sections for single photoionization of a free Xe atom [20] are multiplied by 0.62 to compare the experimental results.

These four products account for 6.18 out of total Xe 4d oscillator strength of 10, indicating that the Xe 4d oscillator strength is distributed predominantly into double photoionization with fragmentation product channels, and the remaining oscillator strength is likely distributed into other photoionization product channels such as triple photoionization and fragmentation product channels. The results are compared with various theoretical predictions for photoabsorption by $Xe@C_{60}$ and discussed in further detail in the next chapter.

Chapter 7

Triple Photoionization with Fragmentation of $Xe@C_{60}^{+}$ with a Loss of One Pair of Carbon Atoms

Cross section for triple photoionization with fragmentation of $Xe@C_{60}^{+}$ yielding $Xe@C_{58}^{4+}$ products were performed in 60 – 150 eV photon energy range. Results from these measurements are compared, and combined with the results from the cross section measurements for double photoionization with fragmentation products to obtain total Xe 4d contributions. The combined Xe 4d contributions for measured products due to photoionization of $Xe@C_{60}^{+}$ are compared with the theoretically calculated results based on various approximation methods with prediction of "confinement resonances", and are discussed in this chapter.

7.1 Introduction

The cross section measurements for double photoionization with fragmentation product channels together account for about 62% of the total Xe 4d oscillator strength indicating that some might be apparent in higher ionization product channels. In this photon energy region, 4d photoionization of atomic Xe leads to single ionization, dominant double ionization and a third of the cross section for double ionization is found in triple ionization [106]. This motivated a search for the remaining oscillator strength in the triple ionization of $Xe@C_{60}^{+}$. Measurements were made for the triple ionization with fragmentation yielding $Xe@C_{58}^{4+}$, represented as:

$$\gamma + Xe@C_{60}^{+} = 3e + 2C + Xe@C_{58}^{4+} \qquad (7.1)$$

7.2 Cross Section Measurements for Triple Photoionization with Fragmentation of $Xe@C_{60}^{+}$ Yielding $Xe@C_{58}^{4+}$

Measurements for the $Xe@C_{58}^{4+}$ product channel were performed with a $Xe@C_{60}^{+}$ ion beam current of about 2.5 pA. Without chopping the photon beam, $Xe@C_{58}^{4+}$ products were scanned over 60 – 150 eV photon energy range in 0.5 eV increments and with 10 s dwell time. Background counts were measured during the measurement and subtracted. For reference, same measurements were made for the empty C_{60}^{+} cage yielding C_{58}^{4+} under similar conditions. The measured data for endohedral $Xe@C_{60}^{+}$ were normalized to that for empty C_{60}^{+} cage using absolute cross sections for C_{60}^{+} yielding a C_{58}^{4+} product (Table 7.1) and are shown in Figure 7.1. Error bars in the solid circles are statistical uncertainties in the spectroscopic measurements and those on open squares are absolute uncertainties estimated to be ±23%.

Table 7.1 Cross sections for triple photoionization with fragmentation of C_{60}^{+} yielding C_{58}^{4+}.

Photon Energy (eV)	Absolute cross sections for C_{58}^{4+} product (Mb)
90	2.08
105	1.90
140	1.03

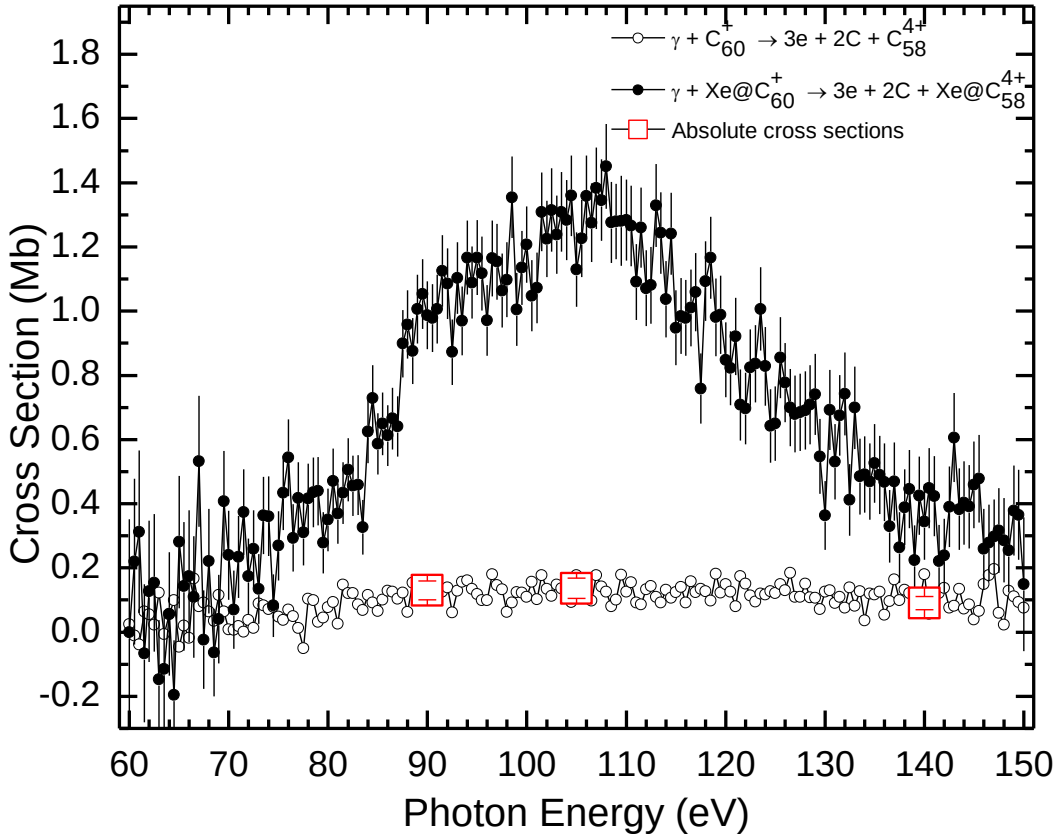

Figure 7.1 Cross section measurements for triple photoionization and fragmentation of C_{60}^{+} and $Xe@C_{60}^{+}$ with a loss of one pair of carbon atoms. The error bars on solid circles are statistical and those on open squares are the absolute uncertainties.

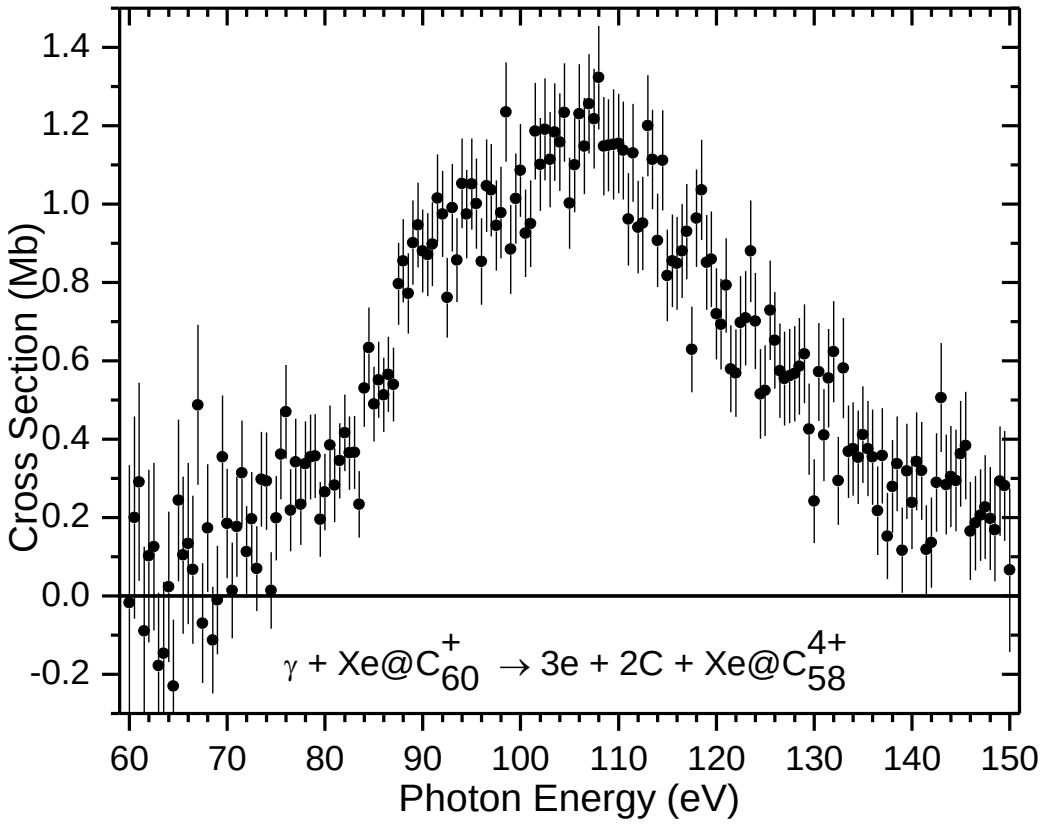

Figure 7.2 Excess cross section for triple photoionization with fragmentation of $Xe@C_{60}^{+}$ yielding $Xe@C_{58}^{4+}$ products relative to the same process for empty C_{60}^{+}. The $Xe@C_{58}^{4+}$ product channel accounts for about 5% of the total Xe 4d oscillator strength.

Figure 7.2 presents the difference between the cross section measurements for endohedral $Xe@C_{60}^{+}$ and the empty C_{60}^{+} molecular ions, which is attributed to the excess cross section due to the presence of Xe inside the C_{60}^{+} cage. The experimental data indicate a statistically significant enhancement of the photoionization cross section in this energy range due to the presence of Xe inside the C_{60}^{+} cage. By integrating the area under the cross section curve in the range 70 – 150 eV, the oscillator strength was found to be 0.47. Since the Xe 4d oscillator strength is 10, it indicates that the $Xe@C_{58}^{4+}$ product channel accounts for about 5% of the Xe 4d oscillator strength.

7.3 Result and Discussion

The net Xe 4d contribution for the $Xe@C_{58}^{4+}$ product channel is compared in Figure 7.3 with the sum of Xe 4d contributions for $Xe@C_{60-2n}^{3+}$ products from double photoionization with fragmentation of $Xe@C_{60}^{+}$. For comparison, the results of triple photoionization are multiplied by 13. The plotted curve represents the theoretical calculation of the free Xe 4d cross section [20] scaled to match the experimental results.

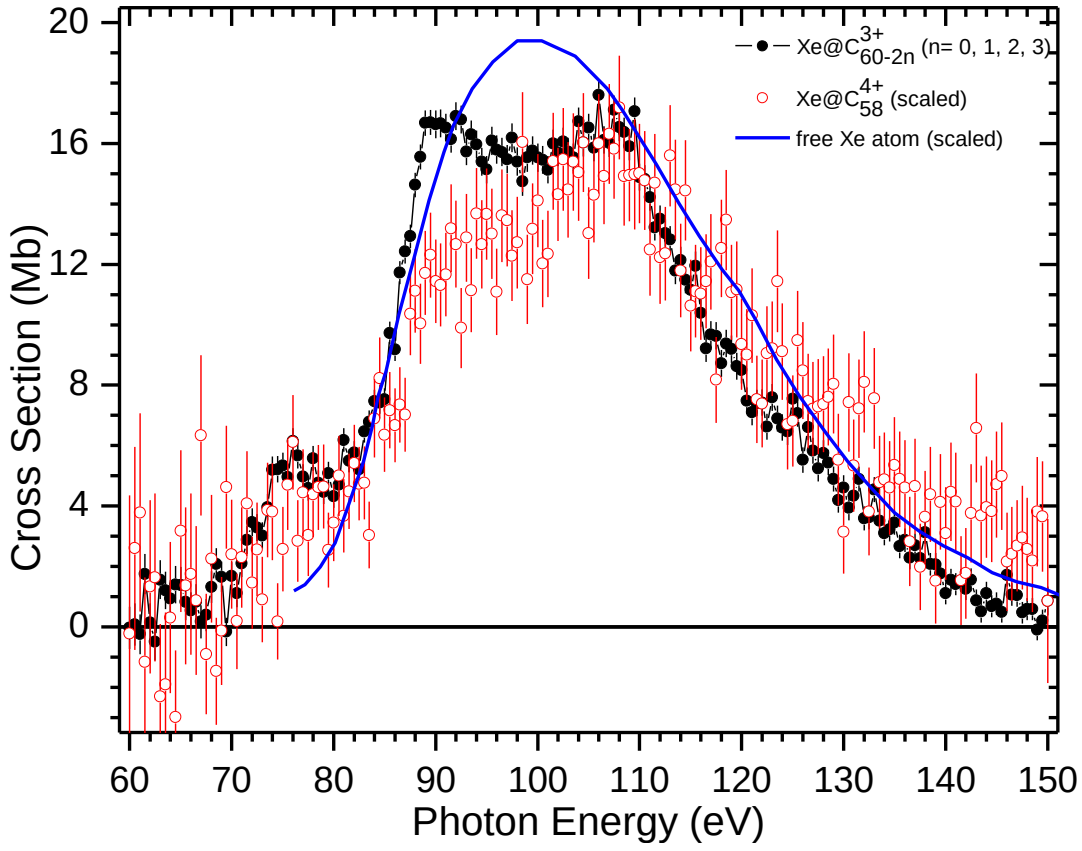

Figure 7.3 Comparison of the Xe 4d cross section for triple photoionization with fragmentation of $Xe@C_{60}^{+}$ yielding $Xe@C_{58}^{4+}$ products (open circles) to the sum of the Xe 4d cross sections from double ionization with fragmentation products (solid circles).

The photon energy dependence of Xe 4d cross section for the triple ionization channel differs from that for the double ionization channels, particularly in the energy range below 105 eV. The peaks around 76 eV and 90 eV are weak. So, this product channel contributing to the total oscillator strength with slightly different energy-dependence indicates different physics.

The ionization potential of Xe 4d is higher than that for direct triple photoionization of the Xe atom. The cross section below 70 eV is close to zero, indicating that the observed net contribution is associated with Xe 4d photoabsorption and the triply charged ions might be produced by different excitation and decay processes. At photon energies higher than the Xe 4d threshold, triply charged ions are likely to be produced by two processes: a double Auger process after photoemission of the 4d electron, and a single Auger transition after a 4d photoionization shake-off process [107,108]. The photoemission of the 4d electron followed by an Auger process that releases two electrons per event is less likely.

Figure 7.4 presents the ratio of Xe 4d cross sections for photoionization and fragmentation of $Xe@C_{60}^{+}$ yielding $Xe@C_{58}^{4+}$ and $Xe@C_{58}^{3+}$ products. Despite statistical fluctuations, a signature of an increased ratio above 92 eV is suggested, which is near the energy required to open the Xe 4d5p double photoionization channel [20]. So, a Xe 4d shake-off process might explain the nature of confinement resonances observed in net triple ionization of $Xe@C_{60}^{+}$. In the shake-off process, the suddenly changed potential of the ionic core due to the Xe 4d subshell ionization results in release of a second photoelectron from an outer shell. Subsequent Auger decay due to filling of the 4d subshell vacancy results in net triple ionization. In this case the two photoelectrons must

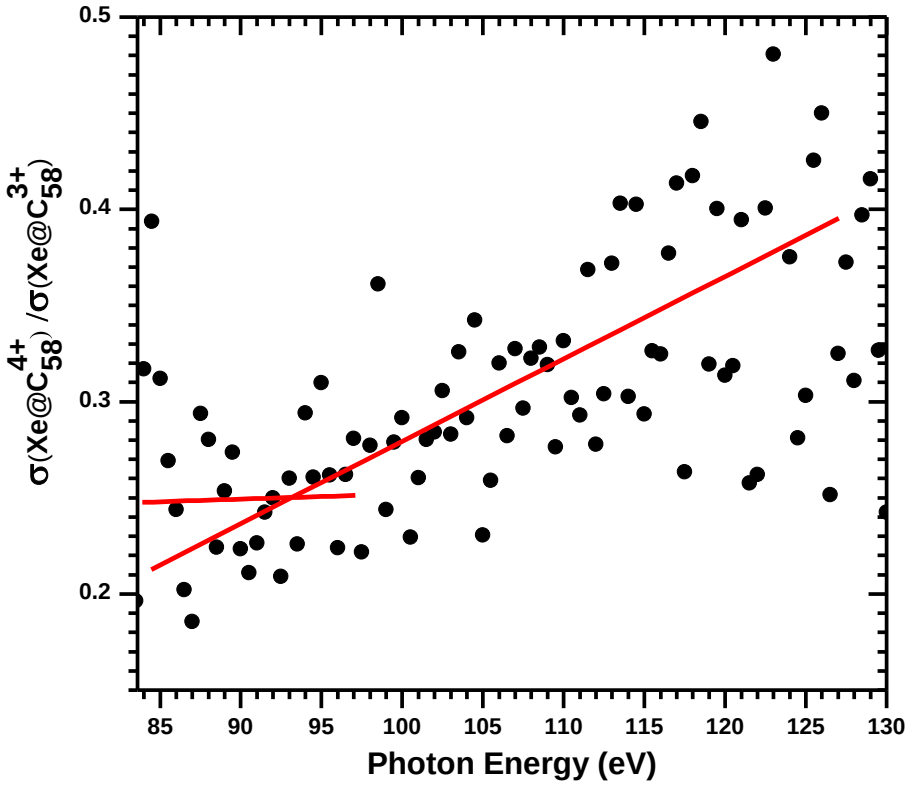

Figure 7.4 Ratio of Xe 4d cross sections for the net triple ionization with fragmentation of $Xe@C_{60}^{+}$ yielding $Xe@C_{58}^{4+}$ to that for the net double ionization with fragmentation of $Xe@C_{60}^{+}$ yielding $Xe@C_{58}^{3+}$ product. An increased ratio above 93 eV suggests the possible role of a Xe 4d photoionization shake-off process followed by a single Auger transition leading to net triple ionization.

share the excess energy, making the interference pattern more complicated. For equal energy sharing, interference between the direct and reflected waves of the two photoelectrons would result in a pattern different than that observed in the product channels resulting in net double ionization because of the changed correspondence between photon and photoelectron energies. In the case of unequal energy sharing, when the faster photoelectron carries away most of the excess energy, the interference pattern would be expected to resemble that observed in the product channels yielding net double

ionization, but with reduced amplitude due to the distribution of photoelectron energies. A theoretical interpretation of this process would be challenging but necessary to better understand the dynamics associated with the triple ionization product channels.

7.4 Comparison with Theoretical Results

The sum of Xe 4d cross sections obtained from the measurements for double and triple photoionization with fragmentation of $Xe@C_{60}^{+}$ are compared with a number of theoretical calculations. The theoretical calculations for photoionization cross section of $Xe@C_{60}$ are mainly based on three approaches: time dependent density functional theory (TDDFT), random phase approximation with exchange (RPAE) and R-matrix methods. For comparison, all theoretical results are scaled by a factor of 2/3 to match the present experimental results giving an integral Xe 4d oscillator strength of 6.65 ± 1.5.

7.4.1 Comparison to RPAE Calculations

Figure 7.5 presents the comparison of experimental results (solid circles) with two theoretical results based on the RPAE method [13, 14]. Solid curve presents the cross section calculated by Amusia et al. [13] for which the potential of the C_{60} shell was represented by a zero-thickness delta-type spherical attractive potential. On the basis of this model, strong oscillations in the energy dependence of the photoionization cross section are predicted, producing four maxima in the Xe 4d photoionization of $Xe@C_{60}$. Only for comparison, their results are shifted in energy by - 4.5 eV. The energy dependences of resonances and their amplitudes do not agree with the experimental results, except for the positions of two peaks at about 90 eV and 108 eV. The RPAE results of Dolmatov et al. [14] are shifted down in energy by 4.5 eV and represented by dashed curve. Their calculations are based on modeling the confining cage C_{60} by a

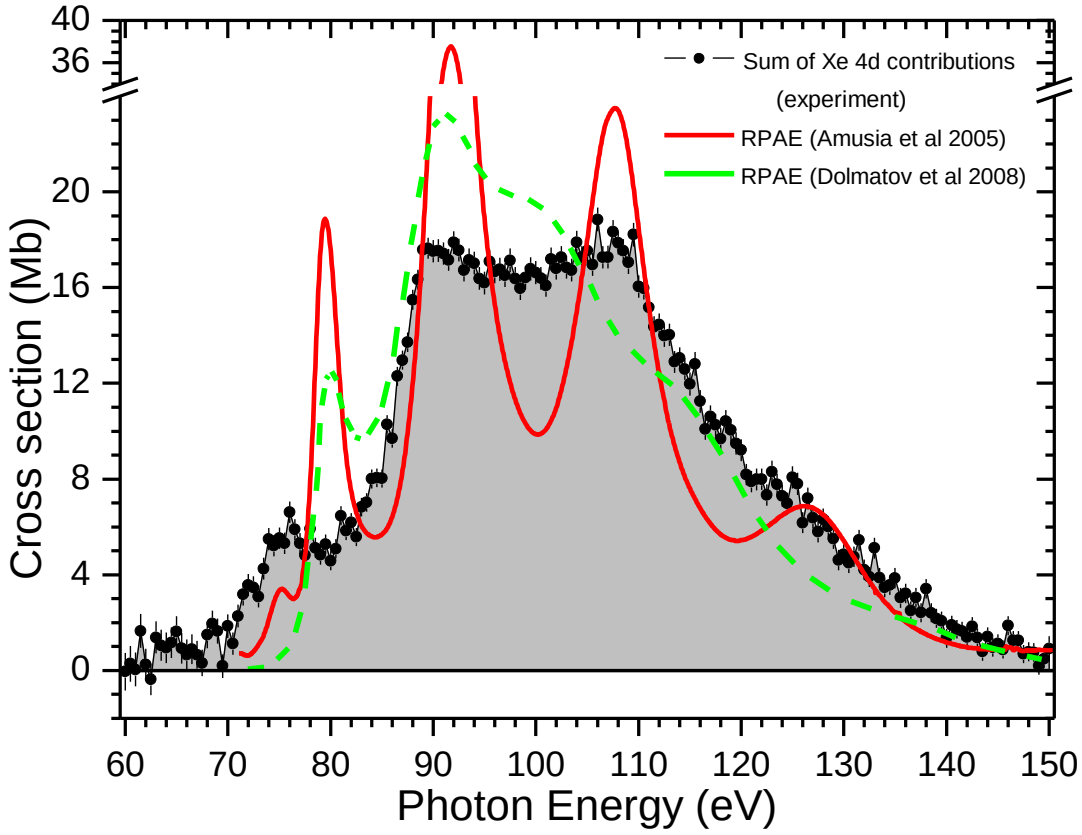

Figure 7.5 Comparison of experimental results (solid circles) with results from the RPAE calculations by Amusia et al. (solid curve) [13] and Dolmatov et al. (dashed curve) [14] Theoretical results are shifted toward left by 4.5 eV for comparison.

spherical, short range, attractive potential shell of radius 5.8 au, thickness 1.9 au and potential depth 8.2 eV, and calibrated by reproducing the known electron affinity of C_{60}.

Calculations within the framework of both models yielded a 4d photoionization cross section of the encapsulated Xe atom with maxima and minima. Their results indicate that the amplitude of oscillations depends on the thickness of the fullerene shell. The energy dependences and the amplitudes of the resonances predicted by these two models in the 4d photoionization cross section of $Xe@C_{60}$ are different from the

experimental results. This suggests that model descriptions of C_{60} by a spherical potential of zero or fixed thickness cannot fully describe the electron dynamics of such a complex multi-electron system.

7.4.2 Comparison to TDDFT Calculations

Figure 7.6 presents a comparison of experimental results with the theoretical results for photoionization of $Xe@C_{60}$ using methods based on the time dependent density functional theory (TDDFT). The TDDFT calculations of the 4d photoabsorption cross section of the Xe atom inside C_{60} molecule (blue curve) were made by Puska et al. [12] and Madjet et al. [15] (red curve) using a jellium shell model in conjunction with local density approximation (LDA). Both of these studies used the same model which considers all the valence electrons forming a delocalized charged cloud, and treats the residual ion-core as a classical jellium shell. The jellium potential representing 60 C^{4+} ions is constructed as a uniform charge density over a spherical shell with radius R (taken to be the known radius of C_{60}, (3.54 A°) and thickness Δ, increased by a constant potential V_0 to ensure quantitative accuracy. The Xe nucleus is placed at the center of the sphere. The Kohn-Sham equations for the system are then solved to obtain the ground state wave function in the LDA, and the parameters V_0 and Δ are determined by requiring charge neutrality with a given number of valence electrons. During these calculations, Puska et al. considered a system of 250 electrons while Madjet et al. considered 294 electrons (54 from Xe and 240 from C_{60}). The dynamic electronic response to an external dipole field was obtained through TDDFT/TDLDA which includes important many-body correlations. Although their calculations demonstrated some oscillations in the cross section curve, the present experimental results do not support their results quantitatively.

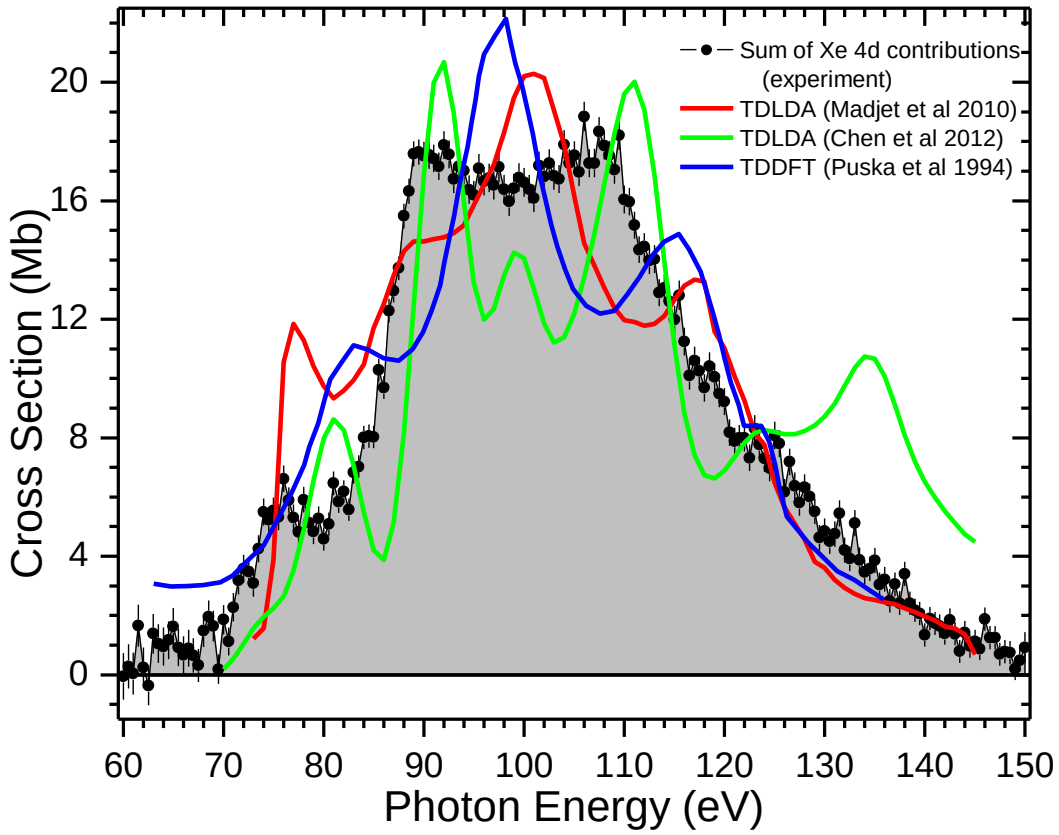

Figure 7.6 Comparison of experimental results (solid circles) with TDDFT calculations for the photoionization cross section of $Xe@C_{60}^{+}$. Blue, red, and green curves represent the calculations made by Puska et al. [12], Madjet et al. [15], and Chen et al. [16], respectively.

Recently, Chen et al. [16] performed TDDFT calculation for the photoabsorption spectrum of the $Xe@C_{60}$. In their approach, dynamical polarizability of an interacting electron system was represented by an off-diagonal matrix element of the resolvent of the Liouvillian superoperator. The problem was solved with the Lanczos algorithm to the first order expansion of the time-dependent Kohn-Sham equation in the linear response regime to determine the dipole susceptibility. The photoabsorption spectrum was then

calculated from the imaginary part of the dipole susceptibility. This method avoids the classical jellium approximation. Their results are close to the experimental results in the energy range below 115 eV if shifted down in energy by 2.5 eV (Figure 7.6). However, the amplitudes of the peaks differ greatly from the measured data.

7.4.3 Comparison to R-matrix Calculations

Figure 7.7 compares the experimental results with the theoretical results of Gorczyca et al [18]. The modified R-matrix method was used to compute the 4d photoionization of $Xe@C_{60}$. The external environment imposed by the fullerene cage was described by a simple, local, spherically symmetric, attractive cage potential of constant depth (U_0) in the region of the fullerene shell of inner radius (r_0) and outer radius (r_1). They used the cage potential with parameters r_0 = 6.02 a. u., r_1 = 7.27 a. u., and U_0 = 0.422 a. u., which were the values obtained by Dolmatov et al. [39] in fitting their theoretical results to the experimental photoionization data [26]. These values differ somewhat from the more commonly used values that were empirically determined from experimental results giving r_0 = 5.8, r_1 = 7.7 a. u. [109] and binding energy U_0 = 0.301 a. u. [110, 111]. To match the experimental results, only about 2/3rd of the theoretical cross sections are considered and shifted down in energy by 2 eV. Below 115 eV, the energy dependence of the cross section and the oscillatory structures match experiment satisfactorily. Despite the discrepancy in amplitude of the peaks, there is encouraging agreement between experiment and theory for the structures in this energy range.

Measurements and calculations each indicate some redistribution of oscillator strength with respect to photon energy compared to that for a free Xe atom but they differ

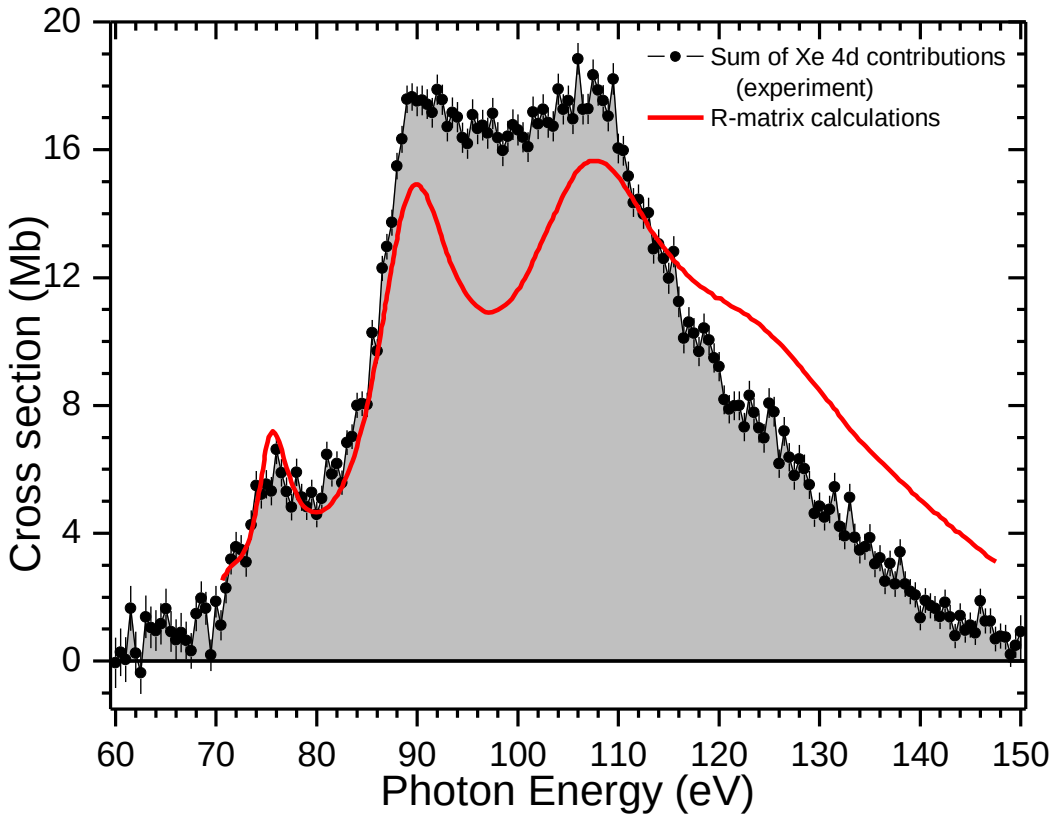

Figure 7.7 Comparison of experimental results (solid circles) with the R-matrix calculations for photoionization of Xe@C_{60} (curve) by Gorczyca et al. [18]. Theoretical cross section is shifted down in energy by 2 eV for comparison.

considerably in the details which are evidently sensitive to the geometry of the fullerene shell and on the method used to characterize it. All calculations to date represent the C_{60} cage either by a spherical delta-potential of zero thickness or by a spherical square-well potential, which are computationally convenient but can introduce numerical instability due to their sharp forms. A model potential having a smooth form like spherical Gaussian shell would be an alternate way to describe the carbon cage in endohedral Xe@C_{60}.

For consideration of photoionization of a deep inner shell of a Xe atom located inside C_{60}, the electron wavefunction can be considered to be same as that of an isolated

atom, but the situation for the continuum wavefunction describing the outgoing photoelectron is different. This is because the photoelectron feels the potential of the fullerene shell as well as that of the atomic residue. In the theoretical studies [10, 15, 16, 18] using model potentials of square well type, the fullerene cage potential is approximated and replaced by a phenomenological potential *V(r)* formed by carbon atoms smeared on a sphere of radius *R*, the radius of the fullerene shell. The potential of the fullerene shell is characterized by fullerene shell radius *R*, thickness Δ, and depth of the potential well U_0. Only the value of fullerene shell radius R= 2.64 A^0 available from experimental data is used. Value of thickness of fullerene shell is estimated indirectly and taken to be comparable to the diameter of carbon atoms forming the shell. Since the shell thickness and the potential depth are related to each other, depth of the potential well is uncertain owing to the uncertainty in thickness Δ.

Similarly, in the delta-potential model [13], the fullerene shell potential *V(r)* a spherical delta function with thickness of the fullerene shell taken to be zero. This potential depends on the fullerene radius *R* and potential depth U_0. The value of potential depth is estimated by changing its value to maintain the known electron affinity of C_{60}. It creates the problem with the model descriptions of shape and parameters of fullerene shell potential. To explain the nature of the experimental results for Xe 4d cross sections, one has to model the phenomenological potential with the parameters based on experimental results.

Chapter 8
Summary, Conclusion and Outlook

Cross sections for the photoionization and fragmentation of $Xe@C_{60}^{+}$ were measured in the photon energy range of the Xe 4d giant resonance by the ion-photon merged-beams technique using monochromatized synchrotron radiation at the ALS. Prior to the cross section measurements for photoionization of $Xe@C_{60}^{+}$, samples containing $Xe@C_{60}$ were produced at ALS. Summary and conclusions of these measurements and results are presented in this chapter with a future outlook.

8.1 Summary and Conclusions

Samples containing $Xe@C_{60}$ were prepared from a set up developed at the ALS. Isotopically enriched ^{136}Xe was used and the sample production parameters were optimized to increase the endohedral $Xe@C_{60}$ yield in the prepared samples. Samples were re-evaporated in a small oven into a low-power argon discharge in an ECR ion source. Endohedral $Xe@C_{60}$ yields as high as $2.5x10^{-4}$ were synthesized and an ion beam current of $Xe@C_{60}^{+}$ was obtained up to 5.5 pA for the merged-beams experiments.

Cross section measurements were performed in the 60 – 150 eV photon energy range for single, double, and triple photoionization with fragmentation of endohedral $Xe@C_{60}^{+}$ yielding $Xe@C_{60-2n}^{2+}$ (n = 0, 1), $Xe@C_{60-2n}^{3+}$ (n = 0, 1, 2, 3), and $Xe@C_{58}^{4+}$ products. Reference measurements were also made for the empty C_{60}^{+} cage for the same reaction channels under identical conditions. These spectroscopic measurements were put onto an absolute scale by measuring absolute cross sections for photoionization and

fragmentation of C_{60}^{+} at several discrete photon energies. Results are summarized in Figure 8.1.

Net Xe 4d contributions due to photoionization of $Xe@C_{60}^{+}$ yielding various products, were obtained by taking the excess cross section of endohedral $Xe@C_{60}^{+}$ relative to the same process for the empty C_{60}^{+} cage. No evidence of Xe 4d signature was observed in the single photoionization and fragmentation of $Xe@C_{60}^{+}$ yielding $Xe@C_{60}^{2+}$ and $Xe@C_{58}^{2+}$ products. Results from the cross section measurements for double and triple photoionization with fragmentation of $Xe@C_{60}^{+}$ yielding $Xe@C_{60-2n}^{3+}$ (n = 0, 1, 2, 3), and $Xe@C_{58}^{4+}$ product channels, showed the strong Xe 4d contributions. Net Xe 4d contributions for all product channels are compared in Figure 8.2 and their integral oscillator strengths are summarized in Table 8.1. For all double photoionization with fragmentation product channels, observed Xe 4d contributions were found to exhibit oscillatory structures having similar energy dependences, called confinement resonances. The $Xe@C_{56}^{3+}$ product channel was found to be dominant product channel. About 62% ± 14% of the total Xe 4d oscillator strength was found to be distributed among these product channels.

A measurement of triple photoionization with fragmentation of $Xe@C_{60}^{+}$ yielding the $Xe@C_{58}^{4+}$ product also exhibited statistically significant structure due to confinement resonances but the energy dependence is somewhat different from those observed in double photoionization product channels. This product channel contributes only about 5% of the total Xe 4d oscillator strength.

Table 8.1 Integral oscillator strength of Xe 4d for measured product channel.

Product channels	**Area under the curve (Mb.eV)** (70-150 eV)	**Oscillator strength** (Area x 9.11 x 10^{-3})
$Xe@C_{60}^{3+}$	187.38	1.71
$Xe@C_{58}^{3+}$	165.98	1.51
$Xe@C_{56}^{3+}$	231.14	2.11
$Xe@C_{54}^{3+}$	93.04	0.85
$Xe@C_{58}^{4+}$	51.19	0.47
Sum	**728.73**	**6.65**

The sum of net Xe 4d contributions from all measured product channels was compared with a number of theoretical results calculated using different approximation methods and modeling of C_{60} cage. All theoretical results are based on the models representing the C_{60} shell potential by either a spherical delta-potential of zero thickness or by a spherical square-well potential, which are computationally convenient but somewhat unphysical. The theoretical calculations have been made for neutral $Xe@C_{60}$ but the experimental results are for $Xe@C_{60}^{+}$ ion. Both the measurements and calculations indicate some redistribution of oscillator strength with respect to photon energy compared to that for a free Xe atom but they differ somewhat in the details which are evidently sensitive to the geometry of the fullerene shell and on the method used to characterize it. Features near 76 eV, 90 eV and 108 eV are prominent in the measurements and are also evident in the theoretical calculations at photon energies higher by several eV.

Finally, experimental evidence and details for the redistribution of the oscillator strength associated with Xe 4d photoionization in the endohedral $Xe@C_{60}^{+}$ molecular ion

will help theorists to better characterize the quantum confinement phenomenon by modeling C_{60} cage potential in terms of experimental variables. The caged Xe atom serves as the photoelectron source in this single-molecule interferometer system, thereby providing a powerful means of probing details of the electronic structure of the encaging molecule from within. Also, the 4d-photoionization of the encaged Xe atom leads to enhanced destruction of the C_{60}^{+} cage. Apparently, the caged Xe atom serves as an efficient converter of photon energy to molecular vibrational energy. This effect may be useful for cancer therapy or for nano-structuring of solid surfaces, where damage to a molecular or crystalline environment needs to be applied in a controlled and well localized manner.

8.2 Outlook

Due to limitation in the beamtime available at the ALS, cross section measurements were performed only for $Xe@C_{58}^{4+}$ products in the triple photoionization and fragmentation of $Xe@C_{60}^{+}$ reaction channel. Results showed significant Xe 4d signatures having different nature compared to those from double photoionization with fragmentation product channels. Shake-off might be an important process to explain the nature of the observed confinement resonances. For this, measurements for triple photoionization with fragmentation of $Xe@C_{60}^{+}$ yielding other products e.g. $Xe@C_{60}^{4+}$, $Xe@C_{56}^{4+}$ would be challenging but a further step forward to examine this phenomenon. Measurements for photoionization of $Xe@C_{60}^{+}$ cage performed in energy range 60 – 150 eV showed the effect of the C_{60}^{+} cage on the Xe 4d giant resonance. It would be interesting to see the effect of the caged Xe atom on the C_{60}^{+} surface and volume plasmon resonances observed near 22 eV and 38 eV, respectively [81]. In photoionization studies

of $Ar@C_{60}$, an order of magnitude enhancement in the Ar 3p cross section and an attenuation of the C_{60} surface plasmon has been predicted in the 19 – 35 eV photon energy range [36]. Similar measurements would be significant in probing the dynamics of the interaction between a caged noble gas atom and its molecular cage [112].

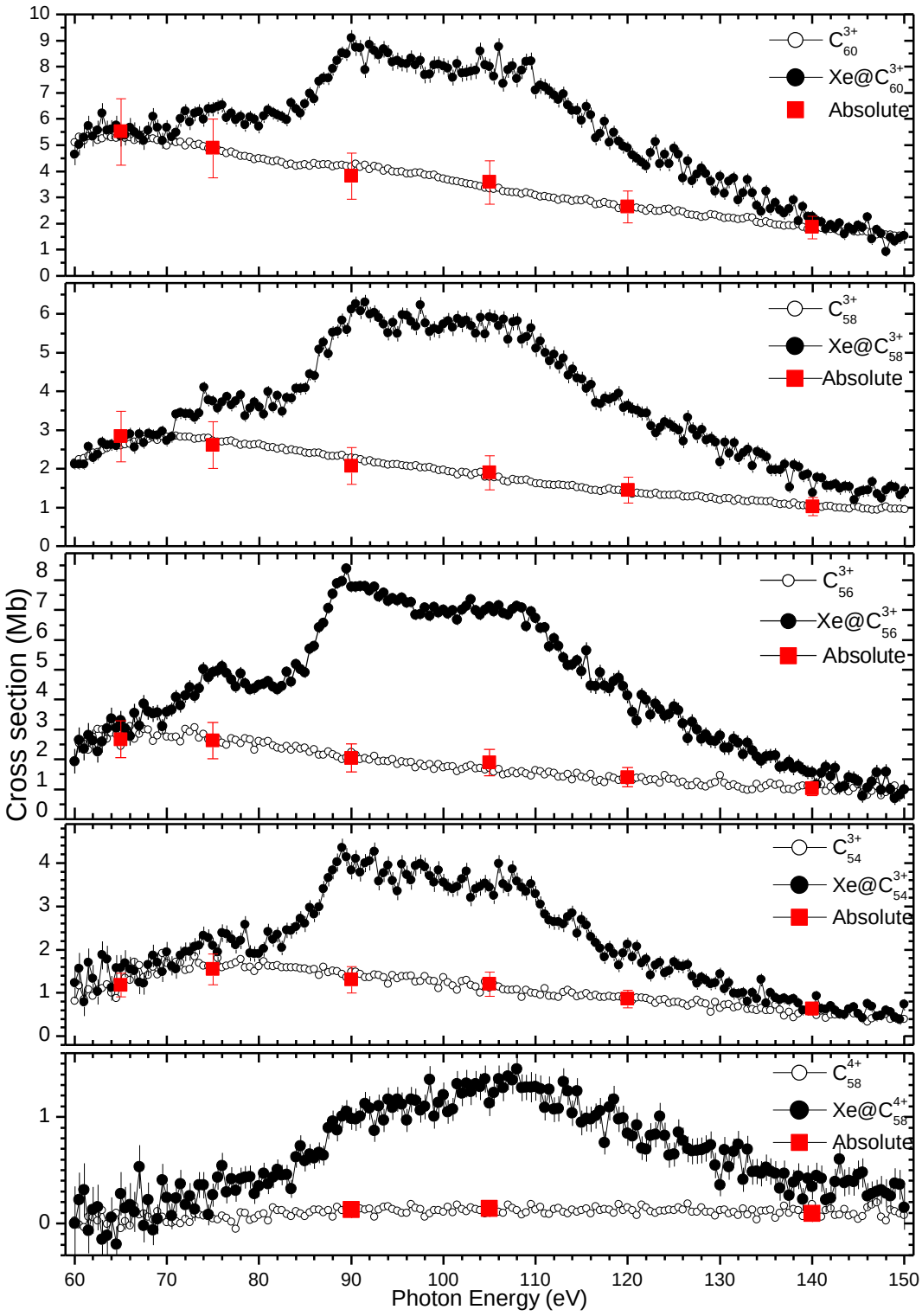

Figure 8.1 Cross section measurements for photoionization and photoionization with fragmentation of the endohedral $Xe@C_{60}^{+}$ and the empty C_{60}^{+} cage.

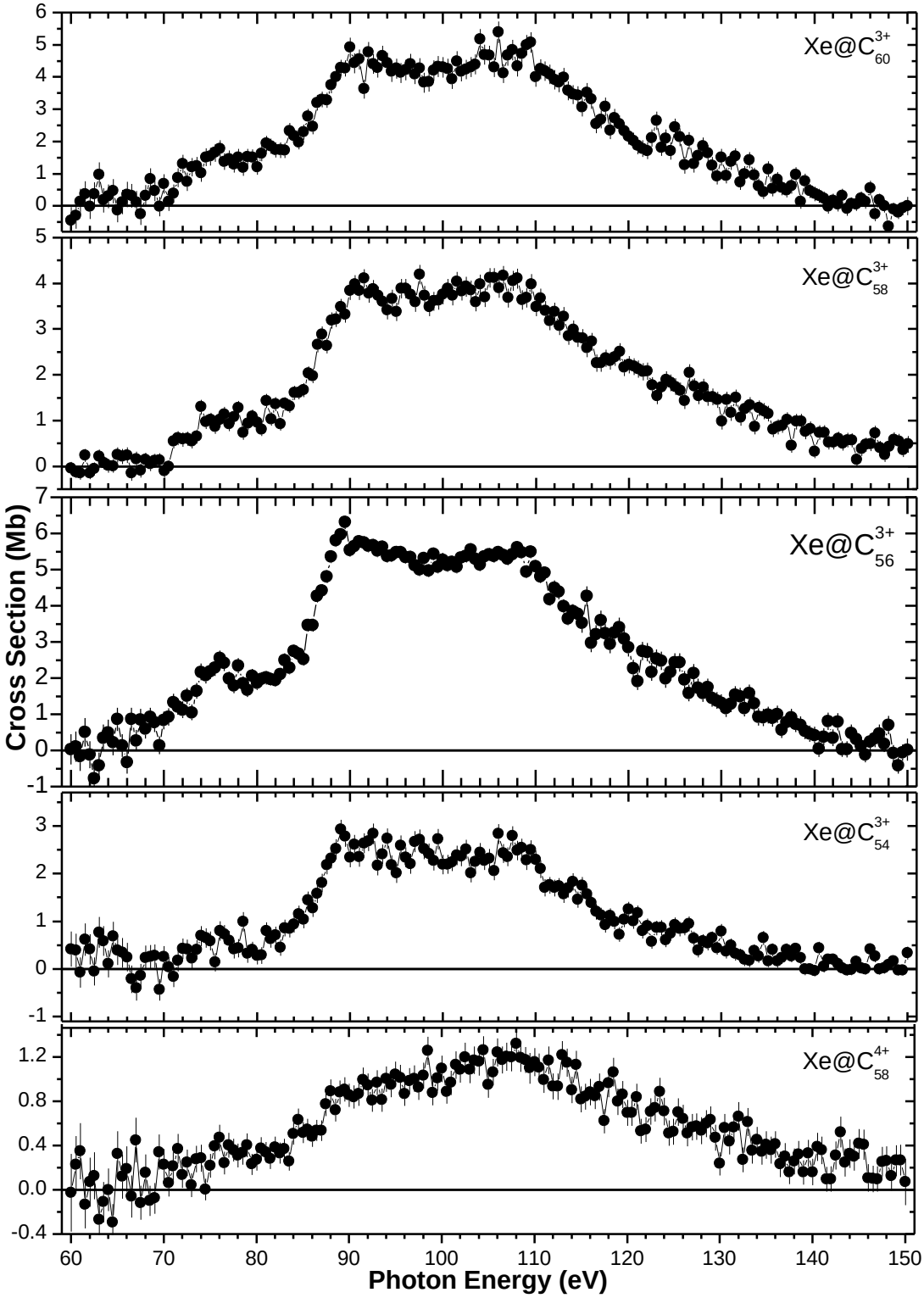

Figure 8.2 Measurements of the Xe 4d contributions to the photoionization of $Xe@C_{60}^{+}$ yielding various products.

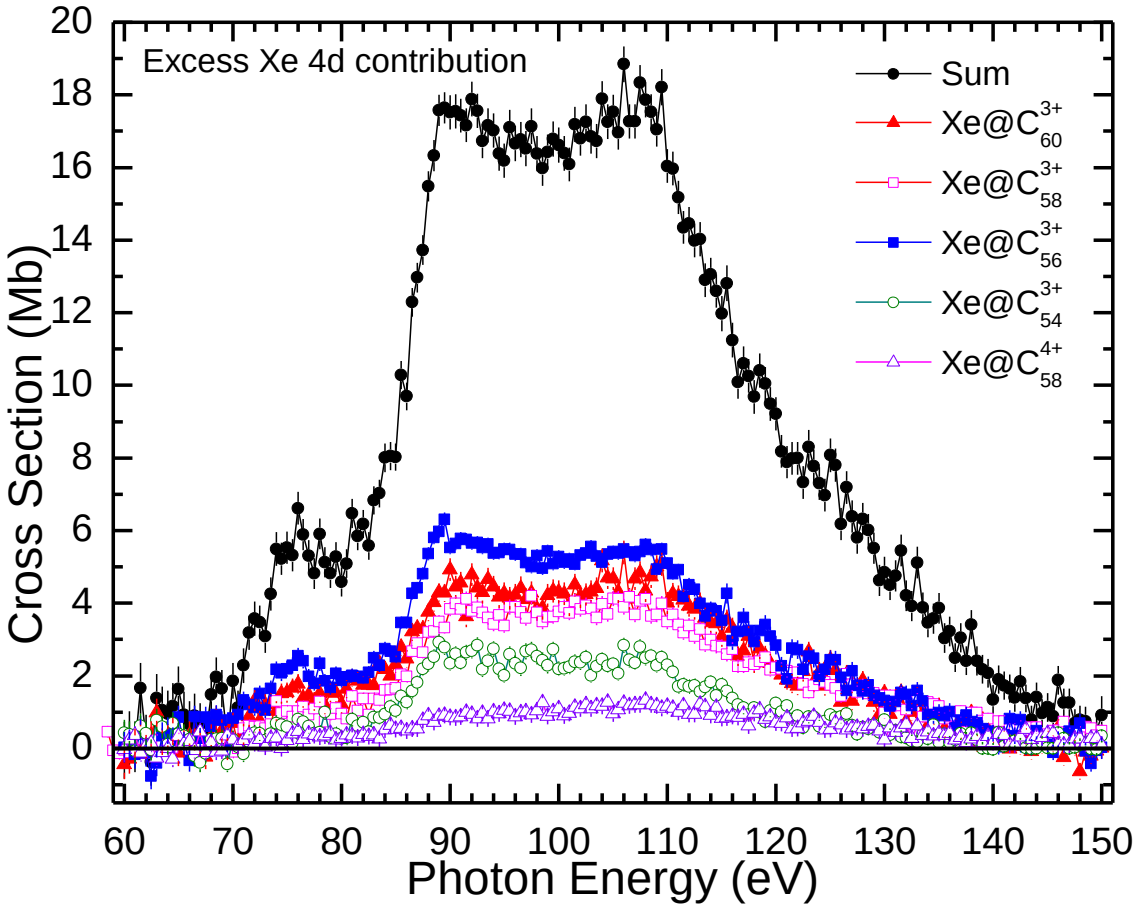

Figure 8.3 The individual Xe 4d contributions to the photoionization of $Xe@C_{60}^{+}$ yielding various products, and their sum.

References

[1] G. Ferland, D. W. Savin, and Astronomical society of the Pacific, *Spectroscopic challenges of photoionized plasmas*: proceedings of a conference held at University of Kentucky, Lexington, Kentucky, USA, 15-18 November 2001. San Francisco (Calif.): Astronomical society of the Pacific, (2001).

[2] H. Kjeldsen, *Photoionization cross sections of atomic ions from merged-beam experiments*, J. Phys. B: At. Mol. Opt. Phys., **39**, R325, (2006).

[3] J. B. West, *Photoionization of atomic ions*, J. Phys. B: At. Mol. Opt. Phys., **34**, R45, (2001).

[4] H. W. Kroto, J. R. Heath, S. C. O'Brien, R. F. Curl, and R. E. Smalley, *C_{60}: Buckminsterfullerene*, Nature, **318**, 1623, (1985).

[5] J. R. Heath, S. C. O'Brien, Q. Zhang, Y. Liu, R. F. Curl, F. K. Tittel, and R. E. Smalley, *Lanthanum complexes of spheroidal carbon shells*, J. Am. Chem. Soc., **107**, 7779, (1985).

[6] W. Harneit, *Fullerene-based electron-spin quantum computer*, Phys. Rev. A, **65**, 032322, (2002).

[7] O. V. Pupysheva, A. A. Farajian, and B. I. Yakobson, *Fullerene Nanocage Capacity for Hydrogen Storage*, Nano Lett., **8**, 767, (2008).

[8] K. B. Hartman, M. G. Rosenblum, and L. J. Wilson, *Detecting and treating cancer with nanotechnology*, Molecular Diagnosis & Therapy, **12**, 1, (2008).

[9] L. Becker, R. J. Poreda, A. G. Hunt, T. E. Bunch, and M. Rampino, *Impact Event at the Permian-Triassic Boundary: Evidence from Extraterrestrial Noble Gases in Fullerenes*, Science, **291**, 1530, (2001).

[10] Puska and Nieminen, *Photoabsorption of atoms inside C_{60}*, Phys. Rev., A, **47**, 1181, (1993).

[11] J. P. Connerade, V. K. Dolmatov, and S. T. Manson, *On the nature and origin of confinement resonances*, J. Phys. B: At. Mol. Opt. Phys., **33**, 2279, (2000).

[12] Puska and Nieminen, *Erratum: Photoabsorption of atoms inside C_{60}*, Phys. Rev., A, **49**, 629, (1994).

[13] M. Y. Amusia, A. S. Baltenkov, L. V. Chernysheva, Z. Felfli, and A. Z. Msezane, *Dramatic distortion of the 4d giant resonance by the C_{60} fullerene shell*, J. Phys. B: At. Mol. Opt. Phys., **38**, L169, (2005).

[14] V. K. Dolmatov and S. T. Manson, *Correlation confinement resonances in photoionization of endohedral atoms: Xe@C_{60}*, J. Phys. B: At. Mol. Opt. Phys., **41**, 165001, (2008).

[15] M. E. Madjet, T. Renger, D. E. Hopper, M. A. McCune, H. S. Chakraborty, J.-M. Rost, and S. T. Manson, *Photoionization of Xe inside C_{60}: Atom-fullerene hybridization, giant cross-section enhancement, and correlation confinement resonances*, Phys. Rev. A, **81**, 013202, (2010).

[16] Z. Chen and A. Z. Msezane, *Photoabsorption spectrum of the Xe@C_{60} endohedral fullerene*, Eur. Phys. J. D, **66**, 1, (2012).

[17] K. Govil, A. J. Siji, and P. C. Deshmukh, *Relativistic and confinement effects in photoionization of Xe*, J. Phys. B: At. Mol. Opt. Phys., **42**, 065004, (2009).

[18] T. W. Gorczyca, M. F. Hasoglu, and S. T. Manson, *Photoionization of endohedral atoms using R-matrix methods: Application to Xe@C_{60}*, Phys. Rev. A, **86**, 033204, (2012).

[19] V. V. Albert, J. R. Sabin, and F. E. Harris, *Simulated structure and energetics of endohedral complexes of noble gas atoms in buckminsterfullerene*, International J. Quan. Chem., **107**, 3061, (2007).

[20] M. Y. Amusia, L. V. Chernysheva, G. F. Gribakin, and K. L. Tsemekhman, *Single and double photoionisation in Xe and Ba above the 4d threshold*, J. Phys. B: At. Mol. Opt. Phys., **23**, 393, (1990).

[21] A. Müller, S. Schippers, M. Habibi, D. Esteves, J. C. Wang, R. A. Phaneuf, A. L. D. Kilcoyne, A. Aguilar, and L. Dunsch, *Significant Redistribution of Ce 4d Oscillator Strength Observed in Photoionization of Endohedral $Ce@C_{82}^{+}$ Ions*, Phys. Rev. Lett., **101**, 133001,(2008).

[22] K. Mitsuke, T. Mori, J. Kou, Y. Haruyama, and Y. Kubozono, *4d→4f dipole resonance of the metal atom encapsulated in a fullerene cage: $Ce@C_{82}$*, J. Chem. Phys., **122**, 064304, (2005).

[23] K. Mitsuke, T. Mori, J. Kou, Y. Haruyama, Y. Takabayashi, and Y. Kubozono, *Phot-oion yield curves of $Dy@C_{82}$ in the vacuum UV region*, International Journal of Mass Spectrometry, **243**, 121, (2005).

[24] H. Katayanagi, B. P. Kafle, J. Kou, T. Mori, K. Mitsuke, Y. Takabayashi, E. Kuwahara, and Y. Kubozono, *The 4d–4f dipole resonance of the Pr atom in an endohedral metallofullerene, $Pr@C_{82}$*, Journal of Quantitative Spectroscopy and Radiative Transfer, **109**, 1590, (2008).

[25] A. Müller, S. Schippers, R. A. Phaneuf, M. Habibi, D. Esteves, J. C. Wang, A. L. D. Kilcoyne, A. Aguilar, S. Yang, and L. Dunsch, *Photoionization of the endohedral fullerene ions $Sc_3N@C_{80}^{+}$ and $Ce@C_{82}^{+}$ by synchrotron radiation*, J. Phys.: Conf. Ser., **88**, 012038, (2007).

[26] A. L. D. Kilcoyne, A. Aguilar, A. Müller, S. Schippers, C. Cisneros, G. Alna'Washi, N. B. Aryal, K. K. Baral, D. A. Esteves, C. M. Thomas, and R. A. Phaneuf, Confinement Resonances in Photoionization of $Xe@C_{60}^{+}$, Phys. Rev. Lett., **105**, 213001, (2010).

[27] G. Wendin and B. Wästberg, *Many-electron effects in BaC_{60}: Collective response and molecular effects in optical conductivity and photoionization*, Phys. Rev. B, **48**, 14764, (1993).

[28] J. Luberek and G. Wendin, *The Ba 4d-f giant dipole resonance as a probe of the structure of endohedral $Ba@C_n$ metallofullerenes*, Chem. Phys. Lett., **248**, 147, (1996).

[29] A. S. Baltenkov, *Resonances in photoionization cross sections of inner subshells of atoms inside the fullerene cage*, J. Phys. B: At. Mol. Opt. Phys., **32**, 2745, (1999).

[30] P. Decleva, G. D. Alti, G. Fronzoni, and M. Stener, *Theoretical study of resonances in the metal core photoionization of $M@C_{60}$ (M = Li, Na, K)*, J. Phys. B: At. Mol. Opt. Phys., **32**, 4523, (1999).

[31] A. S. Baltenkov, V. K. Dolmatov, and S. T. Manson, *Inner-shell near-threshold photoionization of $A@C_{60}$ endohedral atoms*, Phys. Rev. A, **66**, 023201, (2002).

[32] Z. Chen and A. Z. Msezane, *Photoionization of Ce^{3+} and $Ce^{3+}@C_{60}$*, J. Phys. B: At. Mol. Opt. Phys., **42**, 165206, (2009).

[33] M. Y. Amusia, A. S. Baltenkov, and U. Becker, *Strong oscillations in the photoionization of 5s electrons in $Xe@C_{60}$ endohedral atoms*, Phys. Rev. A, **62**, 012701, (2000).

[34] M. Y. Amusia, A. S. Baltenkov, V. K. Dolmatov, S. T. Manson, and A. Z. Msezane, *Confinement resonances in photoelectron angular distributions from endohedral atoms*, Phys. Rev. A, **70**, 023201, (2004).

[35] M. A. McCune, M. E. Madjet, and H. S. Chakraborty, *Reflective and collateral photoionization of an atom inside a fullerene: Confinement geometry from reciprocal spectra*, Phys. Rev. A, **80**, 011201, (2009).

[36] M. E. Madjet, H. S. Chakraborty, and S. T. Manson, *Giant Enhancement in Low Energy Photoemission of Ar Confined in C_{60}*, Phys. Rev. Lett., **99**, 243003, (2007).

[37] V. K. Dolmatov, *Photoionization of Atoms Encaged in Spherical Fullerenes*, in Advances in Quantum Chemistry, Ed. John Sabin and Erkki Brandas, Academic Press, 58, (2009).

[38] A. B. Patel and H. S. Chakraborty, *Fourier photospectroscopy of Xe@C_{60} through a Xe 4d resonance window: theory versus recent experiment*, J. Phys. B: At. Mol. Opt. Phys., **44**, 191001, (2011).

[39] V. K. Dolmatov, J. L. King, and J. C. Oglesby, *Diffuse versus square-well confining potentials in modelling A@C_{60} atoms*, J. Phys. B: At. Mol. Opt. Phys., **45**, 105102, (2012).

[40] T. G. Dietz, M. A. Duncan, D. E. Powers, and R. E. Smalley, *Laser production of supersonic metal cluster beams*, J Chem. Phys., **74**, 6511, (1981).

[41] R. Taylor, J. P. Hare, A. K. Abdul-Sada, and H. W. Kroto, *Isolation, separation and characterisation of the fullerenes C_{60} and C_{70}: the third form of carbon*, J. Chem. Soc., Chem. Commun., **20**, 1423, (1990).

[42] W. Krätschmer, L. D. Lamb, K. Fostiropoulos, and D. R. Huffman, *Solid C_{60}: a new form of carbon*, Nature, 347, 354, (1990).

[43] Y. Chai, T. Guo, C. Jin, R. E. Haufler, L. P. F. Chibante, J. Fure, L. Wang, J. M. Alford, and R. E. Smalley, *Fullerenes with metals inside*, J. Phys. Chem., **95**, 7564, (1991).

[44] T. Weiske, D. K. Böhme, J. Hrušák, W. Krätschmer, and H. Schwarz, *Endohedral Cluster Compounds: Inclusion of Helium within C_{60} and C_{70} through Collision Experiments*, Angew. Chem. Intern. Ed. Engl., **30**, 884, (1991).

[45] T. Weiske, T. Wong, W. Krätschmer, J. K. Terlouw, and H. Schwarz, *The Neutralization of HeC_{60}^{+} in the Gas Phase: Compelling Evidence for the Existence of an Endohedral Structure for He@C_{60}*, Angew. Chem. Intern. Ed. Engl. **31**, 183, (1992).

[46] M. M. Ross and J. H. Callahan, *Formation and characterization of carbon mol.-helium ($C_{60}He^{+}$)*, J. Phys. Chem., **95**, 5720, (1991).

[47] K. A. Caldwell, D. E. Giblin, C. S. Hsu, D. Cox, and M. L. Gross, *Endohedral complexes of fullerene radical cations*, J. Am. Chem. Soc., **113**, 8519, (1991).

[48] E. E. B. Campbell and F. Rohmund, *Fullerene reactions*, Rep. Prog. Phys., **63**, 1061, (2000).

[49] J. F. Christian, Z. Wan, and S. L. Anderson, *$Ne^{+}+C_{60}$ collisions: The dynamics of charge and energy transfer, fragmentation, and endohedral complex formation*, J. Chem. Phys., **99**, 3468, (1993).

[50] M. Saunders, H. A. Jiménez-Vázquez, R. J. Cross, and R. J. Poreda, *Stable Compounds of Helium and Neon: $He@C_{60}$ and $Ne@C_{60}$*, Science, **259**, 1428, (1993).

[51] M. Saunders, R. J. Cross, H. A. Jiménez-Vázquez, R. Shimshi, and A. Khong, *Noble Gas Atoms Inside Fullerenes*, Science, **271**, 1693, (1996).

[52] M. S. Syamala, R. J. Cross, and M. Saunders, *^{129}Xe NMR Spectrum of Xenon Inside C_{60}*, J. Am. Chem. Soc., **124**, 6216, (2002).

[53] T. Braun and H. Rausch, *Endohedral incorporation of argon atoms into C_{60} by neutron irradiation*, Chem. Phys. Lett., **237**, 443, (1995).

[54] G. E. Gadd, P. J. Evans, D. J. Hurwood, P. L. Morgan, S. Moricca, N. Webb, J. Holmes, G. McOrist, T. Wall, M. Blackford, D. Cassidy, M. Elcombe, J. T. Noorman, P. Johnson, and P. Prasad, *Endohedral fullerene formation through prompt gamma recoil*, Chem. Phys. Lett., **270**, 108, (1997).

[55] T. Ohtsuki, K. Ohno, K. Shiga, Y. Kawazoe, Y. Maruyama, and K. Masumoto, *Insertion of Xe and Kr Atoms into C_{60} and C_{70} Fullerenes and the Formation of Dimers*, Phys. Rev. Lett., **81**, 967, (1998).

[56] R. Shimshi, R. J. Cross, and M. Saunders, Beam Implantation: *A New Method for Preparing Cage Molecules Containing Atoms at High Incorporation Levels*, J. Am. Chem. Soc., **119**, 1163, (1997).

[57] S. Watanabe, N. S. Ishioka, T. Sekine, A. Osa, M. Koizumi, H. Shimomura, K. Yoshikawa, and H. Muramatsu, *Production of endohedral ^{133}Xe-fullerene by ion implantation*, J. Rad. Nucl. Chem., **255**, 495, (2003).

[58] M. Schafer-Korting, *Drug Delivery.* Springer Heidelberg Dordrecht, (2010).

[59] K. B. Hartman, M. G. Rosenblum, and L. J. Wilson, *Detecting and treating cancer with nanotechnology*, Molecular Diagnosis & Therapy, **12**, 1, (2008).

[60] S. K. Sharma, L. Y. Chiang, and M. R. Hamblin, *Photodynamic therapy with fullerenes in vivo: reality or a dream?*, Nanomedicine (London), **6**, 1813, (2011).

[61] R. B. Ross, C. M. Cardona, D. M. Guldi, S. G. Sankaranarayanan, M. O. Reese, N. Kopidakis, J. Peet, B. Walker, G. C. Bazan, E. Van Keuren, B. C. Holloway, and M. Drees, *Endohedral fullerenes for organic photovoltaic devices*, Nat Mater, **8**, 208, (2009).

[62] C. F. Fischer, *Hartree--Fock method for atoms. A numerical approach*. John Wiley and Sons, Inc., New York, (1977).

[63] U. Becker and D. A. Shirley, *Vuv and Soft X-Ray Photoionization*. Plenum Press (Newyork and London), (1996).

[64] T. N. Chang, *Many Body Theory of Atomic Structure and Photoionization*. World Scientific, (1993).

[65] D. Bohm and D. Pines, *A Collective Description of Electron Interactions. I. Magnetic Interactions*, Phys. Rev., **82**, 625, (1951).

[66] P. L. Altick and A. E. Glassgold, *Correlation Effects in Atomic Structure Using the Random-Phase Approximation*, Phys. Rev., **133**, A632, (1964).

[67] M. Amusia, L. Chernysheva, and V. Yarzhemsky, *Handbook of Theoretical Atomic Physics: Data for Photon Absorption, Electron Scattering, and Vacancies Decay.* Springer, (2012).

[68] P. Hohenberg and W. Kohn, *Inhomogeneous Electron Gas*, Phys. Rev., **136**, B864, (1964).

[69] W. Kohn and L. J. Sham, *Self-Consistent Equations Including Exchange and Correlation Effects,* Phys. Rev., **140**, A1133, (1965).

[70] E. Runge and E. K. U. Gross, *Density-Functional Theory for Time-Dependent Systems,* Phys. Rev. Lett., **52**, 997, (1984).

[71] M. Petersilka, U. J. Gossmann, and E. K. U. Gross, *Excitation Energies from Time-Dependent Density-Functional Theory,* Phys. Rev. Lett., **76**, 1212, (1996).

[72] M. E. Casida, *In Recent advances in density functional methods: Part 1*. World Scientific Singapore, (1995).

[73] E. P. Wigner and L. Eisenbud, *Higher Angular Momenta and Long Range Interaction in Resonance Reactions,* Phys. Rev., **72**, 29, (1947).

[74] P. G. Burke and K. T. Taylor, *R-matrix theory of photoionization. Application to neon and argon,* J. Phys. B: At. Mol. Phys., **8**, 2620, (1975).

[75] C. O. P. TEAM, *The Opacity Project, vol. 2*. CRC Press, (1997).

[76] I. G. Kaplan, *Comparative discussion of the giant resonance phenomenon in nuclei, atoms, atomic clusters, and condensed media,* Czech J Phys, **48**, 763, (1998).

[77] G. C. Baldwin and G. S. Klaiber, *Photo-Fission in Heavy Elements,* Phys. Rev., **71**, 3, (1947).

[78] G. C. Baldwin and G. S. Klaiber, *X-Ray Yield Curves for γ-n Reactions,* Phys. Rev., **73**, 1156, (1948).

[79] C. Brechignac and J. P. Connerade, *Giant resonances in free atoms and in clusters*, J. Phys. B: At. Mol. Opt. Phys., **27**, 3795, (1994).

[80] J. B. West, P. R. Woodruff, K. Codling, and R. G. Houlgate, *The 4d, 5s and 5p partial photoionization cross sections of xenon above the 4d threshold,* J. Phys. B: At. Mol. Phys., **9**, 407, (1976).

[81] S. W. J. Scully, E. D. Emmons, M. F. Gharaibeh, R. A. Phaneuf, A. L. D. Kilcoyne, A. S. Schlachter, S. Schippers, A. Müller, H. S. Chakraborty, M. E. Madjet, and J. M. Rost, *Photoexcitation of a Volume Plasmon in C_{60} Ions,* Phys. Rev. Lett., **94**, 065503, (2005).

[82] D. E. Sayers, E. A. Stern, and F. W. Lytle, *New Technique for Investigating Noncrystalline Structures: Fourier Analysis of the Extended X-Ray—Absorption Fine Structure,* Phys. Rev. Lett., **27**, 1204, (1971).

[83] R. A. Phaneuf, C. C. Havener, G. H. Dunn, and A. Müller, *Merged-beams experiments in atomic and molecular physics*, Rep. Prog. Phys., **62**, 1143, (1999).

[84] A. M. Covington, A. Aguilar, I. R. Covington, M. F. Gharaibeh, G. Hinojosa, C. A. Shirley, R. A. Phaneuf, I. Álvarez, C. Cisneros, I. Dominguez-Lopez, M. M. Sant'Anna, A. S. Schlachter, B. M. McLaughlin, and A. Dalgarno, *Photoionization of Ne^+ using synchrotron radiation*, Phys. Rev. A, **66**, 062710, (2002).

[85] H. Winick, *Synchrotron Radiation Sources: A Primer.* World Scientific, Singapore, (1995).

[86] D. Attwood, *Soft X-Rays and Extreme Ultraviolet Radiation: Principles and Applications.* Cambridge University Press, New York, (2007).

[87] A. van Steenbergen, *Synchrotron Radiation Sources,* IEEE Transactions on Nuclear Science, **26**, 3785, (1979).

[88] J. Schwinger, *On the Classical Radiation of Accelerated Electrons*, Phys. Rev., **75**, 1912, (1949).

[89] J. P. Blewett, *Radiation Losses in the Induction Electron Accelerator*, Phys. Rev., **69**, 87, (1946).

[90] F. R. Elder, A. M. Gurewitsch, R. V. Langmuir, and H. C. Pollock, *Radiation from Electrons in a Synchrotron*, Phys. Rev., **71**, 829, (1947).

[91] D. H. Tomboulian and P. L. Hartman, *Spectral and Angular Distribution of Ultraviolet Radiation from the 300-Mev Cornell Synchrotron*, Phys. Rev., **102**, 1423, (1956).

[92] H. Winick, *Synchrotron Radiation Sources – Present Capabilities and Future Directions*, Journal of Synchrotron Radiation, **5**, 168, (1998).

[93] D. A. Skoog, F. J. Holler, and T. A. Nieman, *Principles of instrumental analysis*. Saunders College Pub., (1998).

[94] F. Broetz, R. Trassl, R. W. McCullough, W. Arnold, and E. Salzborn, *Design of Compact All-Permanent Magnet Electron Cyclotron Resonance (ECR) Ion Sources for Atomic Physics Experiments*, Phys. Scr., 2001, 278, (2001).

[95] R. Geller, *Electron Cyclotron Resonance Ion Sources and Ecr Plasmas*. Institute of Physics Publishing, Bristol UK and Philadelphia, (1996).

[96] C. C. Havener, M. S. Huq, H. F. Krause, P. A. Schulz, and R. A. Phaneuf, *Merged-beams measurements of electron-capture cross sections for O^{5+}+H at electron-volt energies*, Phys. Rev. A, **39**, 1725, (1989).

[97] M. Lu, G. Alna'washi, M. Habibi, M. F. Gharaibeh, R. A. Phaneuf, A. L. D. Kilcoyne, E. Levenson, A. S. Schlachter, C. Cisneros, and G. Hinojosa, *Photoionization and electron-impact ionization of Kr^{3+}*, Phys. Rev. A, **74**, 062701, (2006).

[98] G. C. King, M. Tronc, F. H. Read, and R. C. Bradford, *An investigation of the structure near the $L_{2,3}$ edges of argon, the $M_{4,5}$ edges of krypton and the $N_{4,5}$ edges*

of xenon, using electron impact with high resolution, J. Phys. B: At. Mol. Phys., **10**, 3357, (1977).

[99] M. Saunders, H. A. Jimenez-Vazquez, R. J. Cross, S. Mroczkowski, M. L. Gross, D. E. Giblin, and R. J. Poreda, *Incorporation of helium, neon, argon, krypton, and xenon into fullerenes using high pressure*, J. Am. Chem. Soc., **116**, 2193, (1994).

[100] E. E. B. Campbell, R. Tellgmann, N. Krawez, and I. V. Hertel, *Production and LDMS characterisation of endohedral alkalifullerene films*, Journal of Physics and Chemistry of Solids, **58**, 1763, (1997).

[101] R. Tellgmann, N. Krawez, S.-H. Lin, I. V. Hertel, and E. E. B. Campbell, *Endohedral fullerene production*, Nature, **382**, 407, (1996).

[102] T. Almeida Murphy, T. Pawlik, A. Weidinger, M. Höhne, R. Alcala, and J.-M. Spaeth, *Observation of Atom-like Nitrogen in Nitrogen-Implanted Solid C_{60}*, Phys. Rev. Lett., **77**, 1075 (1996).

[103] M.-S. Son and Y. Kiel Sung, The atom-atom potential. *Exohedral and endohedral complexation energies of complexes of $X@C_{60}$ between fullerene and rare-gas atoms (X = He, Ne, Ar, Kr, and Xe)*, Chem. Phys. Lett., **245**, 113, (1995).

[104] Z. Altun, M. Kutzner, and H. P. Kelly, *Photoionization of the 4d subshell of xenon*, Phys. Rev. A, **37**, 4671, (1988).

[105] M. Sano, Y. Itoh, T. Koizumi, T. M. Kojima, S. D. Kravis, M. Oura, T. Sekioka, N. Watanabe, Y. Awaya, and F. Koike, *Photoionization of 4d-electrons in singly charged Xe ions*, J. Phys. B: At. Mol. Opt. Phys., **29**, 5305, (1996).

[106] D. M. P. Holland, K. Codling, G. V. Marr, and J. B. West, *Multiple photoionisation in the rare gases from threshold to 280 eV*, J. Phys. B: At. Mol. Phys., **12**, 2465, (1979).

[107] M. Y. Amusia, I. S. Lee, and V. A. Kilin, *Double Auger decay in atoms: Probability and angular distribution*, Phys. Rev. A, **45**, 4576, (1992).

[108] N. Saito and I. H. Suzuki, *Shake-off processes in photoionization and Auger transition for rare gases irradiated by soft X-rays*, Phys. Scr., **49**, 80, (1994).

[109] Y. B. Xu, M. Q. Tan, and U. Becker, *Oscillations in the Photoionization Cross Section of C_{60}*, Phys. Rev. Lett., **76**, 3538,(1996).

[110] J. P. Connerade, V. K. Dolmatov, P. A. Lakshmi, and S. T. Manson, *Electron structure of endohedrally confined atoms: atomic hydrogen in an attractive shell*, J. Phys. B: At. Mol. Opt. Phys., **32**, L239, (1999).

[111] L.-S. Wang, J. M. Alford, Y. Chai, M. Diener, and R. E. Smalley, *Photoelectron spectroscopy and electronic structure of $Ca@C_{60}$*, Z Phys D - Atoms, Molecules and Clusters, **26**, 297, (1993).

[112] M. Y. Amusia, A. S. Baltenkov, and L. V. Chernysheva, *Photoionization of the subvalent subshells of noble gas endohedrals: interference of three resonances*, J. Phys. B: At. Mol. Opt. Phys., **41**, 165201, (2008).

[113] R. D. Cowan, *The Theory of Atomic Structure and Spectra*. University of California Press, Berkeley, (1981).

[114] A. Aguilar, Ph. D. dissertation, University of Nevada, Reno (2003).

[115] D. Esteves, Ph. D. dissertation, University of Nevada, Reno (2010).

[116] http://www.upload.wikimedia.org/wikipedia/commons/9/9f/Undulator.png .

[117] http://www.als.lbl.gov/als/quickguide/bend_und.pdf.

[118] http://www.als.lbl.gov/als/als_users_bl/bl_layout.html.

[119] http://ssg.als.lbl.gov/ssgdirectory/aguilar/bl10homepage.html.

[120] J. Hellhund, Diploma thesis, Justus Liebig Universität Gießen (2011).

[121] C. Thomas, Master thesis, University of nevada, Reno (2011).

Publications

1. *Confinement resonances in photoionization of $Xe@C_{60}^{+}$,* A.L.D. Kilcoyne, A. Aguilar, A. Müller, S. Schippers, C. Cisneros, G. Alna'Washi, N. B. Aryal, K. K. Baral, D.A. Esteves, C.M. Thomas, and R.A. Phaneuf, *Phys. Rev. Lett*. **105**, 213001 (2010).

2. *Photoionization of Xe inside a C_{60}^{+} cage: A single-molecule electron interferometer,* N. B. Aryal, K. K. Baral, D. A. Esteves-Macaluso, C. M. Thomas, J. Hellhund, A. L. D. Kilcoyne, R. Lomsadze, A. Müller, S. Schippers, and R. A. Phaneuf. *In progress.*

3. *Photofragmentation of fullerene molecular ions*, K. Baral, N. Aryal, D. Esteves, C. Thomas, R. Phaneuf, D. Kilcoyne, *43nd meeting of the American Physical Society, Division of Atomic, Molecular, and Optical Physics, June 4 - 8, 2012; Bull. Am. Phys. Soc*. **57** 5 D1 27 (2012).

4. *Experimental evidence of confinement resonances in the photoionization of the endohedral $Xe@C_{60}^{+}$*, D. Kilcoyne, A. Aguilar, A. Müller, S. Schippers, C. Cisneros, G. Alna'Washi, N. Aryal, K. Baral, D. Esteves, C. Thomas, R. Phaneuf, *42nd meeting of the American Physical Society, Division of Atomic, Molecular, and Optical Physics, June 13 - 17, 2011; Bull. Am. Phys. Soc.* **56** 5 L1 142 (2011).

5. *Photoionization of Xe in a fullerene ion cage*, R. Phaneuf, N. Aryal, D. Esteves, C. Thomas, D. Kilcoyne, A. Aguilar, C. Cisneros, *41th meeting of the American Physical Society, Division of Atomic, Molecular, and Optical Physics, May 25 – 29, 2010; Bull. Am. Phys. Soc.* **55** 5 E1 67 (2010).

6. *Photoionization of fullerene ions of various mass in the energy range of the giant plasmon excitations*, D.A. Esteves, R.A. Phaneuf, A. Aguilar, A.L.D. Kilcoyne, A. Müller, S. Schippers, C. Cisneros, M. Habibi, K. Baral, N. Aryal, *40th Meeting of the American Physical Society, Division of Atomic, Molecular, and Optical Physics, May 19-23, 2009; Bull. Am. Phys. Soc.* **54**, 7 M1 17 (2009).